

Gran Sasso Science Institute

PHD PROGRAMME IN
MATHEMATICS IN NATURAL, SOCIAL AND LIFE SCIENCES

Cycle XXXII - AY 2016/2019

Mathematical models and analysis of turbulent, wall-bounded, complex flows.

PHD CANDIDATE

Francesco Sacco

PhD Thesis Submitted
January, 2019

ADVISOR

Prof. Roberto Verzicco

Gran Sasso Science Institute

Università di Roma Tor Vergata

University of Twente

Thesis Jury Members

Prof. Maurizio Quadrio (Jury President, Politecnico di Milano)

Prof. Sergio Pirozzoli (Università degli Studi di Roma “La Sapienza”)

Prof. Marcello Manna (Università di Napoli Federico II)

Dr. Mauro Chinappi (Università di Roma Tor Vergata)

Dr. Francesco Viola (Gran Sasso Science Institute, L’Aquila)

Thesis Referees

Dr. Rodolfo Ostilla-Mónico (University of Huston)

Prof. Marcello Manna (Università di Napoli Federico II)

Contents

Notations	1
1 Introduction	3
1.1 Turbulence: what is and how to describe it.	4
1.2 Taylor–Couette: the <i>Drosophila</i> of the field	8
1.3 Outline of the thesis	13
2 A pencil distributed code for strongly turbulent wall–bounded flows	15
2.1 Introduction	16
2.2 Rayleigh–Bénard convection and Taylor–Couette flow	18
2.3 Numerical scheme	20
2.4 Constraints on the timestep	24
2.5 Code Parallelization	27
2.6 Computational performance	29
2.7 Summary and prospects	30
3 Dynamics and evolution of Turbulent Taylor rolls	33
3.1 Introduction	34
3.2 Numerical details	37
3.3 Results	39
3.3.1 Changes in the rolls with Reynolds number	39
3.3.2 The Taylor roll in the context of the self sustained process	41
3.3.3 The pinning of Taylor rolls	45
3.3.4 The effect of the domain size	47
3.4 Summary and conclusions	51
4 Double maxima of angular momentum transport in small gap $\eta = 0.91$ Taylor-Couette turbulence	55
4.1 Introduction	56
4.2 Experimental setup and measurement procedure	60
4.2.1 Setup	60
4.2.2 Global measurements: Torque	60

4.2.3	Local measurements: PIV	62
4.3	Setup of the direct numerical simulations	63
4.4	Transitions and local maxima in $Nu_\omega(Ta, a)$	65
4.4.1	Transitions in the $Nu_\omega(Ta)$ scaling	65
4.4.2	Appearance and shifting of the local maxima	66
4.4.3	Local flow structure and its relation to the local Nu_ω maxima	70
4.5	Boundary layer transitions and state switching	73
4.5.1	Disappearance of the broad peak	74
4.5.2	Roll state switches	75
4.5.3	Transient roll dynamics	78
4.6	Summary and conclusions	79
5	Dynamic mode decomposition analysis of coherent structures rotating plane Couette flow	81
5.1	Introduction	82
5.2	Dynamic mode decomposition	83
5.2.1	Standard DMD	83
5.2.2	Multi-resolution DMD (mrDMD)	85
5.2.3	High order DMD	87
5.3	Numerical setup	89
5.4	Results	90
5.4.1	mrDMD	91
5.4.2	HODMD	97
5.5	Summary and conclusion	100
6	Linear correction of the turbulent velocity profile for a small gap Taylor–Couette flow	103
6.1	Introduction and background	104
6.2	The linear correction	107
6.2.1	Pressure–gradient correction to the overlap layer	107
6.2.2	Correction to the overlap layer in Taylor–Couette flow	108
6.3	Numerical framework	109
6.4	Results	111
6.5	Summary and conclusion	119
7	Conclusions and outlook	121
A	Domain dependency	127
	Bibliography	129

Notations

a	Rotation ratio $\left(-\frac{\omega_o}{\omega_i}\right)$
d	Gap between walls
G	Gravity
h	Half-gap between walls $\left(\frac{d}{2}\right)$
J^ω	Flux of angular momentum $(r^3(\langle u_r \omega \rangle_{A,t} - \nu \partial_r \langle \omega \rangle_{A,t}))$
J_{lam}^ω	Flux of angular momentum for non-vortical laminar flow $\left(\frac{2\nu r_i^2 r_o^2 (\omega_i - \omega_o)}{(r_o^2 - r_i^2)}\right)$
L_x	Streamwise extent of the system
L_z	Spanwise extent of the system
Nu_ω	Pseudo-Nusselt number $\left(\frac{J^\omega}{J_{\text{lam}}^\omega}\right)$
p	Pressure
p_x	Pressure gradient
Pr	Fluid Prandtl number $\left(\frac{\nu}{\kappa}\right)$
$r_{i,o}$	Inner, outer cylinder radii
R_c	Curvature number $\left(\frac{d}{\sqrt{r_i r_o}}\right)$
R_Ω	Non-dimensional Coriolis parameter $\left(\frac{2d\Omega}{U}\right)$
Ra	Rayleigh number $\left(\frac{g\beta\Delta L_z^3}{\nu\kappa}\right)$
$\text{Re}_{i,o}$	Reynolds number of rotating cylinders $\left(\frac{r_{i,o}\omega_{i,o}d}{\nu}\right)$
Re_S	Shear Reynolds number $\left(\frac{Ud}{\nu}\right)$
Re_τ	Friction Reynolds number $\left(\frac{2du_\tau}{\nu}\right)$
Ta	Taylor number $\left(\frac{(1+\eta)^4 d^2 (r_o + r_i)^2 (\omega_i - \omega_o)^2}{64\eta^2 \nu^2}\right)$
U	Characteristic velocity of the flow
U_f	Free-fall velocity $\left(\sqrt{g\beta\Delta L_z}\right)$
$u_{i,o}$	Azimuthal tangential velocity of the inner, outer cylinder
u_τ	Friction velocity $\left(\sqrt{\frac{\tau_w}{\rho}}\right)$

β	Isobaric thermal expansion coefficient of the fluid
δ_ν	Viscous length scale $\left(\nu\sqrt{\frac{\rho}{\tau_w}}\right)$
Δ	Temperature difference between thermal plates
ϵ	Viscous dissipation rate
η	Radius ratio (dimensionless measure of curvature) $\left(\frac{r_i}{r_o}\right)$
η_K	Kolmogorov length scale $\left(\nu^{3/4}\epsilon^{-1/4}\right)$
Γ	Aspect ratio $\left(\frac{L_z}{d}\right)$
κ	Thermal conductivity
λ_z	Wavelength of large scale structures
ν	Kinematic viscosity
ρ	Density of the fluid
σ	Pseudo-Prandtl number $\left(\frac{(1+\eta)/2}{\sqrt{\eta}}\right)^4$
τ_w	Wall shear stress
$\omega_{i,o}$	Azimuthal angular velocity of the inner, outer cylinder
Ω_{rf}	Angular velocity of the rotating frame

Chapter 1

Introduction

1.1 Turbulence: what is and how to describe it.

There are many possibilities to observe turbulent flows in our daily life, usually identified by unsteady, irregular, seemingly random and chaotic motion of a fluid. The vortices of water in a river or waterfall, the mixing of milk and coffee inside a cup or the terrifying bumps felt in an aeroplane during a flight are just a few examples from an innumerable amount. This phenomenon is embedded in everyday life.

But how is turbulence defined? Etymologically, the word *turbulence* comes from the latin word *turba* (“stir, tumult”) plus the suffix *-ulentus* (“full of, abounding in”) and describes something commonly perceived as agitated and disturbed. If we look in the dictionary we will find the following definition: “In fluid dynamics, *turbulence* is the irregular (or “chaotic”) movement of the particles of a liquid or gas characterized by strong fluctuations in speed and by whirling motions, which occurs when the fluid flow, with respect to fixed surfaces with which it is in contact, exceeds a certain critical speed. The speed field varies at every point from instant to instant so that the trajectories of the fluid particles cannot be determined a priori” [169]. Even with this definition, it is difficult to figure out clearly what a turbulent flow is. Indeed, the great Richard Phillips Feynman (1918–1988) refers to this problem as one of the most important still unsolved in classical physics, and it is due to the fact that it deals with the study of fluid motion of which patterns are characterized by being far from deterministic. Chaos is often the main ingredient which makes physical predictions hard to come by. For this reason, even giving a definition is a highly non-trivial challenge in itself.

We can start to deal with the topic by looking at figure 1.1, which shows two of the examples mentioned above. In both of them, we see that there are areas in the flow characterized by the presence of vortices of different sizes. If we look even more closely at the pictures, we can see two different states: (i) when the flow moves slowly, its structure is well-organized, usually in parallel layers. In the context of fluid science, this flow is said to be laminar. (ii) However, due to the presence of different velocities or densities, the flow pattern becomes non-regular, chaotic, complicated, and thus its trajectory cannot be described easily; this is what we call a turbulent state.

Osborne Reynolds (1842–1912) was the first who systematically studied turbulence. He conducts laboratory experiments on the flow inside circular pipes in 1883 [126]. By combining the average flow velocity U , the pipe diameter d and the kinematic viscosity of the fluid ν in the factor $Re = Ud/\nu$ (the so called Reynolds number), he observed that the dynamics of the flow could be divided into 3 different regimes: laminar (low Re), transitional (medium Re)



Figure 1.1: Left: Sketch of turbulent vortices forming on the wake of an airfoil (Credits: <https://commons.wikimedia.org/w/index.php?curid=61072555>). Right: turbulent vortices arising when we pour milk into a cup of coffee (Credits: <https://theculturetrip.com/asia/japan/articles/where-to-find-the-best-coffee-in-osaka>).

and turbulent (high Re).

The phenomenology of turbulence was better described in the seminal work by Lewis Fry Richardson (1881–1953), who presented turbulent flows as a set of vortices [128]. The bigger ones, through mechanisms of instability, produce smaller vortices which in turn generate smaller vortices and so on until the dimensions are so small that the viscosity dissipates structures preventing any further transfer of energy. By using his own words: “Big whorls have little whorls, which feed on their velocity and little whorls have lesser whorls and so on to viscosity”.

This concept of *cascading energy* was rigorously quantified in 1941 by Andrej Nikolaevič Kolmogorov (1903–1987), in his theory on homogeneous isotropic turbulence [67]. He postulated that the kinetic energy cascades from the largest, energy-containing scales to the viscous scales through a range of “inertial” scales. Small vortices in the inertial and viscous range of scales are universal, they “forget” where they come from, and do not feel the presence of the external flow. In particular, this energy distribution throughout all length scales within the inertial regime has the simple relation $E(K) \approx k^{-\frac{5}{3}}$, with wavenumbers k within the inertial range of turbulence $2\pi/(15\eta_K) > k > 2\pi/\mathcal{L}$. Here, η_K is the Kolmogorov length scale and \mathcal{L} is the so-called integral length scale. Although this theory is not exactly correct and corrections exist, it is still the most important model we have for understanding turbulence far away from walls.

In real life, however, a flow is most commonly confined by solid walls, as in our example of mixing milk in a cup of coffee (but many more exist). The presence of a wall complicates the description of turbulence. The first result in the effects of wall boundaries on the flow owe to Ludwig Prandtl (1875–1953)

who at the beginning of the last century introduces the concept of a boundary layer (BL) [121]. This seminal, but fundamental idea, allowed Prandtl himself [123, 124] and Theodore von Kármán (1881–1963) [174] to develop what would become the classical theory of wall bounded flows. Using a very similar line of argumentation as in slightly later Kolmogorov’s theory, they supposed the existence of a region in a turbulent boundary layer dominated by eddies which are too large to be damped by viscosity, and too small to feel the additional constraints imposed by the wall. They postulated that the statistics of these eddies would only depend on the shear which is transported from the bulk to the wall, in a way which is analogous to the inertial eddies of Kolmogorov, which only depend on the energy cascade. As a result, turbulent boundary layers would have a universal mean velocity profile, with a logarithmic–region, regardless of the specific flow. Prandtl’s and von Kármán’s model was extended with the purpose of understanding the cascades happening in the near–wall region.

In order to study wall–bounded turbulence for high–Reynolds number flows, i.e. $Re \gg 1$, one could design *ad hoc* experimental facilities to control precisely and monitor selected physical variables. Examples of these facilities are the Boundary Layer Wind Tunnel [24] to study turbulent boundary layer flow, the Princeton Superpipe [178] to study pipe flow, the High Pressure Convective Facility [3] to study Rayleigh–Bénard convection, the Turbulent Twente–Taylor Couette facility (T^3C) [168] to study wall–bounded turbulence in the Taylor–Couette geometry, whose schematics are represented in figure 1.2 and figure 1.3.

Turbulence can also be studied numerically through direct numerical simulations (DNS). They have the advantage of having access to the complete three–dimensional velocity and pressure field data at every time instant, that is impossible to achieve in experiments. DNS attempts to resolve all scales in the flow, from the largest scales which are of the same size as the big geometrical scales of the problem to the smallest, viscosity–dominated scales. Even for the case of homogeneous isotropic turbulence, the computational load required can be very high, as the scale separation between the largest and the smallest scale grows as $Re^{3/4}$ [120]. As a consequence, the amount of grid points required to spatially discretize a three–dimensional system grows as $Re^{9/4}$. Furthermore, not only the dynamic range of length scales grows with increasing Reynolds number, but also the dynamic range of time scales (i.e. the scale difference between the fastest and the slowest time scales) grows. When we include in the expenses the time–step required to integrate the equations, a computational cost of $Re^{11/4}$ for simulating a characteristic time unit $\mathcal{O}(L/U)$ is obtained. When we consider the real life case of wall–bounded flows, we get

1.1 Turbulence: what is and how to describe it.

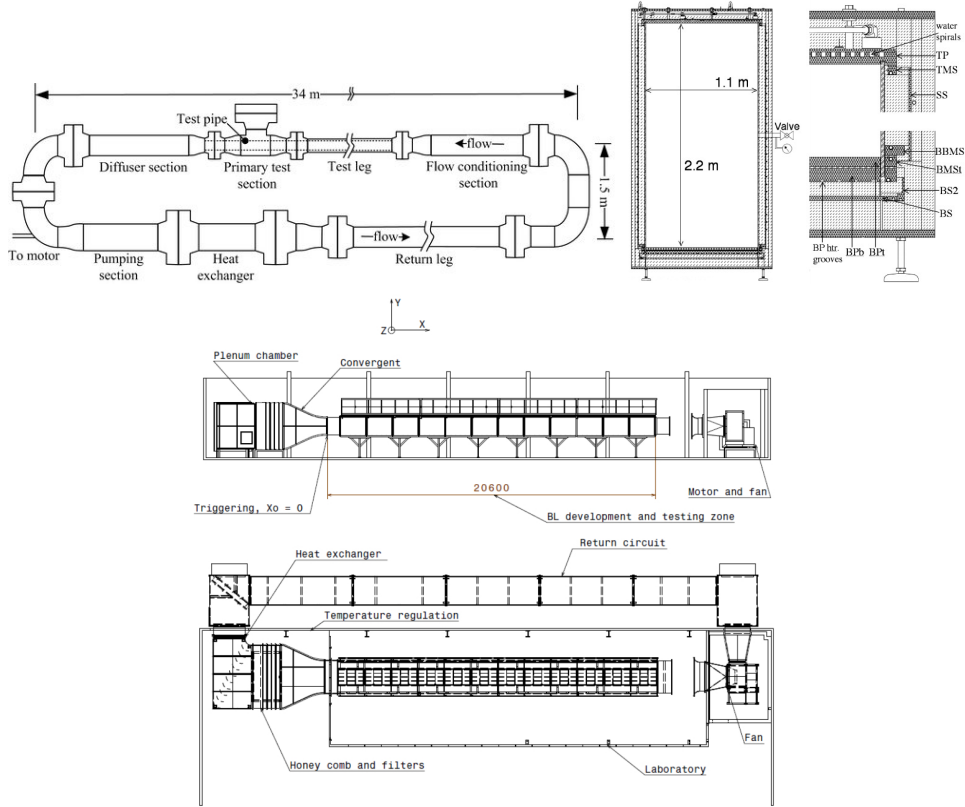


Figure 1.2: Schematic of the Princeton Superpipe facility (Top left, credits: <https://www.princeton.edu/~gasdyn/Facilities/Facilities.html#SuperPipe>), diagram of the High Pressure Convective Facility with detailed diagram of the top and bottom corners described in [5] (top right); schematic of the LMFL Boundary Layer Wind Tunnel (bottom, credits: <https://www.euhit.org/infras/lml/facilities#!>).

even more complications compared with homogeneous turbulence, due to the presence of near-wall motions. In these kind of systems we have the generation of vortices at a smaller length scale, called viscous length scale and defined as $\delta_\nu = \nu \sqrt{\frac{\rho}{\tau_w}}$, where ν is the viscosity of the fluid, τ_w is the wall shear stress and ρ is the density of the fluid. This smaller length scale impose an additional resolution requirement, since DNS have to solve structures up to the scale δ_ν close to the wall and following the computation of Pope [120], or Reynolds [127], we find that the amount of grid points required to spatially discretize a three-dimensional channel flow or boundary layers grows as $Re^{27/10}$, instead of the $Re^{9/4}$ found before.

Despite these complications, thanks to the growth of the last decades in computational power and to the presence of amazingly powerful supercomputer spread in many countries, nowadays many typical systems simulations have

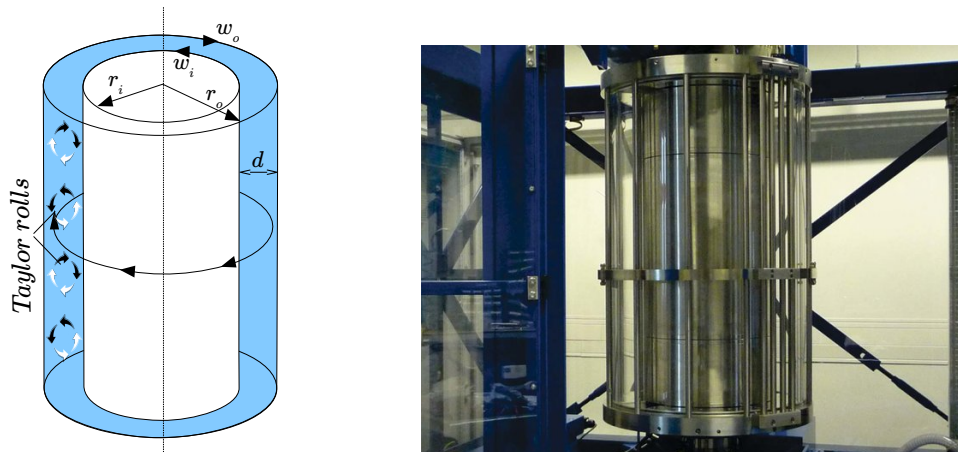


Figure 1.3: Left: schematic of the Taylor–Couette system. The system consists of two coaxial cylinders, with inner cylinder radius r_i and outer cylinder radius r_o . The inner cylinder rotates with an angular velocity ω_i and the outer cylinder rotates with an angular velocity of ω_o . Right: Twente Turbulent Taylor–Couette (T^3C) experimental facility (Picture from [168]).

become feasible, even at high level of turbulence, with a computational time consumed that ranges from 15 min CPU time on the most powerful supercomputers for “applications”, up to 250 hours, again on the most powerful supercomputers, of the channel–flow DNS of Kim et al. [65]. DNS remains a very versatile tool for the study of turbulence, and it has led to many deep insights on its nature in the last years.

1.2 Taylor–Couette: the *Drosophila* of the field

As we have mentioned in the previous section, there exist canonical systems that are fundamental to study wall–bounded turbulence for high–Reynolds number flows, i.e. $Re \gg 1$.

In this thesis we will mainly analyze through direct numerical simulations features of one of them, namely Taylor–Couette (TC) flows to understand some of its unexplored features and link them to other canonical flows. This system describes the motion of a viscous fluid confined in the gap between two coaxial, independently rotating cylinders (see figure 1.3).

TC flow is an idealized, canonical flow that is among the most investigated systems in fluid mechanics, not only thanks to its simplicity as an experimental model for shear flows, but also due to its applications in process tech-

nology. It is, next to Rayleigh–Bénard (RB) flow (the flow in a box heated from below and cooled from above), the so-called *Drosophila* of the field, and various new concepts in fluid dynamics have been tested with these systems, such as instabilities [151, 30, 20, 25, 38, 40, 39, 49, 32, 94, 56, 97, 92, 158], nonlinear dynamics and chaos [84, 2, 117, 139, 11, 102, 147], pattern formation [6, 34, 68, 19, 13], and turbulence [137, 75, 63, 4, 83]. This system is very popular because of the simplicity of its geometry and the high number of symmetries, which makes it experimentally accessible with high precision. And since it is a closed systems, directly from the Navier–Stokes equations one can extract exact global balance relations between the respective driving and the dissipation. Moreover, thanks to the presence of both convex and concave surfaces, and to the fact that these boundaries are free to move, the resulting boundary layers (BLs) are ideal to study the interaction between BLs and the bulk in non planar and rotating conditions.

The simplicity of the system is reflected in the few number of parameters we need to describe the geometry and the driving of the flow.

The geometry of TC system is completely characterized by two parameters. The first one is the radius ratio $\eta = r_i/r_o$, where r_i and r_o are the inner and the outer cylinder radii, respectively. The second one is the aspect ratio $\Gamma = L_z/d$, where $d = r_o - r_i$ correspond to the gap width between the two cylinders, and L_z is the height of the sample. The system is driven by rotation of the inner and outer cylinders. This is quantified in dimensional form by the angular velocities ω_i and ω_o and in dimensionless form by the respective Reynolds numbers Re_i and Re_o , namely

$$Re_{i,o} = \frac{r_{i,o}\omega_{i,o}d}{\nu}, \quad (1.2.1)$$

where ν is the kinematic viscosity of the fluid between the cylinders. The convention is that Re_i is always positive, whereas $Re_o > 0$ stands for a corotating outer cylinder and $Re_o < 0$ for a counter-rotating outer cylinder.

Instead of using Re_i and Re_o , one can alternatively characterize the driving of TC flow by the Taylor number

$$Ta = \frac{(1 + \eta)^4}{64\eta^2} \frac{d^2(r_o + r_i)^2(\omega_i - \omega_o)^2}{\nu^2}, \quad (1.2.2)$$

which can be seen as the nondimensional differential rotation of the system, and the rotation ratio $a = -\omega_o/\omega_i$, with $a > 0$ for counter-rotation and $a < 0$ for corotation.

As an alternative, one could also describe the parameter space characterizing the driving by the shear Reynolds number $Re_S = 2r_i r_o d |\omega_i - \omega_o| / ((r_i + r_o)\nu)$

($\text{Re}_S \propto \sqrt{\text{Ta}}$) and the rotation of the cylinders by the rotation number $R_\Omega = (1 - \eta)(r_i\omega_i + r_o\omega_o)/(r_i\omega_i - r_i\omega_o)$.

The advantages of choosing one or an other parameter representation will be described in detail in chapter 4.

The Taylor–Couette problem has a quite long history and the interest of the subject dates back to more than three hundred years ago, when Newton, investigating on rotating circular motion of fluids, firstly imagined and described the system in his *Philosophiae Naturalis Principia Mathematica* [104] back in 1687. However, the subject was forgotten for more than 100 years to be re–examined by the writings of Stokes [145] and Margules [93] in the second half on XIX century, who proposed also to construct a rotating cylinder viscometer. Basing on these ideas, in France, Maurice Couette [31] at the end of the 1800s developed in his experimental work an apparatus which he could use to measure the viscosity of fluids. This was essentially a Taylor–Couette system in which only the outer cylinder rotated. At around the same time in the United Kingdom, Mallock [90, 91] also built a device to measure torque between two coaxial cylinders, but he was able to rotate both cylinders. When only the inner cylinder was rotating, he firstly observed the turbulent regime of TC flow reflected on the torque–versus–velocity curve, which no longer followed a purely linear functional dependence. He concluded (incorrectly) that such a flow is always unstable. The first intensive studies on TC problem have been performed by Taylor [150, 152], that greatly expanded the knowledge of TC flow. Taylor’s 1923 paper contains an examination of linear stability theory for the general cases of viscous flow with both cylinders rotating in the same direction and in opposite directions. He was the first to mathematically describe the cells that form if the flow is linearly unstable. Taylor’s paper became a cornerstone in the development of hydrodynamic stability theory. He was also pioneering, since he convincingly demonstrated that the Navier–Stokes equations are the correct equations for describing fluid flow, and the no–slip condition, i.e. zero relative velocity between fluid and wall, was the correct boundary condition for viscous flows at a solid boundary. This was a great step forward, since this argument was in a great dispute by the scientific community at the time.

In the 1960s, TC flow was extensively discussed in Chandrasekhar’s “Hydrodynamic and Hydromagnetic Stability” [25]. He addressed a number of generalizations of Taylor–Couette flow and brought our experimental and theoretical understanding of Taylor–Couette flow up to date. Experimental and numerical work on TC flow also continued over the years, cf. Refs. [30, 139, 6, 74, 75, 81, 168, 115, 57, 32, 49]. For a broader historical overview on the field, which we have barely summarized here, we refer the reader to

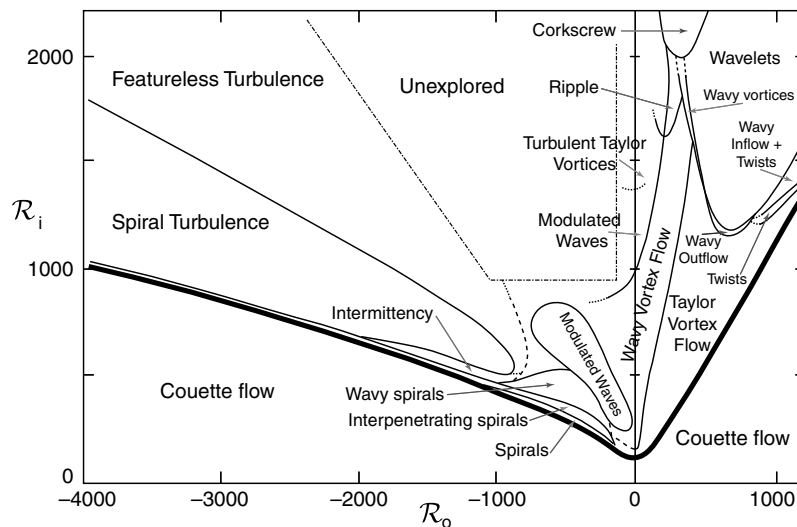


Figure 1.4: Phase diagram of patterns observed in Taylor–Couette flow as a function of Re_i and Re_o . (Picture from Cross and Greenside [35].)

Donnelly’s review [39].

Coming back to modern days, when we look at the results achieved, we can see (figure 1.4) that the phase diagram of TC flow is complex and rich, and strongly dependent on the rate of rotation of the two cylinders. In brief, TC flow is linearly stable for outer cylinder rotation and for a fixed or only slowly rotating inner cylinder. The onset of instabilities at increasing Reynolds number of the inner cylinder is caused by the driving centrifugal force and can be estimated by force balance arguments, as done by Taylor [151] and Esser and Grossmann [44], who generalized Rayleigh’s [125] famous stability criterion. In the unstable regime, one can observe Taylor rolls, modulated waves, spirals, and many other rich spatial and temporal flow features. For more details on this regime, we refer the reader to the book by Chossat and Iooss [28] and the review by Fardin et al. [47].

However, only during the last few years researchers started to complete the exploration for independently rotating cylinders and at the same time strongly driven turbulence, but still several questions remain.

The first point that need an answer is the presence of large structures at high Re . Large scale structures have been observed in many system, like Couette flow, [8, 79, 118] and square ducts [119] for large computational boxes. In this context, substantial effort has been made in order to characterize the origin, the pinning and the mathematical modeling of such structures. Large structures in TC flow are known as Taylor rolls or Taylor vortices, after the seminal works of Taylor [150]. It is well known that they develop just beyond

the onset of linear instability and they have been observed both in experiments and simulations, and dominate the flow topology up to the highest values of Reynolds number [74, 59, 107]. These structures have been traditionally attributed to the effects of centrifugal instabilities. However, for pure inner cylinder rotation, they appear to be stronger for narrow-gaps (i.e. small curvature [107], while for high curvature ($\eta = 0.5$), they survive only at mild counter-rotations [165]. This is against the centrifugal effects thesis, since otherwise they would be always the strongest for the largest centrifugal driving, i.e. for pure inner cylinder rotation. On the other side, the works of Faisst and Eckhardt [46] and Brauckmann et al. [17] have analysed the transition from TC flow to rotating plane Couette in the limit of vanishing curvature, i.e. for $\eta \rightarrow 1$. Their results suggest that for small gaps η it is rotation rate, and not curvature, that causes the origin and the pinning of such structures; moreover, the large scales reported for Plane Couette flow [8, 155] show similar patterns to the ones of TC flow. However in a shear-driven flow, like plane Couette flow, with linear instabilities absent, turbulence is regenerated by the self-sustaining process (SSP) first characterized by Waleffe [176]. A rigorous theoretical understanding of the link between TC flow and PC flow is missing, therefore we will focus on the different mechanisms that may be at play on large scales for $\eta \rightarrow 1$.

Once the causes of these structures are understood, an other missing step is to find methods to isolate them, in order to describe accurately their dynamics. Commonly used methods to extract structures include moving ensemble averages [8, 85], two-point correlations [138] or Fourier analysis [112]. However, these methods have their limitations, such as arbitrariness in parameter choice or specificity to certain setups, so they can completely fail to track structures across certain dimensions of parameter space. For this reason an other important point is the development of a low-order model for the analysis of the evolution of large-scale structures in shear-driven flows that are able to remove arbitrariness as far as possible, and robustly capture the structures everywhere in parameter space.

The second question we will focus on in this thesis is the better understanding of the phenomenon of optimal transport in TC flow. Recent experiments [168, 115, 53] revealed that for a fixed geometry η and constant driving strength Ta , a maximum in the torque-versus-rotation ratio curve was found for a certain non-zero rotation ratio. On the other side, as we have already said, Brauckmann et al. [17] numerically studied the transition from TC flow to rotating plane Couette flow (RPCF), namely the limit $\eta \rightarrow 1$ in a small-aspect ratio domain. In this limit they found that for $\eta > 0.9$ (low curvature), not one maximum of angular momentum transport is present, but two. By

combining experiments and simulations of TC flow we can look in a more detailed way at the flow. Thus, in this thesis, we will use them to further isolate and analyze the mechanisms behind optimal transport.

The last question we will try to answer is about the universality of turbulence in TC flow. Turbulence is supposed to be universal. However, since the experiments by Lewis and Swinney [81], it is known that there is a mismatch between the classical von Kármán logarithmic law and TC velocity profile, even at experiments conducted at very large Reynolds numbers $Re \approx \mathcal{O}(10^6)$. The effects of both geometry and rotation ratio of the cylinders have a role on the large scale circulation, i.e. the turbulent Taylor rolls, that seems to play a crucial role in determining the bulk dynamics. So it is crucial to disentangle those two effects, in order to recollect the universality of the logarithmic law. Once again, we can use DNS, to look in more detail and explore in depth the turbulent bulk and the turbulent boundary layers of TC flow.

1.3 Outline of the thesis

The thesis is structured so that each chapter is self-consistent, basing on papers that have been already published, submitted or that are still in preparation. It attempts to answer the questions presented in the previous section, mainly by performing direct numerical simulations.

In details it is organized as follows:

In chapter 2, we first detail the development of the numerical solver initially designed to simulate high Reynolds number wall-bounded flows, which can be directly applied to TC flow, and has been later modified for rotating plane Couette flow, the shear-driven flow between two parallel plates.

In chapter 3, we investigate on the nature of Taylor rolls at high Reynolds number, showing how they are driven by the combination of shear and mild anti-cyclonic rotation, and analyzing the effects of computational domain size on the pinning of the structure.

In chapter 4, we probe both experimentally and numerically the phase space of TC flow, for both co- and counter-rotation, analyzing the effects of driving and rotation on the torque and showing that this reveals two local maxima in a certain range of parameter space: a narrow one, linked to shear instabilities, and a broad one, caused by the centrifugal instabilities. Further changes in the flow structure for increasing driving cause the broad peak to disappear completely and only the narrow peak to survive. During this transition we also explore an unusual state, where the expected structure of counter-rotating Taylor vortex pairs breaks down and stable unpaired rolls appear locally and

we attribute it to changes in the underlying roll characteristics during the transition to the ultimate regime.

In chapter 5, we inquire about the origin of shear-driven large structures by performing Dynamic Mode Decomposition on (rotating) Plane Couette flow. We first verify that the method is adequate to capture the coherent structures and to extract correctly the different properties that arise for different control parameters, in particular the effect of rotation on the large scale structures.

In chapter 6, we develop a correction to the von Kármán logarithmic law of the velocity profile for the turbulent TC flow when the curvature of the system is small, by accounting the deviation from the law to the conserved transverse current of azimuthal motion. We show that, when the correction is applied, the logarithmic law is restored even when varying the curvature, and that the parameters found for TC flow converge to the ones of plane Couette flow, in the limit of vanishing curvature $\eta \rightarrow 1$.

In chapter 7, we conclude our dissertation with a summary of the results contributions achieved and an overview on future perspectives.

Chapter 2

A pencil distributed code for strongly turbulent wall-bounded flows

2.1 Introduction

Turbulence is known as the “last unsolved problem of classical physics”. Direct numerical simulations (DNS) provide a valuable tool for studying in detail the underlying, and currently not fully understood, physical mechanisms behind it. Turbulence is a dynamic and high dimensional process, in which energy is transferred (cascades) from large vortices into progressively smaller ones, until the scales of the energy are so small that they are dissipated by viscosity. DNS requires solving all of the flow scales, and to adequately simulate a system with very large size separation between the largest and the smallest scale, immense computational power is required.

The seminal works on homogeneous isotropic turbulence by Orszag & Patterson [105] and on pressure-driven flow between two parallel plates (also known as turbulent channel flow) by Kim and Moin [100], while difficult back then, could nowadays be performed easily on contemporary smartphones. Computational resources grow exponentially, and the scale of DNS has also grown, both in memory and floating point operations (FLOPS). In approximately 2005, the clock speed of processors stopped increasing, and the focus shifted to increasing the number of processors used in parallel, as reported in figure 2.1. This presents new challenges for DNS, and efficient code parallelization is now essential to obtaining (scientific) results.

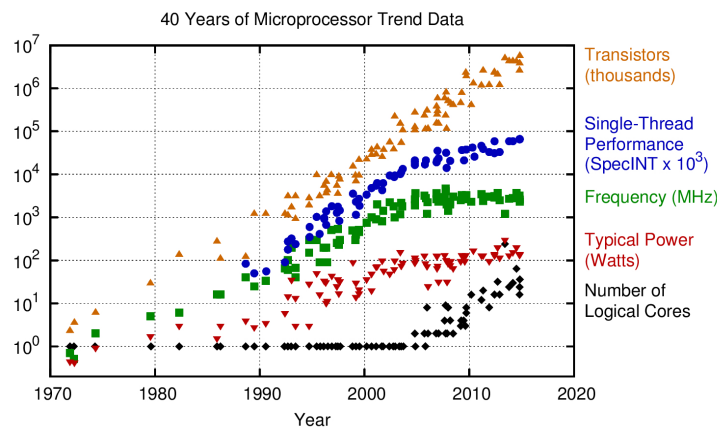


Figure 2.1: 40 Years of Microprocessor Trend Data [131]

Efficient parallelization is deeply tied to the underlying numerical scheme. A wide variety of these schemes exist; for trivial geometries, i.e. domains periodic in all dimensions, spectral methods are the most commonly used [64]. However, for the recent DNS of wall-bounded flows, a larger variation of schemes is used. For example, in 2014, two channel flow DNSs at similar Reynolds numbers were performed using both a finite-difference schemes (FDS) in the

case of Ref. [12] or a more complex spectral method in the case of Ref. [86]. FDS also present several advantages, they are very flexible, allowing for complex boundary conditions and/or structures interacting through the immersed boundary method with relative ease [45]. A commonly asserted disadvantage of low-order FDS is the higher truncation error relative to higher order schemes and spectral methods. However, this is only true in the asymptotic limit where the grid spacing $\Delta x \rightarrow 0$ that is commonly not reached. Additionally, by a comparison between different order FDS and pseudo-spectral methods in [50, 69], it was found that aliasing errors are smaller for lower order schemes. Lower-order schemes have been shown to produce adequate first- and second-order statistics, but require higher resolution when compared to spectral methods for high order statistics [99, 42, 175]. Because lower-order schemes are computationally inexpensive the grid resolution can in general be larger for the same computational cost compared to higher order schemes, although one has to consider the higher memory bandwidth over FLOPS ratio. In this chapter, we will describe the parallelization of a second-order FDS based on Verzicco & Orlandi [172] and extended to two wall bounded systems, such as Rayleigh-Bénard (RB) convection (the flow in a fluid layer between two parallel plates; heated from below and cooled from above) and Taylor-Couette (TC) flow (the flow between two coaxial independently rotating cylinders) although our code can easily be extended to any other flow that is wall-bounded in one dimension. This FDS scheme has already been used in the evolution of a free vortex ring and its collision with a wall, the formation of a tripolar vortex and the motion of a Lamb dipole crossing the origin [172], in confined thermal convection in a cylindrical cell with immersed boundary methods [146], for Rayleigh-Bénard convection [171, 173, 70, 143, 161, 162, 144] and for Taylor-Couette flow [106, 108]. The numerical results have been validated against experimental data numerous times. We will exploit several advantages of the large Re regime and the boundary conditions to heavily reduce communication cost; opening the possibility to achieve much higher driving. The chapter is organized as follows: Section 2 describes TC and RB in more detail. Section 3 details the numerical scheme used to advance the equations in time. Section 4 shows that in thermal convection, the Courant-Friedrichs-Lewy (CFL) [33] stability constraints on the timestep due to the viscous terms become less strict than those due to the non-linear terms at high Rayleigh (Reynolds) numbers. Section 5 details a pencil decomposition to take advantage of the new time integration scheme and the choice of data arrangement in the pencil decomposition. Finally, section 6 compares the computational cost of existing and the new approach and presents an outlook of what further work can be done to combine this approach with other techniques.

2.2 Rayleigh–Bénard convection and Taylor–Couette flow

RB and TC are paradigmatic models for convective and shear flows, respectively. They are very popular systems because they are mathematically well defined, experimentally accessible and reproduce many of the interesting phenomena observed in applications. A volume rendering of these flows can be seen in Fig. 2.2. The Reynolds numbers Re in the common astro- and geophysical applications are much higher than what can be reached currently in a laboratory. Therefore it is necessary to extrapolate available experimental results to the large driving present in stars and galaxies. In RB and TC the driving of the system is quantified by the Rayleigh number (Ra), i.e. the non-dimensional temperature difference, and the Taylor number (Ta), i.e. the non-dimensional cylinders differential rotation, respectively. The extrapolation becomes meaningless when transitions in scaling behaviour are present, and it is expected that once Ta (or Ra) become large enough, the boundary layers transition to turbulence. This transition would most likely affect the scaling of interesting quantities. However, experiments disagree on exactly where this transition takes place [129, 55]. DNS can be used to understand the discrepancies among experiments. However, to reach the high Ta (or Ra) of experiments new strategies are required. DNS must resolve all scales in the flow, and the scale separation between the smallest scale and the largest scale grows with Reynolds number, and so with the driving of the system, since $Re \propto \sqrt{Ta}$. This means larger grids are needed, and the amount of computational work W scales approximately as $W \sim Re^4$ [120].

Simulations of RB commonly imitate the cylindrical geometry most used in experiments. Recently, a DNS with aspect ratio $\Gamma = d/L_z = 1/3$, where d is the diameter of the plates and L_z the height of the cell reached $Ra = 10^{12}$ using 1.6 Billion points with a total cost of 2 Million CPU hours [164]. DNS in other geometries have been proposed, such as homogeneous RB, where the flow is fully periodic and a background temperature gradient is imposed. This geometry is easy to simulate [82], but presents exponentially growing solutions and does not have a boundary layer, thus not showing any transition [23]. Axially homogeneous RB, where the two plates of the cylinder are removed, and the sidewalls kept and a background temperature gradient is imposed to drive the flow has also been simulated [134]. This system does not have boundary layers on the plates and does not show the transition. Therefore, it seems necessary to keep both horizontal plates, having at least one wall-bounded direction. The simplest geometry is a parallelepiped box, periodic in both wall-parallel directions, which we will call “rectangular” RB for simplicity. Rectangular RB is receiving more attention recently [22, 116, 136, 48], due to

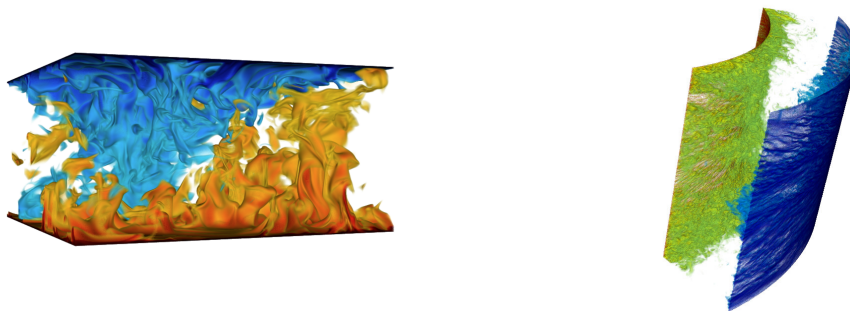


Figure 2.2: Left: RB flow for $Ra = 10^8$, $Pr = 1$ and $\Gamma = 2$ in Cartesian coordinates. The horizontal directions are periodic and the plates are subjected to a no-slip and isothermal boundary condition. Red/yellow indicates hot fluid, while (light)blue indicates cold fluid. The small heat carrying structures known as thermal plumes as well as a large scale circulation can be seen in the visualization, highlighting the scale separation in the flow. Right: TC flow with an inner cylinder Reynolds number $Re = 10^5$, a stationary outer cylinder, and a radius ratio $\eta = r_i/r_o = 0.714$. Green fluid has a high angular velocity while blue fluid has a low angular velocity. The smallness of the structures responsible for torque transport, and thus the need for fine meshes, can be appreciated clearly.

possibility to reach higher Ra as compared to more complex geometries. It is additionally the geometry that is closest to natural applications, where there are commonly no sidewalls.

For TC, we have one naturally periodic dimension, the azimuthal extent. The axial extent can be chosen to be either bounded by end-plates, like in experiments, or to be periodic. Axial end-plates have been shown to cause undesired transitions to turbulence if TC is in the linearly stable regime [7], or to not considerably affect the flow if TC is in the unstable regime [167]. Large Re DNS of TC focus on axially periodic TC, bounding the flow only in the radial direction [14, 108]. Therefore, the choice of having a single wall-bounded direction for DNS of both TC and RB seems justified.

It is important to note that RB convection and TC flow have many properties in common. Despite the differences in the driving forces, there are many similarities between the two systems. So many that Busse [21] has characterized them as *the twins of turbulence research*. Indeed a formal analogy between RB and TC flow was developed and described in Eckhardt et al. [43]. For this reason during the chapter many of the results will be shown just for one of the two systems, since they can be straightforwardly transposed to the other one.

2.3 Numerical scheme

The code, developed and described by van der Poel et al. [163], solves the Navier–Stokes equations with an additional equation for temperature (or in general an additional scalar) in three–dimensional coordinates, either Cartesian or cylindrical. The original parallel code, as we said, was firstly developed and described for RB in [163]. In this chapter all concepts will be translated to TC in cylindrical coordinates system by substituting the vertical direction for the radial direction, and the two horizontal directions by the axial and azimuthal ones. The wall-normal direction will be indicated both with x and r , the streamwise direction with y or θ and the axial direction with z . The non–dimensional Navier–Stokes equations with the Boussinesq approximation for RB read:

$$\nabla \cdot \mathbf{u} = 0, \quad (2.3.1)$$

$$\frac{\partial \mathbf{u}}{\partial t} + \mathbf{u} \cdot \nabla \mathbf{u} = -\nabla p + \sqrt{\frac{\text{Pr}}{\text{Ra}}} \nabla^2 \mathbf{u} + \Theta \mathbf{e}_x, \quad (2.3.2)$$

$$\frac{\partial \Theta}{\partial t} + \mathbf{u} \cdot \nabla \Theta = \sqrt{\frac{1}{\text{PrRa}}} \nabla^2 \Theta, \quad (2.3.3)$$

where \mathbf{u} is the non–dimensional velocity, p the non–dimensional pressure, Θ the non–dimensional temperature and t the non–dimensional time. For non–dimensionalization, the temperature scale is the temperature difference between both plates Δ , the length scale is the height of the cell L_z and the velocity scale is the free–fall velocity $U_f = \sqrt{g\beta\Delta L_z}$, where g is gravity and β is the isobaric expansion coefficient of the fluid. $\text{Pr} = \nu/\kappa$ is the fluid Prandtl number, where ν is the kinematic viscosity and κ is the thermal conductivity. The Rayleigh number is defined in this case as $\text{Ra} = G\beta\Delta L_z^3/\nu\kappa$. Finally, \mathbf{e}_x is the unity vector in parallel direction to gravity, which is also the plate–normal direction.

Equation (2.3.2) for TC becomes:

$$\frac{\partial \mathbf{u}}{\partial t} + \mathbf{u} \cdot \nabla \mathbf{u} \times \mathbf{u} = -\nabla p + \frac{f(\eta)}{\text{Ta}^{1/2}} \nabla^2 \mathbf{u} - R_\Omega \mathbf{e}_z, \quad (2.3.4)$$

where R_Ω is a Rossby number that takes into account the effects of rotational forces, $f(\eta)$ is a proportional constant that depends on the radius ratio $\eta = r_i/r_o$, where r_i and r_o are the inner and outer radii, respectively and \mathbf{e}_z is the unit vector in the axial direction. The Rossby and the proportional constant have not been written explicitly here since they depends on the reference frame and the non–dimensionalization of the system.

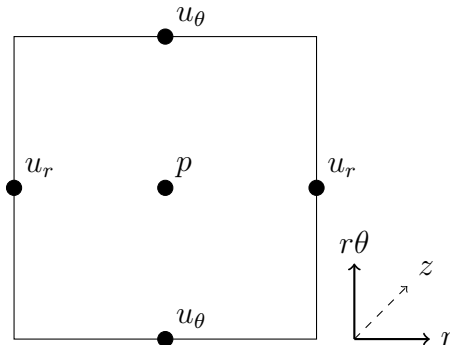


Figure 2.3: Location of pressure and velocities of a 2D simulation cell. The third dimension (z) is omitted for clarity. As on an ordinary staggered scheme, the velocity vectors are placed on the borders of the cell and pressure is placed in the cell center.

As mentioned previously, in TC the axial and azimuthal directions are periodic and the radial direction is wall-bounded. The spatial discretization used is a conservative second-order centered finite difference with velocities on a staggered grid. The pressure is calculated at the center of the cell. The scheme is energy conserving in the limit $\Delta t \rightarrow 0$. A two-dimensional (for clarity) schematic of the discretization is shown in Fig. 2.3.

Time marching is performed with a fractional-step third-order Runge–Kutta (RK3) scheme, in combination with a Crank–Nicholson scheme [99] for the implicit terms. A second-order Adams–Bashforth (AB2) method is additionally implemented. However, in all production runs the RK3 method takes precedence over AB2 even though the total RK3 time step includes three substeps as compared to one for AB2. The theoretical stability limit of AB2 and RK3 are CFL numbers lower than 1 and $\sqrt{3}$, respectively. In practice, the maximum CFL numbers of AB2 and RK3 are approximately 0.3 and 1.3, respectively. Because of three times higher amount of substeps in RK3, the computational cost is proportionally higher compared to AB2. Nevertheless, RK3 is more efficient as the progression in physical time per computational cost is better. In addition, even though it is used in combination with the Crank–Nicholson integration, of which error is $\mathcal{O}([\Delta t]^2)$, the $\mathcal{O}([\Delta t]^3)$ error of RK3 decreases the total error significantly compared to the $\mathcal{O}([\Delta t]^2)$ error of AB2. In addition, RK3 is self-starting at each time step without decreasing the accuracy and without needing additional information in the restart file. AB2 would require two continuation files per quantity.

The pressure gradient is introduced through the “delta” form of the pressure [80]: an intermediate, non-solenoidal velocity field \mathbf{u}^* is calculated using the non-linear, the viscous and the buoyancy terms in the Navier–Stokes equation,

as well as the pressure at the current time sub-step:

$$\frac{\mathbf{u}^* - \mathbf{u}^j}{\Delta t} = \left[\gamma_l H^j + \rho_l H^{j-1} - \alpha_l \mathcal{G} p^j + \alpha_l (\mathcal{A}_x^j + \mathcal{A}_y^j + \mathcal{A}_z^j) \frac{(\mathbf{u}^* + \mathbf{u}^j)}{2} \right], \quad (2.3.5)$$

where the superscript j denotes the substep, \mathcal{A}_i is the discrete differential relationship for the viscous terms in the i th-direction, \mathcal{G} the discrete gradient operator and H^j all explicit terms. The coefficients γ_l , ρ_l and α_l depend on the time marching method used. The pressure required to enforce the continuity equation at every cell is then calculated by solving a Poisson equation for the pressure correction ϕ :

$$\nabla^2 \phi = \frac{1}{\alpha_l \Delta t} (\nabla \cdot \mathbf{u}^*), \quad (2.3.6)$$

or in discrete form:

$$\mathcal{L} \phi = \frac{1}{\alpha_l \Delta t} (\mathcal{D} \mathbf{u}^*), \quad (2.3.7)$$

where \mathcal{D} the discrete divergence operator, and \mathcal{L} is the discrete Laplacian operator, $\mathcal{L} = \mathcal{D}\mathcal{G}$. The velocity and pressure fields are then updated using:

$$\mathbf{u}^{j+1} = \mathbf{u}^* - \alpha_l \Delta t (\mathcal{G} \phi), \quad (2.3.8)$$

and

$$p^{j+1} = p^j + \phi - \frac{\alpha_l \Delta t}{2\text{Re}} (\mathcal{L} \phi), \quad (2.3.9)$$

making \mathbf{u}^{j+1} divergence free.

The original numerical scheme treats all viscous terms implicitly. This would result in the solution of a large sparse matrix, but this is avoided by an approximate factorization of the sparse matrix into three tridiagonal matrices; one for each direction [172]. The tridiagonal matrices are then solved using Thomas' algorithm, (with a Sherman–Morrison perturbation if the dimension is periodic), in $\mathcal{O}(N)$ time. The calculation is thus simplified at the expense of introducing an error $\mathcal{O}(\Delta t^3)$. This method was originally developed and used for small Reynolds number problems, and without having in mind that data communication between different processes could be a bottleneck. The first parallelization scheme with MPI was a 1D-domain “slab” decomposition, visualized in the left panel of Fig. 2.4. The main bottlenecks were found in the all-to-all communications present in the pressure-correction step and the tridiagonal solver in the direction in which the domain is decomposed (cf. Table 2.1 for more details). Slab decompositions are easy to implement,

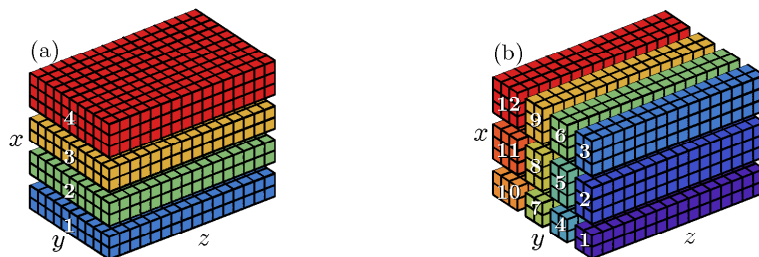


Figure 2.4: Left panel: Slab-type domain decomposition using four MPI processes. Right panel: Pencil-type domain decomposition using twelve MPI processes.

but are limited in two ways: First, the number of MPI processes cannot be larger than N , the amount of grid points in one dimension. A hybrid MPI–OpenMP decomposition can take this limit further, but scaling usually does not go further than 10^4 cores. Second, the size of the “halo” (or ghost) cells becomes very significant with increasing number of cores. Halo cells are cells which overlap the neighbor’s domain, and whose values are needed to compute derivatives. In the limit of one grid point per processor, halo cells are of the size of the domain in a second-order scheme, and even larger for higher order schemes.

2D-domain decompositions, also known as “pencil” decompositions mitigate these problems. A schematic of this decomposition is shown in Fig. 2.4. To implement this decomposition, the 2DECOMP [1] library has been used, and extended upon to suit the specifics of our scheme. The limit on the amount of processes is now raised to N^2 , and the size of the halo cells on every core *decreases* with increasing amount of cores, so the amount of communication per core decreases. However, for a pencil decomposition solving all the tridiagonal matrices requires all-to-all communications for two directions, instead of one direction in the case of slab decomposition. As mentioned previously, solving the tridiagonal matrices involves large data communication, especially in the context of pencil decompositions. In this chapter we attempt to eliminate them as far as possible and at the same time implement an efficient pencil domain decomposition by arranging the data to gain advantage of the inherent anisotropy with respect to the grid point distributions.

2.4 Constraints on the timestep

In the new scheme, solving the tridiagonal matrices in the horizontal directions is avoided by integrating not only the advection terms but also some of the viscous terms explicitly. A major concern is that this can cause the temporal stability issues that the implicit integration used to negate. In this section we argue that for high driving, Ta for TC or Ra for RB, using the Courant–Frederich–Lewy (CFL) [33] time step size constraint is sufficient. The CFL condition ensures the stability of the integration of the advection terms, and for high Ra , or Ta , it additionally ensures stability of the viscous terms. The grid point distribution in the wall-normal direction is different compared to the periodic directions. Namely, it is non-uniform in the wall-normal direction, with clustering of points near the boundaries in order to adequately resolve the boundary layers. As the periodic directions are homogeneous, no such clustering is required and the grid point distribution can be uniform. As a consequence, the minimum grid spacing in the wall-normal direction is much smaller than in the wall-parallel directions. Because of the scaling of both the time-step constraints, the viscous terms in the wall-normal direction do require implicit integration for all Ra , or Ta .

In this semi-implicit method, both viscous and non-linear terms are integrated explicitly. This requires two stability constraints on the time-step: one due to the non-linear terms, and one due to the horizontal viscous terms. For the non-linear terms, the definition of the CFL condition is given by:

$$\Delta t_{\mathbf{u}, \nabla \mathbf{u}} \leq \mathcal{C}_1 \min_{\forall \mathbf{x} \in X} \frac{1}{\frac{|u_r|(\mathbf{x})}{\Delta r(\mathbf{x})} + \frac{|u_\theta|(\mathbf{x})}{r(\mathbf{x})\Delta\theta(\mathbf{x})} + \frac{|u_z|(\mathbf{x})}{\Delta z(\mathbf{x})}}, \quad (2.4.1)$$

where \mathcal{C}_1 is the integration scheme dependent Courant number, \mathbf{x} is the position vector, X is the complete domain and $|\cdot|$ gives the absolute value. Here Δr gives the (non-dimensional) grid spacing in the r direction at position \mathbf{x} . The wall-normal direction is r , the azimuthal direction is θ and the axial direction is z (cf. Fig. 2.3).

The additional constraint originates from the viscous terms, and is given by:

$$\Delta t_{\nu, \nabla^2 \mathbf{u}} \leq \text{Re} \mathcal{C}_2 \min_{\forall \mathbf{x} \in X} (r(\mathbf{x})\Delta\theta(\mathbf{x}) + \Delta z(\mathbf{x}))^2, \quad (2.4.2)$$

where $\text{Re} = \frac{\sqrt{Ta}}{f(\eta)}$, is the Reynolds number, and \mathcal{C}_2 a number which depends on the integration scheme and the number of dimensions treated explicitly. This condition only needs to be satisfied in the azimuthal and axial directions, and not in the radial direction, as the time integration of the radial second derivatives is kept implicit. Thus $\Delta r(\mathbf{x})^2$ can be very small, and the resulting time-step would make the simulation infeasible.

2.4 Constraints on the timestep

We can now compare the two CFL constraints, and show that the non-linear constraint is more restrictive than the viscous constraint in the homogeneous directions. As $|u_z|$ and Δz are strictly positive, we have:

$$\frac{\text{Re } \mathcal{C}_2}{\frac{|u_r|(\mathbf{x})}{\Delta r(\mathbf{x})} + \frac{|u_\theta|(\mathbf{x})}{r(\mathbf{x})\Delta\theta(\mathbf{x})} + \frac{|u_z|(\mathbf{x})}{\Delta z(\mathbf{x})}} < \frac{\text{Re } \mathcal{C}_2}{\frac{|u_\theta|(\mathbf{x})}{r(\mathbf{x})\Delta\theta(\mathbf{x})} + \frac{|u_z|(\mathbf{x})}{\Delta z(\mathbf{x})}}. \quad (2.4.3)$$

Including the wall-normal grid spacing in the CFL condition gives a smaller time-step than only using azimuthal and axial spacing, and thus the expression on the right is an upper bound on the time-step. If we then use that the grid is uniformly and equally spaced in both azimuthal and axial directions, we can simplify the expression as $r(\mathbf{x})\Delta\theta(\mathbf{x}) = \Delta z(\mathbf{x}) = \Delta\theta$, since $r(\mathbf{x}) \sim \mathcal{O}(1)$. We also know that the dimensionless velocity is $|u| \sim \mathcal{O}(1)$ by normalization. Using all of this, we obtain:

$$\Delta t_{\mathbf{u}, \nabla \mathbf{u}} \sim \mathcal{O}(\Delta\theta), \quad (2.4.4)$$

for the non-linear CFL condition and

$$\Delta t_{\nu \nabla^2 \mathbf{u}} \sim \mathcal{O}(\text{Re } \Delta\theta^2), \quad (2.4.5)$$

from the CFL criterion for the viscous terms. We can then get a bound on the viscous time-step as a function of Ta, $\Delta t_{\nu \nabla^2 \mathbf{u}} \sim \mathcal{O}(\text{Ta}^{\frac{1}{2}} \Delta\theta^2)$.

To compare both bounds, we need an estimation for $\Delta\theta$. For a resolved DNS, $\Delta\theta$ should be similar to the smallest physical length scale in the system. Several length scales can be chosen for TC. The first choice stems from homogeneous turbulence, where the most commonly used length scale that determines the numerical resolution is the Kolmogorov length scale, $\eta_K = \nu^{3/4} \epsilon^{-1/4}$, where ϵ is the viscous dissipation rate. For TC, if we define a pseudo-Prandtl number $\sigma = \left(\frac{(1+\eta)/2}{\sqrt{\eta}}\right)^4$, we can obtain an estimate for the Kolmogorov scale by using that the volume and time averaged viscous dissipation rate can be expressed directly as a function of Nu_ω , Ta and σ [43]:

$$\langle \epsilon \rangle_{V,t} = \frac{\nu^3}{L^4} \text{Ta } \sigma^{-2} (\text{Nu}_\omega - 1). \quad (2.4.6)$$

For high Ta simulations, $\text{Nu}_\omega \gg 1$. Since $\sigma \sim \mathcal{O}(1)$, we can obtain an estimate for η_K , and thus the grid spacing as $\Delta\theta = \eta_K/L \approx (\text{Ta} \text{Nu}_\omega)^{1/4}$. If we consider the scaling law $\text{Nu}_\omega \sim \text{Ta}^\gamma$, we can now compare both CFL constraints on the time step, obtaining $\gamma \leq 1$ as a requirement for the non-linear CFL to be more restrictive on the time step than the viscous CFL constraint.

For high driving, however, the boundary layers in TC becomes turbulent, and small scale structures are generated and detached close to the wall. This was

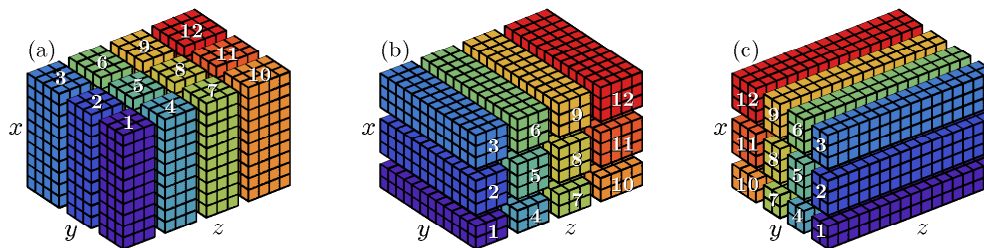


Figure 2.5: Domain decomposition of a $16 \times 12 \times 10$ grid using 12 distributed memory processes on a 4×3 process grid. Only data that is exclusive to one process is shown; i.e. a 1 gridpoint-sized halo is transparent in this figure. The pencils are a) x , b) y or c) z oriented.

firstly detected for thermal convection in RB, and so this structures are conventionally referred to as “plumes”. This naturally impose a more restrictive length scale than the Kolmogorov length scale η_K . In the case of RB, the thickness of a thermal boundary layer can be approximated by $\lambda \approx 1/(2Nu)$. In the case of TC flows, the definition of the thickness λ is more complicated, due to the presence of a convex and a concave wall, and the effects of rotation, but we can use the definition given in [14] of weighted average thickness $\lambda^{(a)} = \sigma \frac{d}{2Nu_w}$, where $d = r_o - r_i$ is the gap between the two cylinders. Using this as an estimate for $\Delta\theta$ in Eq. 2.4.1 and Eq. 2.4.2 gives as bound $\gamma \leq 1/2$. For this high Ta regime, in which both boundary layers and bulk are turbulent, a theoretical prediction of $Nu_w \propto Ta^{1/2}/\log Ta$ was given by Grossmann and Lohse [52], indicating that for the mild assumptions made, the criteria $\gamma \leq 1/2$ is always satisfied. This signifies that the scaling of $\Delta t_{\mathbf{u}, \nabla \mathbf{u}}$ is more restrictive than $\Delta t_{\nu \nabla^2 \mathbf{u}}$, which results in that using only the non-linear CFL constraint in the time-marching algorithm, inherently satisfies the stability constraints imposed by the explicit integration of the horizontal components of the viscous terms. Including the radial non-uniform grid in this derivation makes this statement even more valid, as the used CFL time step is based on this grid (Eq. 2.4.1). Inherent to the big-O-notation is the absorption of the coefficients and offsets. This makes this derivation only valid for high Ta flows. For low Ta, the solver will be unstable the viscous constraint is not satisfied in this regime.

2.5 Code Parallelization

In the previous section, we reasoned that for large Ta the implicit integration of the viscous terms in the wall-parallel directions becomes unnecessary. The calculation becomes local in space as the azimuthal and axial directions no longer require implicit solvers to calculate the intermediate velocity field \mathbf{u}^* . In this case it is worth decomposing the domain such that the pencils are aligned in the wall-normal (x) direction, i.e. that every processor possesses data from x_1 to x_N (cf. Fig. 2.5). Halo updates must still be performed during the computation of \mathbf{u}^* , but this memory distribution completely eliminates all the all-to-all communications associated to the viscous implicit solvers, as for every pair (y, z) , a single processor has the full x information, and is able to solve the implicit equation in x for the pair (y, z) without further communication.

All-to-all communications are unavoidable during the pressure correction step, as a Poisson equation must be solved. As the two wall-parallel directions are homogeneous and periodic, it is natural to solve the Poisson equation using a Fourier decomposition in two dimensions. Fourier transforming variables ϕ and the right side in Eq. 2.3.6 reduces the pressure correction equation to the Helmholtz equation:

$$\left(\frac{\partial^2}{\partial x^2} - \omega_{y,j}^2 - \omega_{z,k}^2 \right) \mathcal{F}(\phi) = \mathcal{F} \left[\frac{1}{\alpha_l \Delta t} (\mathcal{D}\mathbf{u}^*) \right] \quad (2.5.1)$$

where $\mathcal{F}(\cdot)$ denotes the 2D Fourier transform operator, and $\omega_{y,j}$ and $\omega_{z,k}$ denote the j -th and k -th modified wavenumbers in y and z direction respectively, defined as:

$$\omega_{y,j} = \begin{cases} \left(1 - \cos \left[\frac{2\pi(j-1)}{N_y} \right] \right) \Delta_y^{-2} & : \text{for } j \leq \frac{1}{2}N_y + 1 \\ \left(1 - \cos \left[\frac{2\pi(N_y - j + 1)}{N_y} \right] \right) \Delta_y^{-2} & : \text{otherwise} \end{cases}$$

and $\omega_{z,k}$ is defined in an analogous way. A modified wavenumber is used, instead of the real wavenumber, to prevent that the Laplacian has higher accuracy in some dimensions. In the limit $\Delta y \rightarrow 0$, the modified wavenumbers converge to the real wavenumbers.

By using a second order approximation for ∂_x^2 , the left hand side of the equation is reduced to a tridiagonal matrix, and thus the Poisson equation is reduced to a 2D FFT followed by a tridiagonal (Thomas) solver. This allows for the exact solution of the Poisson equation in a single iteration with $\mathcal{O}(N_x N_y N_z \log[N_y] \log[N_z])$ time complexity. Due to the domain decomposi-

tion, several data transposes must be performed during the computation of the equation. The algorithm for solving the Poisson equation is as follows:

1. Calculate $(\mathcal{D}\mathbf{u}^*)/(\alpha_l\Delta t)$ from the x -decomposed velocities.
2. Transpose the result of (1) from a x -decomposition to a y -decomposition.
3. Perform a real-to-complex Fourier transform on (2) in the y direction.
4. Transpose (3) from a y -decomposition to z -decomposition.
5. Perform a complex-to-complex Fourier transform on (4) in the z direction.
6. Transpose (5) from a z -decomposition to a x -decomposition.
7. Solve the linear system of Eq. 2.5.1 with a tridiagonal solver in the x -direction.
8. Transpose the result of (7) from a x -decomposition to a z -decomposition.
9. Perform a complex-to-complex inverse Fourier transform on (8) in z direction.
10. Transpose (9) from a z -decomposition to a y -decomposition.
11. Perform a complex-to-real inverse Fourier transform on (10) in a y direction.
12. Transpose (11) from a y -decomposition to a x -decomposition.

The last step outputs ϕ in real space, decomposed in x -oriented pencils, ready for applying in Eqs 2.3.8–2.3.9. Once the Poisson equation is solved, the corrected velocities and pressures are computed using Eqs. 2.3.8–2.3.9. The temperature and other scalars are advected and the time sub-step is completed. The algorithm outlined above only transposes one 3D array, instead of three velocity fields, making it very efficient. Figure 2.5 shows a schematic of the data arrangement and the transposes needed to implement the algorithm. We wish to highlight that this algorithm also uses all possible combinations of data transposes. It can be seen from Fig. 2.5 that the x to z transposes and the z to x transposes need a more complex structure, as a process may need to transfer data to other processes which are not immediate neighbors. The non-overlapping of data before and after transposes is most striking for e.g. process 10 in figure 2.5 with no overlap at all between x and z oriented pencils. These transposes are absent in the 2DECOMP library on which we

	Slab		Pencil	
	Halo	A2A	Halo	A2A
\mathbf{u}^* computation	2	6	2	0
Pressure correction	8	2	10	6
Scalar equation	3	2	2	0
Total	13	10	14	6

Table 2.1: Number of communications necessary for the computation of all the terms per timestep of the different codes. Here, A2A is short for all-to-all communications. Halo updates involve updating all halo cells, which requires more, but smaller, communications in the case of the pencil code. The difference between the details of the halo and all-to-all for the slab and pencil codes have not been taken into account. It can be seen that the pencil code contains the majority of the communications in the pressure (Poisson) solver.

build. These transposes have been implemented using the more flexible all-to-all calls of the type ALLTOALLW, instead of the all-to-all MPI calls of the type ALLTOALLV used for the other four transposes. A complete list of the used libraries can be found in Table 2.2.

2.6 Computational performance

For optimal scaling conditions, each processor should have an equal amount of work, and the communication to computation ratio should be minimal. In our case, as we do not have iterative solvers, each grid point has the same amount of work, and there is perfect load balancing. We also reduce the communication as far as possible. Not only the number of all-to-all communications are reduced, but also the halo communications as the halo is only one grid point wide. Table 2.1 presents the reduction in the number of communications when going from the slab decomposition with fully implicit viscous terms to the pencil decomposition with semi-implicit viscous terms. It is worth noting that the communications are not exactly the same: halo updates involve communications to four neighbors in the pencil decomposition, while only two neighbors are involved in the slab decomposition. However, the size of the halos is relatively smaller, so less data is transferred. Conversely, for the all-to-all communications, not all processes are involved in the pencil code, while all processes take part in the slab code. The memory consumption of the code, for double precision arithmetic, is approximately $M \approx 15 \times 8 \times N_x \times N_y \times N_z$.

Here M is the total used memory in bytes of all processes without MPI overhead. The number of allocated 3D arrays is 14, with additional 1D and 2D arrays of which the memory consumption will not exceed that of one 3D array in the intended cases with large grids.

The left panel of figure 2.6 shows the strong scaling of the code for 2048^3 and 4096^3 grids on Curie Thin Nodes system. Linear scaling can be seen up to 32K cores for the 4096^3 grid, with some scaling loss for 64K cores. The right panel of figure 2.6 shows the weak scaling of the code for 2^{23} points from 2 to 16K cores. The data in these plots is obtained by using only MPI parallelism, but hybrid OpenMP/MPI schemes are also available in the code. The choice between pure MPI or hybrid OpenMP/MPI depends heavily on the system on which the code is running. In addition, the presence of OpenMP will allow for a faster porting of the codes to a GPU architecture, in case it becomes viable for our application.

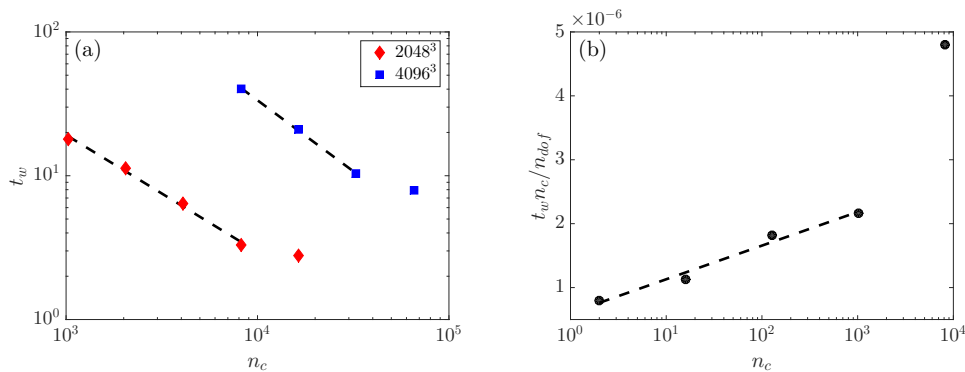


Figure 2.6: a) Strong scaling of the code for 2048^3 (red diamonds) and 4096^3 (blue squares) degrees of freedom n_{dof} . Here n_c is the number of cores used. The dashed lines indicate linear behaviour. The walltime per timestep t_w is accounted for a full timestep, i.e. three subimesteps when using the RK3 integrator. b) Weak scaling of the code for 8.3 Million (2^{23}) points per core. The dashed is a linear fit to the corresponding data points.

2.7 Summary and prospects

In this chapter, we have presented a parallelization scheme of a second-order centred finite difference method with minimal communication. Only six transposes are needed for every fractional timestep, and for large enough grids, the code's strong scaling is linear up to 32K cores, with slight performance loss from 64K cores. We emphasize that 64K cores is almost half the total number

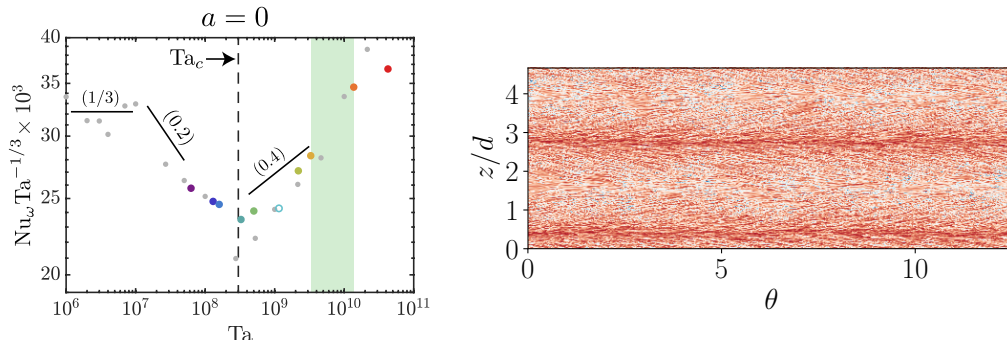


Figure 2.7: Left: Compensated Nusselt number as a function of the driving strength Ta for the case of pure inner cylinder rotation $a = 0$ at $\eta = 0.91$. The gray data points correspond to DNS from [106, 107]. In addition, each colored marker at fixed Ta corresponds to the experiments of chapter 4. The open circle in light blue corresponds to the DNS data of the current study for $\Gamma = 2.33$. The black solid lines serve as a reference to indicate the corresponding scaling. Right: Instantaneous azimuthal velocity at a distance $r = 0.0006$ from the wall for $Ta = 10^{10}$, for a pure inner cylinder rotation case. Red and blue colors indicates positive and negative velocity respectively.

of cores of the Curie Thin nodes system. The code will probably scale well for even larger grids (8096^3) on systems with larger amount of cores, as do similar codes based on the 2DECOMP library [1].

The performance of this code allows simulation of flows at high driving. For the application to Taylor–Couette flows, we refer to figure 2.7, where on the left panel we show the angular momentum flux Nu_w as a function of the driving Ta , also reported in chapter 4. In this way it has been possible to analyze the scaling laws of the $Nu_w(Ta)$ curve for pure inner cylinder rotation with an excellent agreement between the numerics and the experiments, revealing clear changes in the scaling exponent. As a quantification of the computational demand of the code: the highest $Ta = 10^{10}$ data point has a cost of 500000 CPU–hours, on 1.5 billion grid points. The prospected analysis of TC is not limited to global quantities such as the momentum flux. The highly parallel I/O and high resolution facilitates the study of local quantities. An unfiltered snapshot of the temperature field close to the inner cylinder wall for $Ta = 10^{10}$ is shown in the right panel of figure 2.7, where the small scale velocity fluctuations that are required to be properly resolved, can be seen. These small scales can straightforwardly be studied using using spectral analysis, or

Purpose	Library
I/O	HDF5
FFT	FFTW (Guru interface)
Linear algebra	BLAS, LAPACK/MKL/ESSL/LibSci/ACML
Distributed memory parallelism	MPI + 2DECOMP
Shared memory parallelism	OpenMP

Table 2.2: The used libraries for the specified purposes are indicated in this table.

other techniques.

As we can see, the use of this code in Refs. [107, 112] but also in the present manuscript has already allowed us to push the limits in Taylor–Couette simulations to $\text{Re} \sim \mathcal{O}(10^5)$, never simulated previously. Its use in future TC and RB simulations is expected to allow us to achieve the large driving required for entering the “ultimate” regime. The scheme, in combination to a multiple resolution strategy for the scalar field [110], has been used for simulating double diffusive convection [177], achieving the driving parameters relevant for oceanic convection. Due to the flexibility of finite difference schemes, we expect to be able to build further additions on to this code. The possibility of adding a Lagrangian phase, which can be either tracers, one–way or even two–way coupled particles is detailed in Ref. [142]. Other possibilities include adding rough walls using immersed boundary methods [179], or adding mixed Neumann–Dirchelet boundary conditions.

Chapter 3

Dynamics and evolution of Turbulent Taylor rolls

Based on: Francesco Sacco, Rodolfo Ostilla-Mónico & Roberto Verzicco, 'Dynamics and evolution of Turbulent Taylor rolls', *Journal of Fluid Mechanics*, 870, 970-987, 2019.

3.1 Introduction

Taylor–Couette (TC) flow, the fluid flow between two coaxial, independently rotating cylinders, is one of the paradigmatic systems of fluid dynamics, and a model system for studying the influence of rotation and curvature on turbulence [53]. Historically, this system has been heavily researched from the 1890s up to the present day, uncovering interesting phenomena for a system that even at the lowest Reynolds numbers is extremely rich. Taylor–Couette flow is linearly unstable when angular momentum decreases with radius, and different configurations of inner and outer cylinder rotation lead to diverse dynamics [6]. Large–scale structures arise because of instabilities and can fill the entire gap between the cylinders remaining relatively stationary in time. These structures, known as Taylor rolls or Taylor vortices [150], have been observed both in experiments and simulations, and dominate the flow topology up to the highest values of Reynolds number [74, 59, 107]; here the Reynolds number Re is defined as $Re = Ud/\nu$, with U a characteristic shear velocity of the cylinders which will be defined, d the distance between the cylinders and ν the kinematic viscosity.

The phase diagram of Taylor rolls is quite complex, and strongly dependent on the kind of rotation of the two cylinders. In the case of outer cylinder rotation and for a fixed or only slowly rotating inner cylinder, Taylor–Couette flow is linearly stable. On the other hand for pure inner cylinder rotation the centrifugal driving forces make the system unstable as the Reynolds number of the inner cylinder increases. At Reynolds numbers just beyond the onset of linear instability ($Re \sim 10^2$), Taylor rolls appear and are stationary and axisymmetric [6]. For increasing Reynolds number, secondary instabilities arise, and the Taylor rolls develop azimuthal oscillations, entering the wavy Taylor Vortex flow regime [62]. Further increasing the Reynolds number causes the onset of time–dependence, and this is known as the modulated wavy Taylor Vortex regime. When increasing the driving even more, even if the large coherent rolls are still present, the flow becomes chaotic as turbulence starts to develop, first in the bulk, and eventually also in the boundary layers as they undergo a shear transition [107]. This is the so–called turbulent Taylor vortex regime. For Reynolds numbers exceeding $Re \sim 10^3$, the small–scale vortices begin to be strong enough to weaken the large–time–scale circulation. For pure inner cylinder rotation, [74] found experimentally that the rolls disappear for $\eta = 0.714$ and $Re > 10^5$, where $\eta = r_i/r_o$ is the radius ratio of the two cylinders, with r_i (r_o) the inner (outer) cylinder radius. When the Reynolds number becomes sufficiently large, the flow recovers a statistical symmetry in the axial direction. The vanishing of the rolls at $\eta = 0.714$ was also found

numerically in [107], albeit for smaller aspect ratios $\Gamma = L_z/d$, where L_z is the axial length of the domain, d is the gap between the two cylinders.

When both cylinders rotate, the dynamic of the rolls becomes more complicated. By adding a slight counter-rotation to a $\eta = 0.714$ TC system, [59] found that the turbulent Taylor rolls survive at least up to $Re \sim 10^6$. Numerically, [108] observed rolls in the corresponding counter-rotation parameter regimes in DNS simulations for $\eta = 0.714$ and $\Gamma = 2.07$, from the formation of the axisymmetric rolls at low Reynolds number, up to the turbulent Taylor rolls. [108] also explored the phase space for the rolls in the high Reynolds number regime, showing that they can either fill the entire gap, partially survive close to the inner cylinder or completely disappear from the bulk depending on rotation and curvature of the system. Even if a smaller aspect ratio was used, wide agreement was found between the experimental and numerical probes of the counter-rotating regime.

The transition between two stages of the phase diagram in our previous analysis is far from smooth, and the continuity we have assumed between the steady, axisymmetric vortices near the onset of centrifugal instability to the large- Re turbulent Taylor rolls is not totally clear. Several questions remain: first, Taylor rolls have been traditionally attributed to the effects of centrifugal instabilities. However, for pure inner cylinder rotation, they appear to be strongest for narrow-gap (i.e. small curvature) instances of Taylor-Couette flow [107]. For high curvature ($\eta = 0.5$), they survive only at mild counter-rotation [165]. If they were caused solely by centrifugal effects, one could expect them to be always the strongest for the largest centrifugal driving, i.e. pure inner cylinder rotation, and this is not the case.

In this chapter we first intend to clarify the reason for this discrepancy by simulating small-gap Taylor-Couette flow at moderate Reynolds numbers and varying the curvature. By approaching TC flow with zero curvature, and analyzing its transition to rotating plane Couette flow (RPCF), the flow between two infinite and parallel plates moving at different velocities, we will study how the linear instabilities of TC flow relate to those of processes only driven by shear. This idea has already been used in the literature to study solutions of plane Couette flow: by the use of homotopy, [103] was able to continuously deform a low Reynolds number Taylor vortex from a TC solution for counter-rotating cylinders into a narrow gap onto a RPCF solution; [46] studied the narrow gap limit of TC flow, showing how the linear instability that leads to the formation of Taylor vortices is superseded by the planar shear flow transition as the curvature vanishes.

In a shear-driven flow, e.g. plane Couette flow, with linear instabilities absent, turbulence is regenerated by the self-sustaining process (SSP) first character-

ized by [176]. The cycle, detailed in section 3.3.2, consists of three steps, and each of these is necessary to maintain turbulence [61, 54]. Recently, a relationship between Taylor vortices at low curvature and the SSPs of shear flows was found by [37], who showed that at low Reynolds numbers the transition from Taylor vortex flow to wavy-vortex flow is caused by the activation of one of the phases of the SSP: the formation of the streak instability. And once the azimuthal waves arise on the rolls, their non-linear interaction feeds the rolls, closing the SSP. In this chapter, we intend to show how the flow behaves as the Reynolds number increases and to check if imprints of this behaviour can still be seen.

A second question that calls for explanation is about the axial pinning of the rolls. While this comes about naturally in experiments due to the presence of end-plates, in direct numerical simulations it is still not clear why structures should be fixed in a homogeneous direction, and the broken symmetry is not recovered in a statistical sense. Several numerical studies have been conducted to check that the axial pinning of the rolls is not an effect of small computational boxes due to aliasing of long-wavelength modes onto the streamwise-invariant mode [109, 111], finding no apparent effect of box-size on the rolls up to box sizes of $20\pi h \times 2h \times 9\pi h$, with h the half-gap. However on one side it has been found that for what would be considered large boxes, i.e. the DNS simulations in a domain of size $20\pi h \times 2h \times 6\pi h$, with h the half-plate distance by [8], or the $18\pi h \times 2h \times 8\pi$ domain of [118], no pinned structures appeared. On the other side a recent numerical work by [79] has shown that in plane Couette flow structures become pinned in a comparable large computational box of $20\pi h \times 2h \times 5\pi h$ for high Reynolds number.

It thus seems that it is impossible to neglect the effect of computational domain size, and in this chapter we set out to show in a more rigorous manner than simply showing visualizations as done previously [109, 111], how effects of finite domain sizes on structures can be quantified by increasing the azimuthal extent of the simulation domain.

The chapter is organized as follows: in section 3.2 we describe the numerical method used and the parameter setup used in the simulations. All the properties and the characterization of Taylor rolls are reported in section 3.3. In section 3.4 we briefly summarize and give some remarks and an outlook for future works.

3.2 Numerical details

We perform direct numerical simulations of Taylor–Couette flow by solving the incompressible Navier–Stokes equations in a rotating reference frame:

$$\frac{\partial \mathbf{u}}{\partial t} + \mathbf{u} \cdot \nabla \mathbf{u} + 2\boldsymbol{\Omega} \times \mathbf{u} = -\nabla p + \nu \nabla^2 \mathbf{u}, \quad (3.2.1)$$

$$\nabla \cdot \mathbf{u} = 0, \quad (3.2.2)$$

in cylindrical coordinates, where p is the pressure, t is the time, \mathbf{u} is the velocity, $\boldsymbol{\Omega} = \Omega_{r_f} \mathbf{e}_z$ is the angular velocity of the rotating frame around the central axis. Here, Ω_{r_f} is the mean angular velocity and \mathbf{e}_z is the unit vector in the axial direction. Spatial discretization is performed using a second–order energy–conserving centered finite difference scheme, while time is advanced using a low–storage third–order Runge–Kutta for the explicit terms and a second–order Adams–Bashworth scheme for the implicit treatment of the wall–normal viscous terms. Further details of the algorithm can be found in [172, 163]. The code has been extensively validated for Taylor–Couette flow [107] and is parallelized using MPI directives.

Axially periodic boundary conditions are taken with a periodicity length L_z , expressed non–dimensionally as an aspect ratio $\Gamma = L_z/d$, where $d = r_o - r_i$ is the gap between both cylinders, and r_i (r_o) the radius of the inner (outer) cylinder. For this study, we fix $\Gamma = 2.33$, which is enough to fit a single roll pair, so that their wavelength λ_z will be $\lambda_z = \Gamma = 2.33$. The non–dimensional radius ratio $\eta = r_i/r_o$ provides a measure of the curvature of the system, and is the second geometrical control parameter. In the azimuthal direction, Taylor–Couette is naturally periodic. However, a rotational symmetry of order N is imposed on the system with a double purpose: to reduce computational costs and to explore the effect of the the streamwise periodic length on turbulent structures. In this study, we mainly consider rotational symmetries between 5 and 20. For $\eta = 0.909$, a rotational symmetry of $N = 20$ results in a streamwise periodicity length of around 2π half–gaps, the usual value considered for the turbulent channel flow. We note that while [6] found azimuthal waves of wavenumber $m = 2$ near the transition to wavy Taylor vortex flow at similar radius ratio, the moderate Reynolds number simulations of [109] show very rapid drops in the streamwise decorrelation length. Indeed, $N = 20$ was found to be enough for pure inner cylinder rotating Taylor–Couette in [109] and [111] to obtain asymptotic torque and mean statistics, compared to the largest extents of $N = 5$.

We perform the simulations in a convective reference frame [41] such that

the cylinders rotate with opposite velocities $\pm U/2$, and any combination of differential rotations of the cylinders are reflected as a Coriolis force. In this frame the two control parameters become a shear Reynolds number $Re_s = Ud/\nu$ and a non-dimensional Coriolis parameter $R_\Omega = 2d\Omega_{rf}/U$; if we consider the traditional Reynolds numbers that measure the dimensionless velocity of the inner and outer cylinders in the laboratory frame of reference $Re_i = r_i\omega_i d/\nu$ and $Re_o = r_o\omega_o d/\nu$, where ω_i and ω_o are the angular velocities of the inner and outer cylinders, we can express the new control parameters as follows:

$$Re_s = \frac{2}{1+\eta}(Re_i + \eta Re_o), \quad (3.2.3)$$

$$R_\Omega = (1-\eta)\frac{Re_i + Re_o}{Re_i - \eta Re_o}. \quad (3.2.4)$$

In order to compare Taylor–Couette system in the limit of a vanishing curvature, also a few simulations of Plane–Couette flow have been performed, since it is the limit of Taylor–Couette flow when $\eta \rightarrow 1$. For this case we have used a Cartesian version of the previously mentioned code [163]. In the convective frame, the control parameters Re_s and R_Ω naturally reduce to those of rotating Plane–Couette flow when that limit is taken.

Temporal convergence is assessed by measuring the difference in torque between both cylinders. The flow is started from a white noise configuration, and run for approximately $tU/d = 1000$ time units to overcome the transient. The simulations are then advanced until the time average of the respective values are equal within 1%, which roughly corresponds to an additional $tU/d = 200$ time units. The torque is then taken as the average value of the inner and outer cylinder torques. Therefore, the error due to finite time statistics can be estimated to be around 1%. A complete discussion of temporal time-scales is available in [112]. The spatial resolution of lower Re_s simulations is based on [111]. For $Re_s = 3.61 \cdot 10^4$, we take the criteria $\Delta z^+ \approx 5$, $\Delta x^+ = r\Delta\theta^+ \approx 9$ and $\Delta r^+ \in (0.5, 5)$, resulting in resolutions of $n_\theta \times n_r \times n_z = 384 \times 512 \times 768$ in the azimuthal, radial and axial directions respectively for $N = 20$. For simulations in which we halve N , we double the resolution in the azimuthal direction.

3.3 Results

3.3.1 Changes in the rolls with Reynolds number

In order to analyze the properties of the large scale structures, we have performed several simulations fixing the cylinder radius ratio to $\eta = 0.909$, and increasing the driving by rotating the inner cylinder only and varying the Reynolds number Re_s between 10^2 and $3.6 \cdot 10^4$, thus covering the full range between linear instability and turbulent rolls. Indeed, for all the cases, the axially pinned structures exist and fill up the entire domain. These Taylor rolls are known to redistribute angular momentum and have a visible large scale pattern [74, 112], as shown in the first two rows of Figure 3.1: if we look at the temporally and azimuthally averaged azimuthal velocity and azimuthal vorticity, indeed, we can see that the signature of the rolls is preserved for all cases. Following [21], Taylor rolls were analyzed with the terminology of thermal convection by [108], where it was shown that at both cylinder walls, there existed three types of areas: plume ejection regions, where the velocity was largely in the positive wall-normal direction, and turbulent plume-like structures would leave the cylinder, plume impact regions, where the velocity was largely in the negative wall-normal direction, and plume-like structures from the other cylinder would impact the wall, and wind-shear regions where the velocity was largely parallel to the wall, and plumes would be generated. In [106, 108], the plumes were related to herringbone-structures, or hairpin vortices, which can also be seen in the left panel of Figure 3.2.

In Figure 3.1, the two quantities show different behaviours: the mean azimuthal velocity preserves a similar pattern during all the transition, revealing the Taylor rolls and the two zones where the fluid detaches from the inner/outer boundary layer and impacts the opposite wall. Alternatively, the intensity of the azimuthal (streamwise) vorticity concentrates near the wall. While we could expect the axial (spanwise) vorticity to concentrate near the walls with increasing Reynolds number due to boundary layer thinning, the behaviour of the azimuthal vorticity is more complicated. If there were no secondary flow, one could expect the mean azimuthal vorticity to average out to zero. In contrast, if secondary flows were present, as for example in the case of square-duct flow [119], azimuthal vorticity would be largely concentrated not only in the boundary layers but also in the *core* of the secondary structures. For Taylor-Couette flow with inner cylinder rotation, the azimuthal vorticity in the boundary layer becomes much higher than that of the core of the secondary flow, i.e. the Taylor roll. For this to happen, the mean flow velocity of the secondary motion must be relatively constant with Reynolds number,

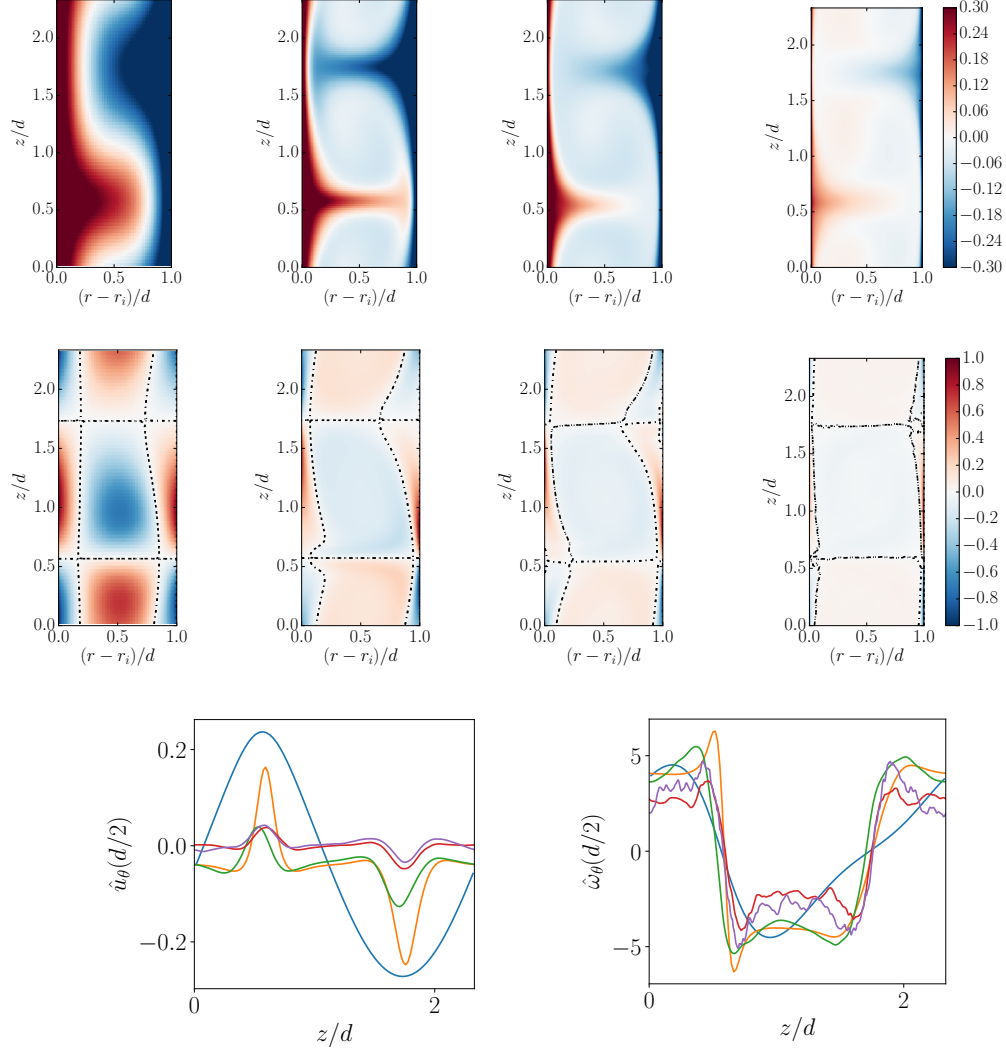


Figure 3.1: Temporally- and azimuthally averaged azimuthal velocity \hat{u}_θ (top row) and normalized averaged azimuthal vorticity $\hat{\omega}_\theta / \max |\hat{\omega}_\theta|$ (middle row) for inner cylinder rotation and several shear Reynolds numbers (from left to right, $Re_s = 1.96 \cdot 10^2$, $1.37 \cdot 10^3$, $4.97 \cdot 10^3$, $3.61 \cdot 10^4$) at $\eta = 0.909$ and $\Gamma = 2.33$. Contours levels for vorticity are shown for values between -0.001 and 0.001, to highlight the roll structures. The panels on the bottom row show two quantities, azimuthal velocity (left) and azimuthal vorticity (right) at the mid-gap $r = d/2$ for Reynolds numbers $Re_s = 1.96 \cdot 10^2$ (blue), $1.37 \cdot 10^3$ (orange), $4.97 \cdot 10^3$ (green), $3.61 \cdot 10^4$ (red) and $1 \cdot 10^5$ (purple).

and the boundary layer of the secondary motion must become thinner. This results in a relative “emptying” process of the bulk of the rolls. It is possible to see this process in the last row of figure 3.1, where in the right panel we have

checked the magnitude of the mean streamwise vorticity in the core of the rolls, i.e. at the mid-gap, along the spanwise coordinate. We can clearly see that, while at low Reynolds number of $Re_s = 1.96 \cdot 10^2$ the peak is located in the very core of the roll, already during the transition to ultimate regime the center of the structure is “deflating”, and vorticity starts to concentrate at the borders of the structure. This condition is enhanced at the highest Reynolds numbers $Re_s = 3.61 \cdot 10^4$ and $Re_s = 1 \cdot 10^5$, where the relatively constant value of azimuthal vorticity drops. This fact shows that other processes are taking place. As a consequence rolls become relatively more quiescent and inactive even if some circulation remains in the secondary flow cores.

This matches previous intuition that as the Reynolds number increases and the flow reaches the ultimate regime, the rolls undergo a series of transitions. In [108], when the ultimate-regime was reached for pure inner cylinder rotation at $\eta = 0.714$, the rolls simply vanished. For $\eta = 0.909$, even if they persist, between the right-most upper panels at $Re_s = 3.61 \cdot 10^4$, corresponding to the so-called ultimate regime, and the panels at $Re_s = 4.97 \cdot 10^3$, the azimuthal velocity in the bulk can be seen to increase even if strong axial signatures are still present. The left panel of the last row of figure 3.1, representing the magnitude of the mean streamwise velocity in the core of the rolls, i.e. at the mid-gap, along the spanwise coordinate, is a confirmation of this fact: even if, as we have already said, the profile of each velocity preserves the concentrated shape due to fluid detaching/impacting pattern, there is a velocity value jump in correspondence with the transition to the ultimate regime, between $Re_s = 4.97 \cdot 10^3$ and $Re_s = 3.61 \cdot 10^4$, that somehow matches the drop of azimuthal vorticity in the core seen in the right panel.

This calls into question the assumption that turbulent Taylor rolls before the ultimate regime such as those in [6], and those in the ultimate regime such as those in [59] are generated by the same mechanisms. The continuity between the left and right upper panels becomes less apparent upon close examination, and it appears that fundamental changes happen as the rolls are becoming relatively empty of vorticity.

3.3.2 The Taylor roll in the context of the self sustained process

It thus seems useful to analyze the turbulent Taylor rolls in the ultimate regime not in the context of centrifugal instabilities, but instead in the framework of shear flows. For this aim we introduce the self-sustained process of shear flows. Following the argument of [176], we know that a self sustained process is composed of three main phases:

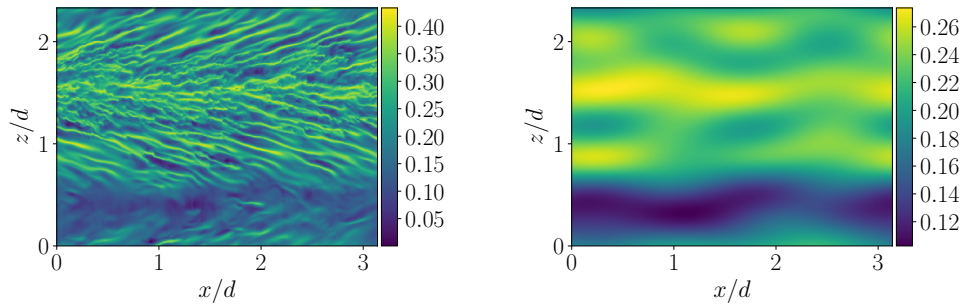


Figure 3.2: Left: Instantaneous visualization of the azimuthal (streamwise) velocity at $r^+ \approx 13$, for $Re_s = 3.4 \cdot 10^4$, $\eta = 0.909$ and $\Gamma = 2.33$. Right: Same velocity field as on the left under a low-pass filter. The characteristic undulatory streamwise instability of the streaks of the self-sustained process can be clearly seen.

- i) the redistribution of mean shear stress by streamwise rolls to create streaks;
- ii) the wake-like instability of the streaks;
- iii) the regeneration of the streamwise rolls from the nonlinear development of the streak instability.

In the previous section, we saw that Taylor rolls are essentially large-scale streamwise rolls which redistribute mean shear-stress. [37] showed that already at low Reynolds numbers, the axisymmetric Taylor roll was part i) of the self-sustained process, and once the transition to wavy Taylor vortices took place, all three parts of the process were active. With increasing Reynolds numbers, we expect the centrifugal (linear) instabilities to become bypassed by the shear instabilities [46, 16]. Thus for high Reynolds numbers we can expect aspects of the Taylor rolls to be related to parts i) and iii) of the SSP. We expect large-scale streaky structures to also exist for Taylor-Couette flow even in the turbulent regime. These structures would then feed the Taylor rolls and axially pinned Taylor rolls would simply be a fixed instance of the above self-sustained process.

A streaky flow would contain strong spanwise inflections. In the near-wall region of turbulent flows this will lead to two possible patterns, a typical staggered row of vortices and a less frequent horseshoe structure. To detect the existence of these spanwise variations, we have checked the instantaneous azimuthal velocity near the wall for pure inner cylinder rotation, and the

3.3 Results

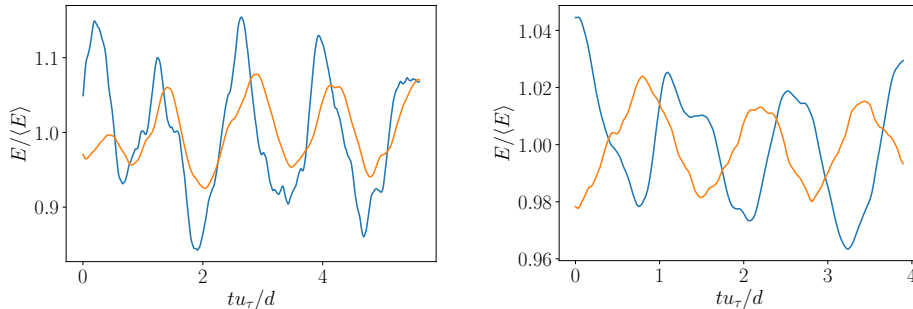


Figure 3.3: Left: Temporal evolution of the kinetic energy associated to streaks E_s (blue) and rolls E_r (orange) normalized by their mean value. Right: Temporal evolution of the normalized modal RMS velocity in the Fourier space associated to the $M(0, \beta)$ mode (blue) and the $M(0, 0)$ mode (orange). Both plots shown are for pure inner cylinder rotation with $\eta = 0.909$ and $Re_s = 3.4 \cdot 10^4$.

results are illustrated in figure 3.2. After applying a low-pass filter to the fields, the streaks-roll structure clearly comes up. This provides an initial indication that a Taylor roll in the ultimate regime is an axially pinned process reminiscent of the self-sustained process of shear flows.

A further assessment of the similarity between the two processes can be made by studying the temporal evolution of streaks and rolls. There are several definitions used in the literature to quantify the energy of streaks and rolls. First, we following the definition given by [37] of streaks and rolls in Taylor-Couette flow where their energy is calculated from the energy in axisymmetric modes.

For this, first of all we separate the field u from its mean U , averaged with respect to the streamwise coordinate θ :

$$u(t, \theta, r, z) = U(t, r, z) + u'(t, \theta, r, z), \quad (3.3.1)$$

and we take a further step by analyzing two derived quantities, the energy in the rolls:

$$E_r(t, \theta, r, z) = \frac{1}{2} \int_{r,z} [U_r^2(t, r, z) + U_z^2(t, r, z)] r dr dz, \quad (3.3.2)$$

and the energy in the streaks as defined by [37], which are defined through the axial anomaly, computed taking out the θ and z average of the field from U ,

$$E_s(t) = \frac{1}{2} \int_{r,z} [U_\theta(t, r, z) - \langle U_\theta(t, r, z) \rangle_z]^2 r dr dz. \quad (3.3.3)$$

This is shown in the left panel of figure 3.3, where the energy of both structures can be seen to oscillate at time-scales of $\mathcal{O}(u_\tau/d)$. The energy in the rolls can be seen to consistently lag behind the energy in the streaks by a small time, and this is probably due to the fact that they are regenerated through something analogous to step (iii) of the SSP cycle.

A second method to quantify the energy of streaks and rolls, and the link between the rolls and the SSP process is done following [54]. Here, the study of streaks and rolls is done through the modal r.m.s. velocity (or the square root of the ‘kinetic energy’), in the Fourier space, given by:

$$M(k_\theta = \alpha m, k_z = \beta n) = \left[\int_{r_i}^{r_o} \left(\widehat{u}_\theta^2(m\alpha, r, n\beta) + \widehat{u}_r^2(m\alpha, r, n\beta) + \widehat{u}_z^2(m\alpha, r, n\beta) \right) r dr \right]^{\frac{1}{2}}, \quad (3.3.4)$$

where $\alpha = 2\pi/L_x$ and $\beta = 2\pi/\lambda_z$ are the fundamental streamwise and spanwise wavenumbers, L_x corresponding to the streamwise domain extent, and λ_z as defined in section 3.2.

In particular we focus on the two principal modes:

- $M(0, 0)$, the axially and streamwise invariant mode, which represents the mean flow.
- $M(0, \beta)$ the streamwise independent, fundamental in z mode, corresponding to both streaks and rolls, as both u_θ and u_r/u_z add to the total energy in M .

In the right panel of figure 3.3 we see that the two energies oscillate at time-scales of $\mathcal{O}(u_\tau/d)$, and the period of the two quantities are almost anti-correlated, instead of the time-lag of the left panel. This is consistent with a breakdown-regeneration structure that resembles the one described in [54]. Energy is constantly being redistributed to the mean flow into streaks and rolls.

We note that [54] analyzed $M(\alpha, 0)$, which is invariant in the axial direction, and fundamental in θ . [54] states that this mode is responsible for rolls regeneration ([54], § 6), but in our simulations it evolves at faster time-scales and we do not see any positive or negative correlation between this mode and the two shown in figure 3.3(b). This indicates that we are not exactly seeing

the SSP as studied by [54], but instead observe a cycle which has properties reminiscent of it. As a final remark, both the plots of figure 3.3 are realized at $Re_s = 3.4 \cdot 10^4$, corresponding, as we already said, to the so called “ultimate regime”, but we have observed almost identical behavior of the energies and modal velocities at smaller Reynolds number ($Re_s = 5 \times 10^3$, during the transition to this regime).

Additional evidence for a general similarity between the rolls and the SSP is given by a previous study performed by [113] on decaying Taylor–Couette turbulence. In channel flow, the self–sustaining process regenerates itself with slow time–scales ($100tU/d$). Once forcing is removed, the vortices would regenerate themselves slower and slower but with the same intensity, until the turbulence died out [61, 54]. In the decaying Taylor–Couette simulations of [113], similar phenomena could be observed. The cylinders were made stress–free at $tU/d = 0$, thus removing the forcing from the rolls. The first life–stage of decay, attributed in the manuscript to the decay of the rolls lasted for a time–scale of $tU/d \approx 15 - 40$. The energy of the azimuthal (streamwise) velocity first decayed up to $tU/d \approx 10$, while the energy of the radial (wall–normal) and axial (span–wise) components did not start decaying up to $tU/d \approx 10$ and had a monotonic decay. This matches the findings of [61, 54]: the streamwise rolls are regenerated in full force in the first life–stage of decay until they completely die down and the flow enters the second life–stage of decay.

3.3.3 The pinning of Taylor rolls

If the Taylor roll is reminiscent of the self–sustained process, which is axially pinned, what is causing the pinning? Is it the instabilities caused by curvature, or can rotation alone cause the pinning of the rolls? To answer this question we have simulated several narrow–gap radius ratios up to the limit of $\eta \rightarrow 1$, i.e. the Plane Couette limit. By varying the curvature and keeping the other control parameters constant we can control for its effect. We set $Re_s = 3.4 \cdot 10^4$, in the ultimate regime [107]. The non–dimensional rotation parameter R_Ω is set to $R_\Omega = 0.1$, so we are considering weak anti–cyclonic rotation very close to the value for pure inner cylinder rotation at $\eta = 0.909$, which is $R_\Omega = 0.0909$. Analyzing the instantaneous and averaged azimuthal or streamwise velocity fields we find that large–scale structure analogous to Taylor rolls are present for all cases. The average and instantaneous flow–fields look very similar, so we expect them to be sustained by the same pattern of streaks that we have described previously. These facts are illustrated in the left and center panels of figure 3.4.

Moreover we have checked the magnitude of the rolls as curvature vanishes by looking at the magnitude of the Fourier component associated to them in the u_r-u_θ mean at the mid-gap: the axisymmetric mode in the streamwise direction ($k_x = 0$) and the axially/spanwise mode associated to the roll wavelength ($k_z = 2\pi/\lambda_z$). This is shown in the right panel of figure 3.4, where we can clearly see that the variations of this quantity are around 6% between $\eta = 0.909$ and $\eta = 1$. This matches the intuition coming from the Navier-Stokes equations that the strength of forces due to curvature is measured by the $R_c = d/\sqrt{r_i r_o}$ parameter [17], which corresponds to $R_c \approx 0.095$ for $\eta = 0.909$. This is further evidence that the nature of the rolls are similar in all the systems, and that their pinning is caused by rotation, and not curvature. Indeed, the Coriolis forces arising from solid body rotation, reflected non-dimensionally as R_Ω , seem crucial in controlling the regions of parameter space in which rolls form.

We note that while we use the word “pinning”, this is a simplification. Coriolis forces do not break the vertical translation symmetry of the problem. Instead, their presence modifies the rolls and adds a feature that makes them more resistant to spanwise translation when compared to the $R_\Omega = 0$ case. Large-scale structures are known to exist in non-rotating Plane Couette flow from the work of [156]. These were isolated in the simulations of [8], and found to consist of counter-rotating pairs of rolls with high vorticity in their boundaries. This pattern is similar to the structure of the Taylor rolls seen in figure 3.1. It is not curvature, but the addition of a mild anti-cyclonic rotation $R_\Omega = 0.1$ which breaks the spanwise wandering of these structures, resulting in the fixed rolls. Proof of this is seen not only in our simulations, where the rolls are barely modified as the curvature vanishes, and correspond to the structures of [8], but also in the large-box rotating Plane Couette simulations of [155] which show identical signatures for RPCF.

While in principle any rotating reference frame could be chosen to express a Coriolis force, obtaining a different expression for R_Ω , the choice of this particular one in which the velocities at the cylinders are equal and opposite is the correct way to reproduce the transition between TC flow and RPCF [17]. As the curvature increases, TC flow driven by pure inner cylinder rotation can be seen as TC flow driven by counter-rotating cylinders with an increasing solid-body rotation. The corresponding Coriolis force increases with increasing η , i.e. $R_\Omega(Re_o) = 1 - \eta$. With this Coriolis parameter R_Ω , we can revisit older data to show that mild anticyclonic rotation, and not centrifugal instabilities, play a defining role for moderate values of curvature. By recalculating the parameters in terms of R_Ω , we see that the $\eta = 0.714$ ($R_c \approx 0.33$) experiments of [59] show the signature of rolls between $R_\Omega \approx 0.1$

3.3 Results

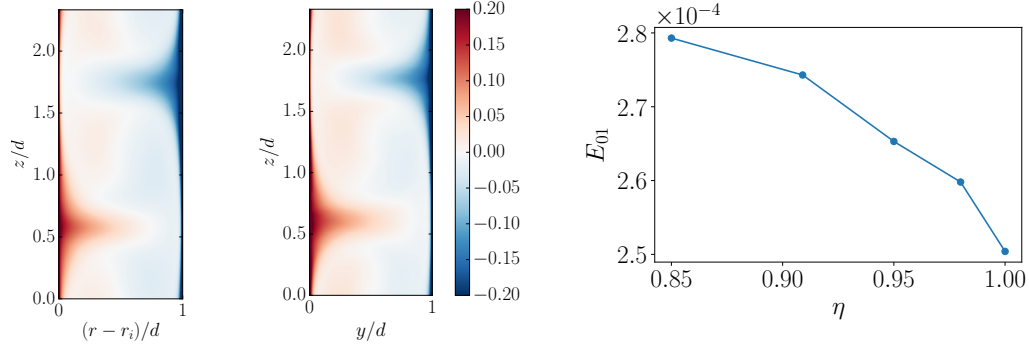


Figure 3.4: Left: Mean azimuthal velocity for Taylor–Couette at $\eta = 0.85$ and $R_\Omega = 0.1$, $Re_s = 3.4 \cdot 10^4$. Center: Mean streamwise velocity for plane Couette flow ($\eta \rightarrow 1$) at $R_\Omega = 0.1$, $Re_s = 3.4 \cdot 10^4$. Spanwise–pinned large–scale structures analogous to the turbulent Taylor rolls can be seen. Right: strength of the Fourier component associated to the turbulent Taylor roll at the mid–gap as a function of curvature for $R_\Omega = 0.1$, $Re_s = 3.4 \cdot 10^4$.

and $R_\Omega \approx 0.2$ when the cylinder counter–rotation is expressed as a Coriolis force, corresponding to the values discussed above. In the $\eta = 0.5$ ($R_c \approx 0.71$) experiments of [165], a fixed roll structure for counter–rotating cylinders was seen at $\omega_o/\omega_i = -0.2$, which corresponds to $R_\Omega = 0.25$, but not for pure inner cylinder rotation corresponding to $R_\Omega = 0.5$. This also serves to rationalize why the rolls vanish for pure inner cylinder rotation at $\eta = 0.5$ ($R_\Omega = 0.5$) and 0.714 ($R_\Omega = 0.286$), but not for 0.909 ($R_\Omega = 0.091$) as seen in [107]. Mild anti–cyclonic Coriolis forces and not centrifugal forces are the primary cause of the pinning of structures in the ultimate regime.

3.3.4 The effect of the domain size

From the previous sections, it seems apparent that mild anticyclonic rotation causes some self–organization in shear–flows by pinning the self–sustained process in the span–wise (axial) direction. However, while the pinning seemed natural for experiments, due to the presence of end–plates, it is still unclear what the effect of box–size is on simulations. As mentioned in the introduction, it has been found by numerical simulation of [79] that for plane Couette flow, a large computational box of $20\pi h \times 2h \times 5\pi h$, where h is half the distance between the walls, cause the pinning of flow structures. We note that this pinning was not observed either in the DNS simulations in a domain of size $20\pi h \times 2h \times 6\pi h$ by [8], nor the $18\pi h \times 2h \times 8\pi h$ domain of [118].

To probe the pinning of rolls, we decompose the velocity in a similar manner as in section 3.2 into mean flow and fluctuations. We return to the definition of streamwise averaged velocities $U(t, r, z)$ from Equation 3.3.1, and we take a further step, as in [101] by analyzing two derived quantities. First, we look at the axisymmetric azimuthal vorticity, which provides a measure of the circulation of the rolls:

$$\Omega_\theta = \frac{\partial U_r}{\partial z} - \frac{\partial U_z}{\partial r}. \quad (3.3.5)$$

and second, we look at the axisymmetric axial anomaly, computed taking out the θ and z average of the field from U , that was used by [37] (Eq. 3.3.3) to identify streaks:

$$U_s(t, r, z) = U(t, r, z) - \langle U(t, r, z) \rangle_z, \quad (3.3.6)$$

We first compare two TC systems, with $R_\Omega = 0.0909$, corresponding to pure inner cylinder rotation, with strong turbulent rolls, the other with $R_\Omega = -0.1$, corresponding to pure outer cylinder rotation, with fixed $Re_s = 3.4 \cdot 10^4$ and $\eta = 0.909$. As we previously discussed when analyzing Ω_θ field, large scale axially pinned rolls are present only with a mild anticyclonic rotation, and so are a characteristic of the first system only, while the second does not present this feature at all. This is also reflected on the streak fields U_s , as we have found also there large-scale axially pinned structure, only for inner cylinder rotation, while they are completely missing in the other case. This is displayed in the left and central panels of figure 3.5.

Moreover if we look closer at the central panel, we can see that the axial signature of the rolls has a well defined shape and an influence also in the bulk, analogous to what was seen for the azimuthal velocity in subsection 3.3.1. This is further proof that different mechanisms are taking place, and that Taylor rolls are part of an axially pinned process reminiscent of the SSP: the Coriolis forces are also pinning the streak fields, which in turn reinforces the rolls, keeping them fixed.

We now compare the effect of the azimuthal domain size on the two cases, to further prove that the rolls are not simply a product of aliasing, i.e. of large wavelengths mapped onto the streamwise invariant modes, caused by small domain extents. Even if recent studies have found that the computational domain (or box) size does affect the outline of the rolls [109, 111], since the axial extent of the box plays a crucial role on the correlations and spectra of the velocity field, no size of box was able to unpin the rolls. Moreover larger

3.3 Results

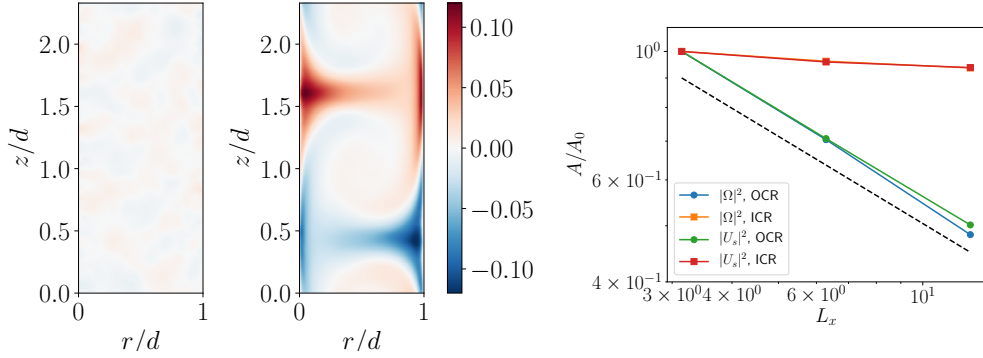


Figure 3.5: Left and center: Mean azimuthal velocity anomaly (U_s) for outer cylinder rotation (left) and inner cylinder rotation (center) at $Re_s = 3.4 \cdot 10^4$, $\eta = 0.909$. Right: Normalized energy of the streaks and rolls as a function of the streamwise domain length at the mid-gap $L_x/d = 2\pi(r_i + r_o)/(2dN)$ for the same values of Re_s and η for inner cylinder rotation (ICR) and outer cylinder rotation (OCR). The dashed line indicates the expected $A \sim L_x^{-1}$ behaviour for a structure-less flow where the energy comes from aliasing.

boxes in the azimuthal extent allow for azimuthal wave-like patterns in the Taylor rolls to develop, which affects the statistics in the bulk region, but does not unpin them anyway. The question remains of how large is “large enough”? Here, we attempt to rigorously quantify the effect of box-size to understand whether the presence of Taylor rolls is a product of numerics, since we are also imposing artificial rotational symmetry in the azimuthal direction. We can do this by systematically varying the azimuthal (streamwise) extent of the computational box. If the rolls are a product of aliasing, then, the energy of the rolls and streaks should decrease with box-size as $\sim 1/N$, as they are essentially a mean ($k_x = 0$). On the other hand, if they are physical, the energy should plateau to a constant with box-size.

We again use the comparison between pure inner rotating cylinder system and pure outer rotating one, as the last one, as we pointed out before, has a lack of roll structures. The simulations are performed with the same parameters, and varying the imposed rotational symmetry of the system between the values $N = 5, 10, 20$. In the right panel of figure 3.5 we show the streak and roll energies for both systems: for inner cylinder rotation we can see that even if the azimuthal extent of the domain change, the amplitude of rolls and streaks is almost constant; on the other hand for pure outer cylinder rotation the amplitude goes down with box-size as predicted for a mean mode.

As the last point we still want to understand if Taylor rolls are effectively fixed in the axial direction for all times or if they move about their position as a

random process. For this reason, we decompose the flow in low-wavenumber roll modes and high-wavenumber fluctuations, in the spirit of the generalized quasi-linear approximation [155]. We have already mentioned that the energy of the rolls is mainly contained in the axisymmetric ($k_x = 0$) mode, and the axial mode associated to the base wavelength of the roll ($k_z = 2\pi/\lambda_z$). By looking at the phase of the Fourier transform of the streamwise velocity u_θ at the mid-gap we can probe the extent of pinning. For the roll to move the phase of this mode, which we will denote from here as α , has to shift with time.

In the top left panel of figure 3.6 we show a visualization of the roll movement, with the predicted peak from the phase of the Fourier component superimposed. The method tracks relatively well the position of the minimum and maximum velocity. We note that an implicit assumption we make when using the Fourier mode, is that each of the two rolls behaves in a symmetric manner, which might not be strictly the case.

On the top right panel we show the time evolution of the phase for pure inner cylinder rotation cases at $Re_s = 3.4 \cdot 10^4$ and $\eta = 0.909$, with a varying imposed rotational symmetry between the values of $N = 5, 10, 20$. The +movement of the rolls can be seen to become smaller for increasing box-size. We also show the temporal autocorrelation of the roll phase in the middle left panel of 3.6, where it can be seen that the spatial changes decorrelate in time, with the decorrelation time increasing as the streamwise extent of the domain increases. Thus the drifts become both longer in time and shorter in space with increasing domain size.

Furthermore, we can measure the amplitude of the phase change (i.e. the speed of the drift of the roll) $d\alpha/dt$, and calculate the probability distribution function (p.d.f.) of this quantity. This is shown in the middle right panel. The drifts are approximately symmetric, as could be expected by the symmetries in the system. In the bottom right panel, we show the three curves normalized by their standard deviation and compared to a standard Gaussian distribution. The three curves can be seen to approximate the Gaussian distribution with their standard deviation, i.e. the size of the spatial drifts, decreasing with increasing domain size.

It thus seems that the spatial drifts not only become shorter, but they also become more correlated with increasing domain size. This can be reasoned as follows: all non-linear interactions are triadic interactions of low or high wavenumber modes. A force that could shift the phase has to come from the interaction of two high-wavenumber fluctuations, that is, from a triadic interaction of the form $\hat{u}'(k_1), \hat{u}'(k_2) \rightarrow \hat{U}(k_1 + k_2)$. If we now assume that fluctuations are random, and centered at zero, using the central limit theorem

we expect that the mean of all triadic interactions affecting the roll behaves like a Gaussian. We also expect that an increase in the computational box, which adds more modes to the averaging, makes the expected value of the fluctuations approach zero. In the bottom left panel of figure 3.6 we show the standard deviation of the drift, which approaches zero even faster than $1/\sqrt{L_x}$, that is what would be expected from a simple random process. This is an indication that the phenomenon is more complicated than what could be predicted from this simple analysis, but anyway the pinning process holds and works stronger than our expectation.

Overall, the results verify reasonably well our expectations. We have shown that rolls are moving, but this movement depends on the box-size: the larger the domain the smaller the spatial variations. Computational effects cannot be completely avoided. Indeed, boxes which are very large might pin structures by the averaging out fluctuations over long spatial extents.

3.4 Summary and conclusions

Several DNS simulations have been performed in a large parameter range of Taylor–Couette system in order to better understand the high–Reynolds number behaviour of the large–scale structures known as Taylor rolls. We have shown that, at a fixed radius ratio $\eta = 0.909$, these structures become more and more empty of vorticity in the bulk as the Reynolds number increases, while the behaviour of the streamwise velocity remains somewhat similar, leaving behind the characteristic imprint in the axial direction on both instantaneous and mean fields. In a way similar to the rolls, large–scale streaky structures arise in the azimuthal (streamwise) direction. At high Reynolds numbers the roll/streak pairs can be understood in the context of a spatially localized instance of a process reminiscent of the self–sustained process of shear flows: the primary mechanism for the generation is not the centrifugal instabilities caused by rotation and curvature, as previously thought [111]. Instead, streaks are generated by the redistribution of shear stress by the rolls, and their instability sustains the evolution of the same rolls. For a narrow gap system, the self–sustained process is pinned under the presence of moderate anti–cyclonic rotation. The pinning is not due to destabilizing centrifugal effects, as the process remains pinned in the plane Couette limit value $\eta \rightarrow 1$, i.e. for no curvature. The R_Ω parameter range where the rolls are pinned matches previous experimental results from large–gaps between $\eta = 0.5 - 0.714$. Finally, we have shown that the rolls are not a product of aliasing due to small computational domains, and their position appears to

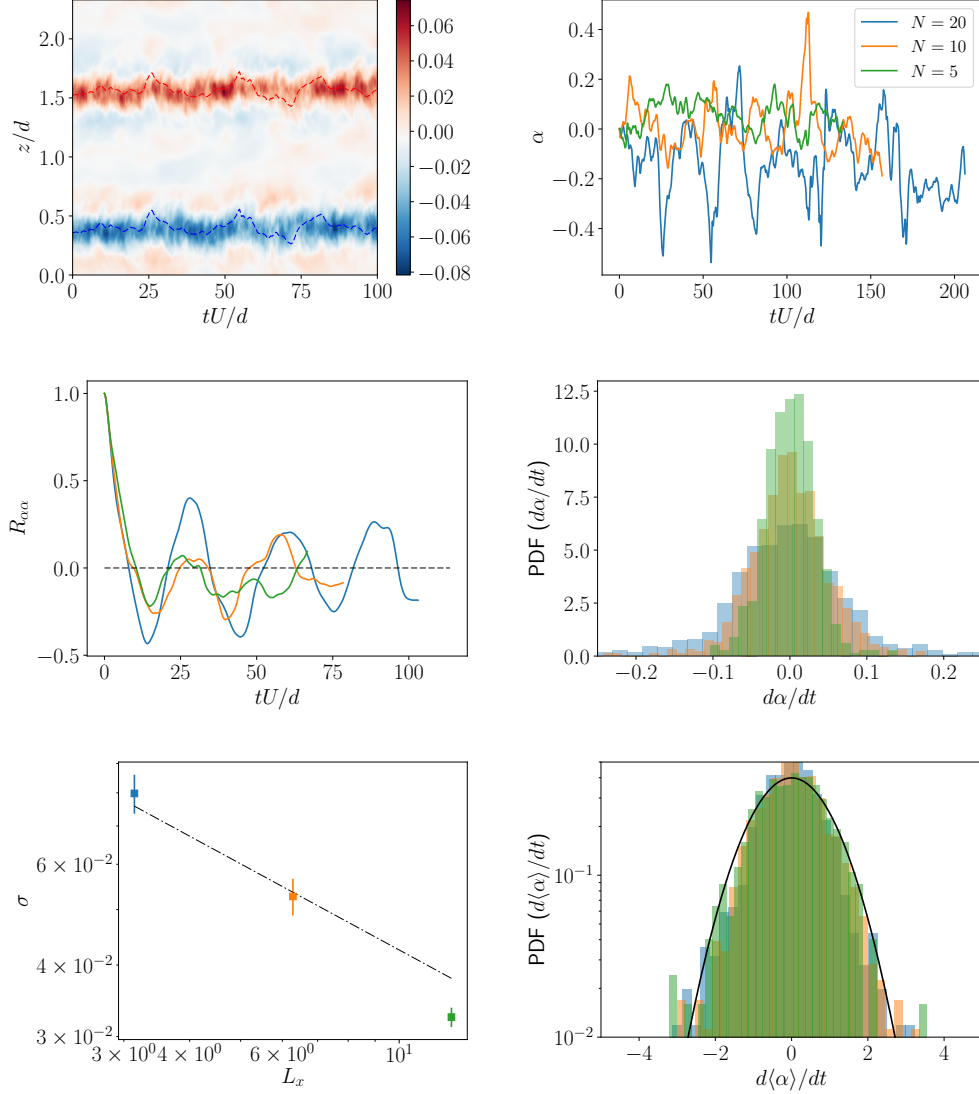


Figure 3.6: Top left: Space–time (Hovmöller) diagram showing the streamwise–averaged azimuthal velocity at mid–gap for $N = 20$ at $Re_s = 3.4 \cdot 10^4$, $\Gamma = 2.33$ and $\eta = 0.909$. The position of the maximum and minimum velocities of the Taylor–roll Fourier mode is shown with a dashed line. Top right: Phase (α) of the Fourier mode associated to the Taylor roll for three different azimuthal (streamwise) domain lengths . Middle left: Temporal auto–correlation of the phases for the three domains. Middle right: Probability distribution function for the phase velocity ($d\alpha/dt$) for the three simulations. Bottom left: Standard deviation of the phase velocity as a function of streamwise domain extent $L_x = 20\pi/N$. The dashed line shows the proposed $1/\sqrt{L_x}$ behaviour. Bottom right: The three probability distributions of (d) normalized by their standard deviation with a Gaussian distribution overlaid.

3.4 Summary and conclusions

change, governed by a random process with long time-scales. The smaller the domain, the larger the change in position of the rolls, because the average of the triadic interactions between fluctuations deviates more from zero. Further investigation should look at the role of the rotation parameter R_Ω on other important parameters, as torque, and on the velocity field, in order to understand when Taylor rolls have an optimal flow, and the effects that rotation and curvature have on large scales, whether alone or coupled.

Chapter 4

Double maxima of angular momentum transport in small gap $\eta = 0.91$ Taylor-Couette turbulence

Based on: Rodrigo Ezeta, Francesco Sacco, Dennis Bakhuis, Sander G. Huisman, Rodolfo Ostilla-Mónico, Roberto Verzicco, Chao Sun, & Detlef Lohse, ‘Double maxima of angular momentum transport in small gap $\eta = 0.91$ Taylor-Couette turbulence’, in preparation.

4.1 Introduction

Taylor–Couette (TC) flow, the flow in between two coaxial, independently-rotating cylinders, has successfully been used as a model for shear flows to study instabilities, flow patterns, nonlinear dynamics and transitions and turbulence [149, 25, 6, 81, 115, 168, 107, 47, 53]. The basic TC geometry is characterized by two parameters: the first is the radius ratio $\eta = r_i/r_o$, where r_i and r_o are the inner and outer radii, respectively. The second is the aspect ratio $\Gamma = L/d$, where L is the height of the cylinders and $d = r_o - r_i$ is the width of the gap. The shear driving of the flow is produced by the cylinders differential rotation and, in dimensionless form, is expressed by the Taylor number [43]

$$\text{Ta} = \frac{(1 + \eta)^4 d^2 (r_o + r_i)^2 (\omega_i - \omega_o)^2}{64\eta^2 \nu^2}, \quad (4.1.1)$$

where $\omega_{i,o}$ are the inner and outer angular velocities, respectively and ν is the kinematic viscosity of the fluid. The second control parameter is the rotation ratio

$$a = -\omega_o/\omega_i, \quad (4.1.2)$$

where $a < 0$ denotes corotation of the cylinders while $a > 0$ indicates counter-rotating cylinders. The value of $a = 0$ corresponds to the case of pure inner cylinder rotation.

We note that instead of describing the control parameters of TC flow with Ta , η , and a , one could alternatively describe the parameter space in a convective reference frame as proposed by [41] such that the cylinders rotate with opposite velocities $\pm U/2$ and the entire system then rotates with angular velocity $\vec{\Omega} = \Omega_{rf} \vec{e}_z$ around the central axis. Here, $\Omega_{rf} = (r_i \omega_i + r_o \omega_o)/(r_i + r_o)$ is the mean angular velocity and \vec{e}_z is the unit vector in the axial direction. This way any combination of differential rotations of the cylinders is parametrized as a Coriolis force. In this frame the two control parameters are the shear Reynolds number Re_S for the driving strength, the curvature number R_C , and the rotation number R_Ω :

$$\text{Re}_S = \frac{Ud}{\nu} = 2r_i r_o \frac{d|\omega_i - \omega_o|}{(r_i + r_o)\nu}, \quad (4.1.3)$$

$$R_C = \frac{(1 - \eta)}{\sqrt{\eta}}, \quad (4.1.4)$$

$$R_\Omega = \frac{2\Omega_{rf}d}{U} = (1 - \eta) \frac{r_i \omega_i + r_o \omega_o}{r_i \omega_i - r_o \omega_o}. \quad (4.1.5)$$

We remark that $\text{Re}_S \propto \sqrt{\text{Ta}}$, and that the rotation number R_Ω is connected with the negative rotation ratio a by:

$$R_\Omega = (1 - \eta) \frac{1 - a/\eta}{1 + a}. \quad (4.1.6)$$

While the choice of one set of parameters might seem arbitrary at first, we note that R_Ω is the quantity that controls the magnitude of the Coriolis force when the equations are written in the rotating reference frame, and it becomes in particular relevant to elucidate certain effects, especially in the limit of low curvature [17].

In statistically stationary TC flow, the flux of angular momentum $J^\omega = r^3(\langle u_r \omega \rangle_{A,t} - \nu \partial_r \langle \omega \rangle_{A,t})$ is exactly conserved [43]; here u_r is the radial velocity, ω the angular velocity of the fluid, r is the radial coordinate and the symbol $\langle \cdot \rangle_{A,t}$ denotes a time average on a cylindrical surface coaxial with the cylinder axis. This transport quantity is independent of r ; any flux going through an imaginary cylinder of radius r also goes through any other imaginary cylinder, or mathematically $dJ^\omega/dr = 0$. The response of the system can then be characterized by normalizing J^ω with its value for non-vortical laminar flow $J_{\text{lam}}^\omega = 2\nu r_i^2 r_o^2 (\omega_i - \omega_o)/(r_o^2 - r_i^2)$, which gives rise to the pseudo-Nusselt number in TC flow [43],

$$\text{Nu}_\omega = \frac{J^\omega}{J_{\text{lam}}^\omega}. \quad (4.1.7)$$

The key scientific question is to accurately describe the transport throughout the parameter space, i.e. $\text{Nu}_\omega = \text{Nu}_\omega(\text{Ta}, \eta, a, \Gamma)$. For low Ta , the boundary layers remain laminar and as a consequence Nu_ω effectively scales roughly as $\text{Nu}_\omega \propto \text{Ta}^{1/3}$ [53]. In the ultimate regime of turbulence, in which both boundary layers and bulk are turbulent, we have $\text{Nu}_\omega \propto \text{Ta}^{1/2}/\log \text{Ta}$ [52]. The transition to the ultimate regime happens when the boundary layers undergo a shear instability and has been observed at $\text{Ta} \approx \text{Ta}_c = 3.0 \times 10^8$ for small and medium gaps ($\eta \geq 0.714$) [57, 107, 53]. For large gaps, where curvature dominates, the transition is postponed to large values of Ta , i.e. $\text{Ta} \approx 10^{10}$ for $\eta = 0.5$. If one estimates the logarithmic correction, a theoretical estimate for the effective scaling $\text{Nu}_\omega \propto \text{Ta}^{0.4}$ is obtained at around $\mathcal{O}(\text{Ta}) \approx 10^{10}$, which has been confirmed experimentally and numerically. We note that even if the value of Ta for which the transition to the ultimate regime depends on the radius ratio η and the rotation ratio a , the $\text{Nu}_\omega(\text{Ta})$ effective scaling is not affected by these parameters after the transition [115, 168, 96, 107].

While the rotation ratio does not affect the effective scaling $\text{Nu}_\omega \propto \text{Ta}^{0.4}$, it has a strong effect on the proportionality constant. The rotation ratio

influences the organization of the flow and increases or decreases the angular momentum transport Nu_ω . For a fixed geometry (η), and constant driving strength (Ta), a maximum in angular momentum transport (Nu_ω) can be found for a certain rotation ratio denoted a_{opt} [168, 115, 53]. For the case $\eta < 0.9$, the maximum has been associated to the strengthening of the large-scale wind [167, 15, 59] and the presence of turbulent intermittent bursts originated from the BLs [167]. Beyond the point of optimal transport $a > a_{\text{opt}}$, when the counter-rotation is strong, the stabilizing effect of the outer cylinder leads to the detachment of mean vortices from the outer layer which leads to intermittent structures in the radial directions, and decreases the overall angular momentum transport [15].

The value of a_{opt} depends on the curvature of the flow, ranging from $a_{\text{opt}} \approx 0.2$ at $\eta = 0.5$ [96] to $a_{\text{opt}} \approx 0.4$ at $\eta = 0.714$ [59]. Ostilla-Mónico et al. [106] showed that as η increases starting from 0.5, a_{opt} becomes larger, corresponding to a system with stronger counter-rotation. However, as η increases, the peak becomes broader. To disentangle the effect of the rotation ratio a from the curvature of the flow, Brauckmann et al. [17] numerically studied the transition from TC flow to rotating plane Couette flow (RPCF), namely the limit $\eta \rightarrow 1$ in a small-aspect ratio domain. In this limit it is more informative to look at the rotation of the cylinders as expressed by R_Ω . When expressed in terms of R_Ω , the asymptotic value (for $\eta \rightarrow 1$) of $R_{\Omega,\text{opt}}$ remains approximately constant. On the other hand in the limit $\eta \rightarrow 1$, $a(\eta)$ converges to $a = 1$ in a rotationless system, and to $a = -1$ for all the other cases, showing that for this parameter the transition between TC flow and RPCF is singular (see [17] for further details). Strikingly, Brauckmann et al. [17] find that for $\eta > 0.9$ (low curvature), not one maximum of angular momentum transport is present, but two. The first peak, located in the corotating regime, was described as the broad peak. It is associated with strong vortical motions, as evidenced by the radial velocity fluctuations which show a maximum at optimal transport [17]. The second peak, denoted as the narrow peak, was found for counter-rotating cylinders. It appeared only when the driving is sufficiently large, and it was speculated that it supersedes the broad peak for sufficiently large driving.

The appearance of two peaks for small gaps means that several competing mechanisms for the formation of the optimum momentum transport must exist, and that these become blurred for large gaps as the stabilizing effects due to curvature add a third factor. By analyzing the $\text{Nu}_\omega(a)$ relationship using R_Ω as a control parameter, Brauckmann et al. [17] were able to show that the peaks appearing in the counter-rotating regime at $\eta = 0.5$ and $\eta = 0.714$, and the broad peak for corotating cylinders for $\eta > 0.8$ basically were the same phenomena, as they both contained strong ordered motions and fell in

the same R_Ω range. As this peak survives the limit of vanishing curvature, it becomes clear that intermittency originated from the stabilizing effect of the OC does not explain its origin. Instead, Brauckmann and Eckhardt [16] divided the TC system into three sub-systems in the spirit of Malkus [89]: the bulk, and the two boundary layers representing marginally stable TC systems. With this simple model, they were able to predict the location of the broad peak in R_Ω space, finding good agreement for the prediction at moderate Ta . Using the same argument, Brauckmann and Eckhardt [16] also predicted that the shear in the boundary layers, and hence their transition to turbulence, depends not only on the absolute shear driving, but also on the rotation ratio, which was corroborated by experiments. In this way, they explained the appearance of the narrow peak as an enhancement of angular momentum transport in certain regions of parameter space caused by the “early” transition of the BLs to turbulence. Brauckmann and Eckhardt [16] also argued that the narrow peak will dominate the broad peak once the centrifugal instabilities are superseded by shear instabilities, and only one peak would be visible as in [106]. This was postulated to happen once the BLs become turbulent for the value of a in the broad peak. [16] predicted this to happen at $Ta > 4.95 \times 10^9$, close to the transition to the ultimate regime for that η .

In this study we set out to globally and locally probe the angular momentum transport in a wide range of driving strength $10^7 \leq Ta \leq 10^{11}$ for the case of low curvature $\eta = 0.91$, focusing in particular in the Ta range $10^8 \leq Ta \leq 10^{10}$, where the transition to the ultimate regime happens, and where Brauckmann and Eckhardt [16] observed the appearance of two peaks for angular momentum transport using numerical simulations. The main motivation of this study is to elucidate the link between the change in behaviour of the $Nu_\omega(\Gamma)$ dependence [95], the vanishing of the broad peak, and the changing role of vortical motions [132] which all happen around this transition. We will use an experimental setup with very large aspect ratios Γ , which allows for the flow to switch between states, i.e. different roll wavelengths. By doing this, not only can we experimentally confirm the appearance of multiple angular momentum optima in TC flow, which has not been reported yet, but we can also study the transition between regimes dominated by narrow and broad peaks. We will also rule out that they are an effect of artificially constraining the flow to small periodic aspect ratios: switching between two and three-roll states for varying driving was already reported in [106], and this could have an effect on the two peaks.

Secondly, we will test the predictions of Brauckmann et al. [17] and Brauckmann and Eckhardt [16] regarding the mechanism underlying the occurrence of

both peaks. Is the broad peak related to vortical motions, which are strengthened by centrifugal forces? Is the narrow peak a consequence of shear? And if so, will it overtake the broad peak and if so, at what turbulence level? By carefully examining the regime where the boundary layers transition, we can better explore the mixed dynamics arising when centrifugal effects and shear are competing side-by-side and further understand what is happening at the transition to the ultimate regime. To address these questions we conducted both experiments (torque and local velocity measurements) and Direct Numerical Simulations (DNS).

The structure of the chapter is as follows. In section 4.2, we explain the experimental methods. In section 4.3, we introduce the numerical details of the simulations. In section 4.4, we experimentally study the global response of the flow throughout a large parameter space of Ta and a . In particular, we reveal transitions and local maxima of the angular momentum transport. In section 4.5, we complement the experimental findings with numerical simulations and discuss in detail how the size and shape of the Taylor rolls changes with varying the rotation parameter R_Ω . The final section 4.6 contains the conclusions and an outlook for future works.

4.2 Experimental setup and measurement procedure

4.2.1 Setup

The experiments were carried out in the Twente Turbulent Taylor-Couette facility (T³C) [168]. In this apparatus, the ratio η and aspect ratio Γ can be adjusted by installing outer cylinders of different dimensions. In this study, the radius of the inner cylinder (IC) is $r_i = 200$ mm and the radius of the outer radius (OC) is set to $r_o = 220$ mm. As a consequence, the radius ratio is $\eta = r_i/r_o \approx 0.91$ and the aspect ratio results in $\Gamma = L/d = 46.35$, with $d = r_o - r_i = 20$ mm and $L = 927$ mm. Two acrylic windows located at the bottom cylinder, which cover the entire gap, allow for the capture of Particle Image Velocimetry (PIV) fields in the $r - \theta$ plane.

4.2.2 Global measurements: Torque

We measure the torque \mathcal{T} required to drive the cylinders at constant speed. This is done via a hollow flanged reaction torque transducer which connects the driving shaft and the inner cylinder. From the torque measurements, the

4.2 Experimental setup and measurement procedure

Working Fluid	(%) Glycerol	ν/ν_w	ρ/ρ_w
Mixture 1	58.72	18.20	1.18
Mixture 2	55.60	13.11	1.17
Mixture 3	45.39	5.67	1.13
Mixture 4	40.18	4.09	1.11
Water	0	1.0	1.0

Table 4.1: Properties of the different mixtures used in the experiments. The percentage of glycerol is based on volume. Both the density and kinematic viscosity ratios are calculated with respect to the density ρ_w and the kinematic viscosity ν_w of water at 21 °C. Data taken from Cheng [27].

Nusselt number can be calculated as follows

$$\text{Nu}_\omega = \left(\frac{r_o^2 - r_i^2}{2\nu r_i^2 r_o^2 \Delta\omega} \right) \left(\frac{\mathcal{T}}{2\pi \ell_{\text{eff}} \rho} \right), \quad (4.2.1)$$

where $\ell_{\text{eff}} = 536$ mm is the effective length along the cylinder where the torque is measured, the difference of angular frequencies is $\Delta\omega = 2\pi\Delta f = 2\pi(f_i - f_o)$ with $f_{i,o}$ the driving frequency of the inner and outer cylinder, respectively, and ρ the fluid density. Typically, the T³C facility operates in the ultimate regime of turbulence, where both boundary layers (inner and outer) are turbulent; in our case, where $\eta = 0.91$, this corresponds to a driving of $\text{Ta} > \mathcal{O}(10^8)$. Thus, in order to capture the transitional regime ($\mathcal{O}(10^7) < \text{Ta} < \mathcal{O}(10^8)$), we use working fluids with different values of the kinematic viscosity ν . The working fluid—depending on the desired range of Ta to be resolved—is a mixture of water and pure glycerol. The percentage of glycerol in the mixtures, along with its corresponding kinematic viscosity and density can be found in table 4.1. The liquid temperature is kept constant at 21 °C during all the experiments.

We probe the phase space of Nu_ω in two different ways. The first one is what we call an *a*-sweep, where the angular velocity difference $\Delta\omega$ and thus the driving strength Ta is kept constant and the angular velocity ratio $a = -\omega_o/\omega_i$ is varied. In this way, we can measure different states in the co- and counter-rotation regime while the driving (Ta) is fixed. The second type of experiments is the opposite i.e. a Ta -sweep, where a is fixed and $\Delta\omega$, and thus the driving strength Ta , is increased.

4.2.3 Local measurements: PIV

We seed the flow with polyamide fluorescent particles with diameters up to $\approx 20 \mu\text{m}$ with a seeding density of ≈ 0.01 particles/pixel. The emission peak of these particles is centered at $\approx 565 \text{ nm}$. We image the particles in the flow with an Imager SCMOS (2560×2160 pixel) 16 bit camera using a Carl Zeiss Milvus 2.0/100 objective. The illumination of the particles is provided by a Quantel Evergreen 145, 532 nm dual cavity pulsed laser. A cylindrical lens is positioned at the laser output to create a thin light sheet of $\approx 1 \text{ mm}$ thickness. A set of mirrors and a traverse system are installed which allows the laser sheet to move with the frame of the T³C (see figure 4.1). The laser beam (at the laser output) hits a first mirror which is tilted 45° . Light will then be redirect upwards towards a second mirror (also tilted at 45°) which redirects it finally towards the T³C, perpendicular to both cylinders. The second mirror is attached to the traverse system which can move freely in the axial direction. Since the traverse is fixed to the frame of the T³C, the result of this arrangement is no relative motion between the camera and the laser sheet due to mechanical vibrations.

The experiments require the OC to move freely; thus, a special trigger for the camera is used for the acquisition of the images. This triggering is done magnetically by magnets located on top of the OC and a Hall switch mounted onto the frame of the T³C which outputs a voltage signal every time the magnets pass by. Using this signal as a trigger, we are able to capture two fields (each one corresponding to one window in the bottom plate) per revolution of the OC. The camera is operated in double frame mode with a framerate f that depends on the rotation rates of the outer cylinder f_o . In all cases however $\Delta t \leq 1/f$, where Δt is the interframe time. In order to increase the contrast between the emission of the light from the particles and the background, we use an Edmund High-Performance Longpass filter 550 nm in front of the camera lens.

A total of 7 different flow states have been investigated using particle image velocimetry. These 7 flow states have different a and Ta , as reported in table 4.2 and—as will be shown later—correspond to the local maxima of the angular momentum transport as function of a for a variety of Ta . In total, 10 different heights were explored for each state, and 500 fields were recorded for each height. The normalized axial span Δz for all experiments is $\Delta z/L \approx 0.1$, which lies in the range $0.402 < z/L < 0.5$ (see figure 4.1). The movement of the laser sheet in the axial direction results in defocusing of the images, therefore the focus is adjusted accordingly for all the explored heights.

The velocity fields are measured in the $r - \theta$ plane and are computed by a

4.3 Setup of the direct numerical simulations

Experiments								
Ta	Re_s	a			R_Ω		Γ	
6.35×10^7	7.93×10^3	-0.58	-	0.80	0.351	-	0.006	46.35
1.33×10^8	1.15×10^4	-0.60	-	1.50	0.373	-	-0.023	46.35
1.63×10^8	1.27×10^4	-0.26	-	0.80	0.156	-	0.006	46.35
3.29×10^8	1.81×10^4	-0.30	-	0.80	0.171	-	0.006	46.35
5.10×10^8	2.25×10^4	-0.49	-	0.80	0.362	-	0.006	46.35
2.23×10^9	4.70×10^4	-0.33	-	0.80	0.183	-	0.006	46.35
3.31×10^9	5.78×10^4	-0.29	-	0.79	0.167	-	0.007	46.35
1.40×10^{10}	1.18×10^5	-0.60	-	1.50	0.373	-	-0.230	46.35
4.30×10^{10}	2.06×10^5	-0.30	-	1.00	0.171	-	-0.004	46.35
DNS								
Ta	Re_s	a			R_Ω		Γ	
5.10×10^8	2.25×10^4	-0.761	-	0.909	0.7	-	0	12.56
1.17×10^9	3.4×10^4	-0.761	-	0.909	0.7	-	0	2.33

Table 4.2: Experimental and numerical flow parameters used in this study. The first two columns show the driving, expressed as either Ta or Re_s . The third and fourth columns show the rotation parameters expressed as either a or R_Ω . The last column shows the aspect ratio Γ .

multi-pass algorithm using commercial software (Davis 8.0). The first pass is set to 64×64 pixels and the last one is set to 24×24 pixels with 50% overlap of the windows. The fields obtained are then expressed in cylindrical coordinates of the form $\vec{u} = u_r(r, \theta, t)\vec{e}_r + u_\theta(r, \theta, t)\vec{e}_\theta$, where u_r and u_θ are the radial and azimuthal velocities, respectively, which depend on the radius r , the angular (streamwise) direction θ and time t . Here, \vec{e}_r and \vec{e}_θ are the unit vectors in the radial and azimuthal direction, respectively.

4.3 Setup of the direct numerical simulations

In addition to experiments, we perform direct numerical simulation (DNS) using an energy-conserving second-order centered finite-difference code for the spatial discretization, while a fractional time-step advancement is adopted in combination with a low-storage third-order Runge-Kutta method. The complete description of the algorithm can be found in [172] and [163]. This code has been extensively used and validated for TC flows [107].

As mentioned in the introduction, we perform the simulations in a convective reference frame [41], determined by the parameters Re_s and R_Ω defined in

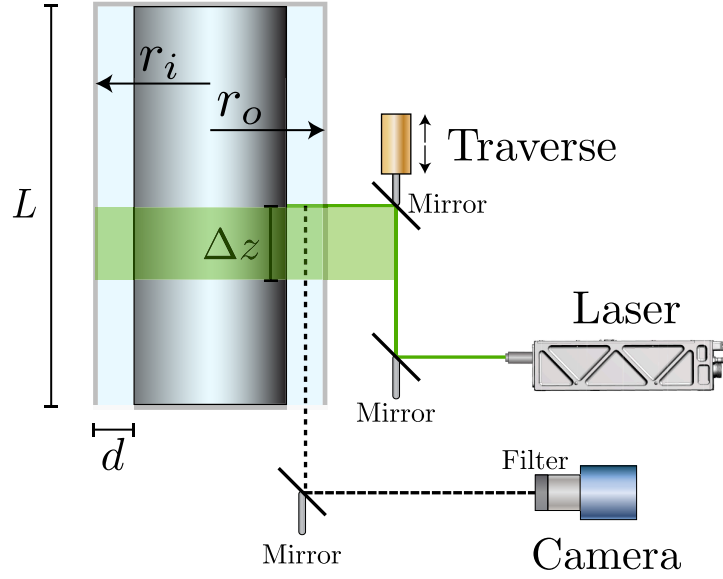


Figure 4.1: Sketch of the experimental setup. An arrange of mirrors is set such that the light sheet and camera are mounted on the frame of the T³C.

equations (4.1.3) and (4.1.5). According to this scaling the nondimensional incompressible Navier-Stokes equations read:

$$\nabla \cdot \mathbf{u} = 0, \quad (4.3.1)$$

$$\frac{\partial \mathbf{u}}{\partial t} + \mathbf{u} \cdot \nabla \mathbf{u} + R_\Omega \mathbf{e}_z \times \mathbf{u} = -\nabla p + Re_S^{-1} \nabla^2 \mathbf{u}. \quad (4.3.2)$$

We chose the same radius ratio $\eta = 0.91$ as in experiments, which is also the same as in the numerical simulations of Ostilla-Mónico et al. [106, 107]. We perform two sets of simulations with fixed Reynolds numbers, $Re_S = 2.25 \times 10^4$ and $Re_S = 3.4 \times 10^4$ (or $Ta = 5.10 \times 10^8$ and $Ta = 1.17 \times 10^9$) while varying R_Ω (or equivalently a). Axially periodic boundary conditions are taken with a periodicity length corresponding to the height of the cylinder L , and are expressed by the aspect ratio Γ . In the azimuthal direction, the system is naturally periodic; however, an imposed artificial rotational symmetry of order n_{sym} is chosen in order to reduce the computational costs.

We take two computational box-sizes. A small box similar to the one used by [14] with $\Gamma = 2.33$ and $n_{sym} = 20$. This small box is used for both values of Re_S , and is large enough to not affect the first-order statistics of the flow [109]. For the case of $Re_S = 2.25 \times 10^4$, we also run a medium-sized box with an aspect ratio of $\Gamma = 12.56$, and a rotational symmetry of $n_{sym} = 3$. This allows the flow some freedom to switch between different roll states, as in

[111]. A uniform discretization is used in the azimuthal and axial directions, while a Chebychev-type clustering near the cylinders is used in the radial direction. The spatial resolution for the small boxes at $\text{Re}_S = 2.25 \times 10^4$ and $\text{Re}_S = 3.4 \times 10^4$ was chosen as $n_\theta \times n_r \times n_z = 384 \times 512 \times 768$ in the azimuthal, radial and axial directions, which in wall units for the more restrictive case of $\text{Re}_S = 3.4 \times 10^4$ is a resolution of $\Delta z^+ \approx 5$, $\Delta x^+ = r\Delta\theta^+ \approx 9$ and $0.5 \leq \Delta r^+ \leq 5$. For the medium-size box at $\text{Re}_S = 2.25 \times 10^4$, a grid of $n_\theta \times n_r \times n_z = 1728 \times 384 \times 1728$ was chosen, which yields a resolution of $\Delta z^+ \approx 5$, $\Delta x^+ = r\Delta\theta^+ \approx 9$ and $0.4 \leq \Delta r^+ \leq 2.5$. In order to achieve temporal convergence, the simulations are run until the difference between the time-averaged torque of the inner and the outer cylinders is less than 1%. The torque is then taken as the average between these two values. The simulations are then run for at least 40 large eddy turnover times tU/d .

4.4 Transitions and local maxima in $\text{Nu}_\omega(\text{Ta}, a)$

4.4.1 Transitions in the $\text{Nu}_\omega(\text{Ta})$ scaling

First, we analyze the scaling laws of the $\text{Nu}_\omega(\text{Ta})$ curve for pure inner cylinder rotation in figure 4.2. The Nusselt number is compensated by the scaling of the classical regime, i.e. $\text{Nu}_\omega \text{Ta}^{-1/3}$ and plotted as a function of the driving strength Ta for pure inner cylinder rotation only ($a = 0$). We also include the DNS of Ostilla-Mónico et al. [107], and observe an excellent agreement between the numerics and the experiments. For values of the driving $\text{Ta} < 10^7$, the flow is still in the classical regime, where both BLs are still laminar, and an effective scaling of $\text{Nu}_\omega \propto \text{Ta}^{0.3}$ can be observed. When the driving strength is increased beyond $\text{Ta} = \mathcal{O}(10^7)$, the flow enters a transitional regime, with an effective scaling exponent α in $\text{Nu}_\omega \propto \text{Ta}^\alpha$ of $\alpha \approx 0.2$. If the driving is further increased, a minimum value of the compensated Nusselt number is reached at a critical Taylor number $\text{Ta}_c \approx 3.0 \times 10^8$, after which a clear change in the scaling exponent to $\alpha = 0.4$ can be seen. This indicates the onset of the ultimate regime, which coincides for experiments and numerics.

Figure 4.2 reveals also a second phenomenon, which was not previously reported in experiments. In [106], the local scaling-law was found to be $\text{Nu}_\omega \sim \text{Ta}^{0.4}$ for $\text{Ta} > 10^{10}$. Indeed, provided $\text{Ta} > \text{Ta}_c$, the local effective scaling-law appears to be the same, with one caveat: a “jump” in the curve around $\text{Ta} \approx 10^{10}$ can be seen, where the Nusselt number suddenly increases, even if the effective scaling is the same on both sides of the jump. The region where this occurs is highlighted in green in figure 4.2. [107] observed the jump in

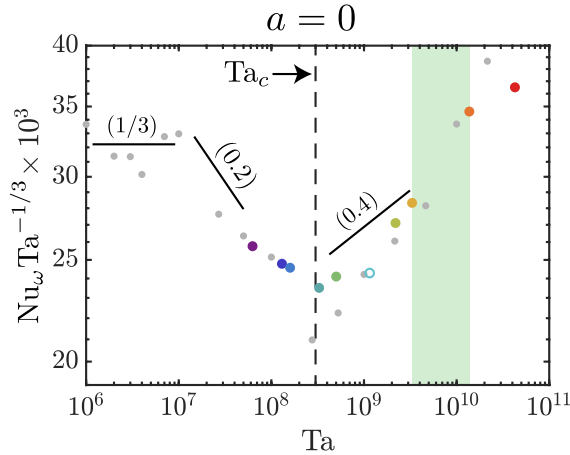


Figure 4.2: Compensated Nusselt number as a function of the driving strength Ta for the case of pure inner cylinder rotation $a = 0$ at $\eta = 0.91$. The gray data points ($Ta < 10^8$) correspond to DNS from [106]. The gray data points for $Ta > 10^8$ are also DNS simulations but from a different study [107]. In addition, each colored marker at fixed Ta corresponds to the driving variation as shown in the legend of figure 4.3c. The open circle in light blue corresponds to the DNS data of the current study for $\Gamma = 2.33$. The transition to the ultimate regime is observed at $Ta = Ta_c \approx 3 \times 10^8$ (vertical dashed line). The green shaded area corresponds to the region where a *jump* can be seen due to the disappearance of quiescent wind shearing regions. The black solid lines serve as a reference to indicate the corresponding scaling.

DNS simulations at $a = 0$, and attributed it to the sudden disappearance of quiescent wind shearing regions in the boundary layer. After this jump, the dependence of Nu_w on the roll wavelength was completely lost [109]. Here, we find evidence that experiments see a similar, sharp jump as observed in figure 4.2. This will be further investigated in section 4.5.1, where we will explore how this behaviour is seen across the a -range, and its effect on the local maxima of angular momentum transport.

4.4.2 Appearance and shifting of the local maxima

Once we allow the outer cylinder to rotate, we have a more complicated three-dimensional parameter space. In figure 4.3a, we show the Nusselt number as a function of the rotation ratio a for different Ta . This figure reveals—just as the DNS from Ostilla-Mónico et al. [106] and Brauckmann et al. [17]—that a very pronounced maximum of angular momentum can be found in

the corotating regime when the driving results $\text{Ta} < 1.33 \times 10^8$. However, as the driving exceeds the critical value Ta_c , we clearly identify two local angular momentum maxima: the first is located in the corotating regime at $a \approx -0.27$ and the second in the counter-rotating regime at $a \approx 0.46$. These turbulent states correspond to $R_\Omega = 0.16$ and $R_\Omega = 0.03$, which are similar to the values found by Brauckmann et al. [17] for $\eta = 0.91$. This measurement reveals that the two local angular velocity transport maxima for the same driving are not an artifact of the initial conditions or the finite extent of the domain of the numerics. As we further increase the driving beyond $\text{Ta} > 3.31 \times 10^9$, the maximum in the corotating regime (broad peak) vanishes, while the maximum in the counter-rotating regime (narrow peak) increases its magnitude. For the largest driving we explore ($\text{Ta} = 4.30 \times 10^{10}$), only one peak can be detected in the counter-rotating regime, although it is now less sharp. In order to highlight this trend, we show in figure 4.3b the compensated Nusselt number for four selected values of Ta . Again, note how the value of the driving dictates the occurrence of the maximum of angular momentum transport: if Ta is too small, only one peak can be found in the corotating regime. Conversely, if Ta is too large, only one peak can be observed albeit for counter-rotation. There is, however, a range of Ta which lies in between these two extremes, for which two maxima can be detected. In figure 4.3c, we show a 3D representation of the compensated Nusselt number as a function of a and Ta . In this figure, we included the experiments for fixed a , i.e. Ta -sweeps. Note how these experiments agree remarkably well with both the a -sweeps (shown in color) and the numerics, mutually validating each other. An animated version of figure 4.3c can be found in the Supplementary Material, where one can appreciate also the extent of the parameter space we explore. We finally note that for $\text{Ta} = 2.23 \times 10^9$ and $\text{Ta} = 3.31 \times 10^9$, discrete jumps in the $\text{Nu}_\omega(a)$ can be observed for $a < 0$. This observation can better be seen in figure 4.3a and will be revisited in §4.5.2 with the results from the numerical simulations.

In figure 4.4a, we show the location of the observed local maxima throughout the parameter space (a, Ta) . Here, we also include the DNS data of Ostilla-Mónico et al. [106] for the same radius ratio $\eta = 0.91$ albeit for much lower values of Ta . We note that as the driving increases from $\text{Ta} = \mathcal{O}(10^4)$ towards the critical Taylor number Ta_c , the peak for corotation moves towards $a = 0$. Past the transition, the location of this peak remains relatively stable at $a \approx -0.2$ until it vanishes. Regarding the peak for counter-rotation, we see that it only appears when $\text{Ta} > 10^8$ and moves as the driving increases. When $1.33 \times 10^8 \leq \text{Ta} \leq 1.17 \times 10^9$, the peak moves towards higher a values of counter-rotation. However, for $\text{Ta} > \mathcal{O}(10^{10})$, when only one peak is detectable, it

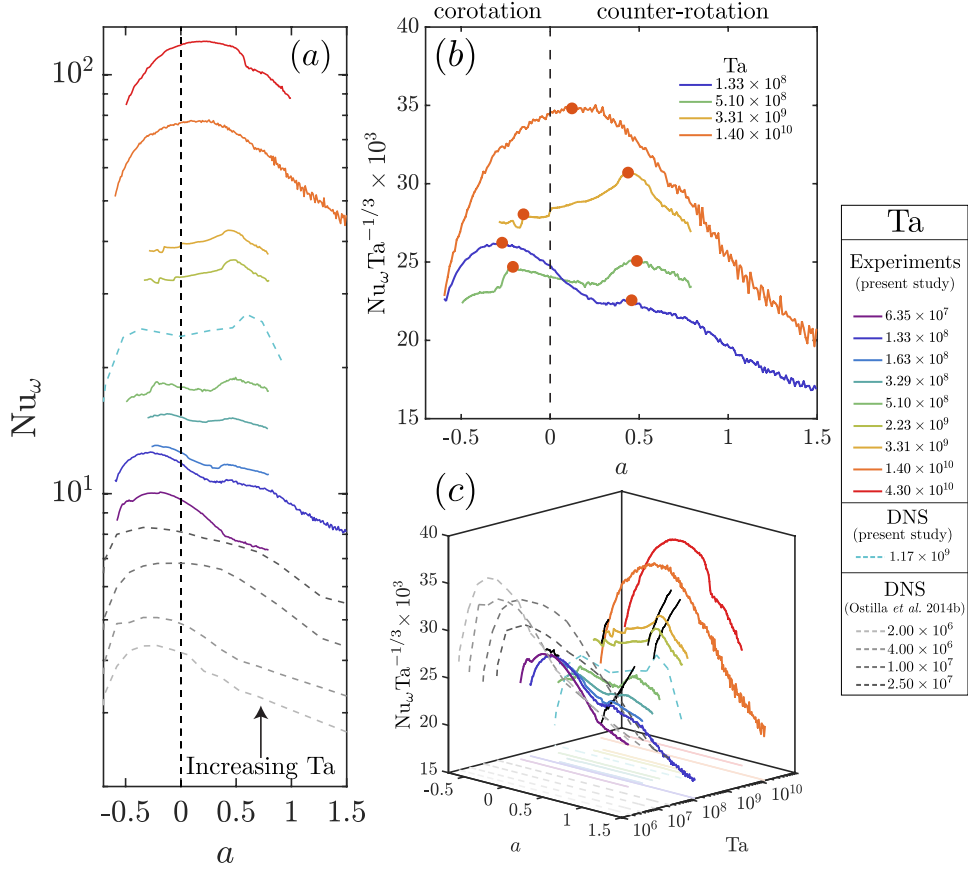


Figure 4.3: (a) Nusselt number Nu_ω as a function of rotation ratio a for different values of the driving Ta . (b) Compensated Nusselt number as a function of a for four selected Ta . Here, the solid red circles represent local maxima of angular momentum, where we perform PIV measurements as described in section 4.4.3. The vertical dashed line ($a = 0$) in both (a) and (b) separates the co and counter-rotating regimes. (c) A 3D representation of the compensated Nusselt number as a function of Ta and a . The black solid lines represent the experiments performed for fixed a , i.e. Ta -sweeps. In all figures, the solid lines represent experiments while the dashed lines represent numerics. The colors represent the variation in Ta as illustrated by the legend.

seems to move back towards $a = 0$. This side-effect of the disappearance of the broad peak means that the explanation by Brauckmann and Eckhardt [16] can be extended. We note, however, that at this driving, $Nu_\omega Ta^{-1/3}$ becomes less a -dependent which could over- or underestimate the precise location of the maximum. However, the shifting of the narrow peak is consistent with the asymptotic value of a_{opt} at large Ta from Ostilla-Mónico *et al.* [106] and happens around the same Ta for which the jumps in the $Nu_\omega(Ta)$ relation

4.4 Transitions and local maxima in $\text{Nu}_\omega(\text{Ta}, a)$

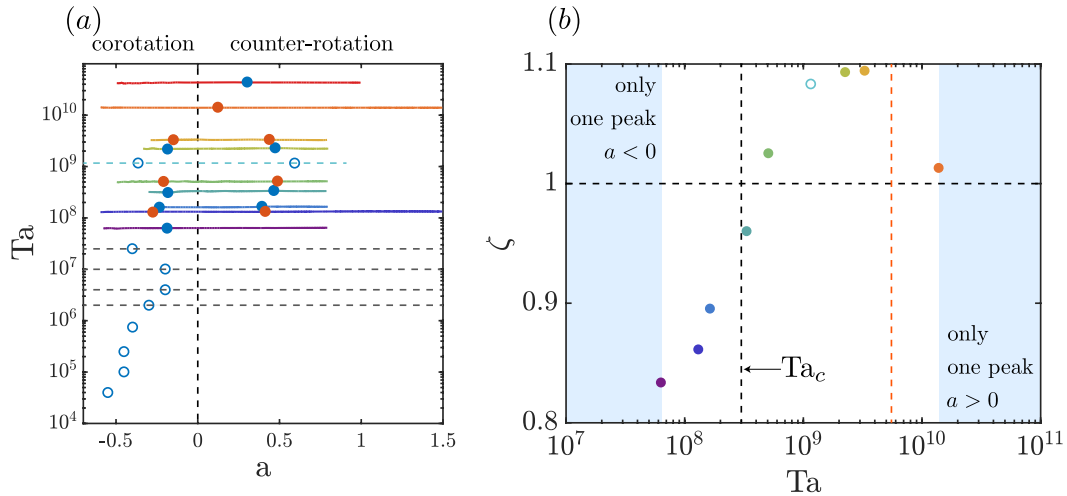


Figure 4.4: (a) Location in the phase space of the local maxima of angular momentum transport. The blue open circles for $\text{Ta} \leq 2.5 \times 10^7$ are the DNS of Ostilla-Mónico et al. [106]. The blue open circles located at $\text{Ta} = 1.17 \times 10^9$ are from DNS of the current study. The solid circles represent experimental data for the local maxima of angular momentum. The solid orange circles represent turbulent states where we perform PIV experiments as described in section 4.4.3 and shown in figure 4.3. (b) Ratios of the magnitude of the angular momentum transport peaks as defined in eq. 4.4.1. The colored points represent the experimental data. The open circle represents the DNS simulation shown in (a) for $\text{Ta} \approx 10^9$. The blue shaded areas represent turbulence levels wherein only one peak in angular momentum can be observed. The transition to the ultimate regime is observed at $\text{Ta} = \text{Ta}_c \approx 3 \times 10^8$. The vertical red dashed line represents the prediction of [16] for the disappearance of the (broad) peak found in corotation, namely at $\text{Ta} > 4.95 \times 10^9$.

appeared. The reasons for this behaviour will be revisited in §4.5.1.

Interestingly, the value of the driving ($\text{Ta} = 5.1 \times 10^8$) for which we detect two local maxima is close to the expected value of the transition to the ultimate regime, i.e. $\text{Ta}_c = 3 \times 10^8$, and that at this Ta , the relative magnitude of the peaks is very similar. In order to quantify this observation, we define the ratio of the magnitude of the peaks as

$$\zeta \equiv \frac{\text{Nu}_\omega(a = a_{\text{counter}})}{\text{Nu}_\omega(a = a_{\text{co}})}, \quad (4.4.1)$$

where a_{co} and a_{counter} denote the a -value that corresponds to the peak for co- and counter-rotation, respectively. In figure 4.4b, we report ζ as a function of Ta showing that for $\text{Ta} < \text{Ta}_c$ we have $\zeta < 1$, whereas for $\text{Ta} > \text{Ta}_c$ it

holds $\zeta > 1$. This yields an alternative representation of what was originally shown in figure 4.3: with sufficient driving the peak for counter-rotation will surpass the peak for corotation. As mentioned previously, the magnitude of both peaks seems to be nearly the same ($\zeta \approx 1$) close to the transition to the ultimate regime. This indicates the link between the appearance of the second peak, and the transitions of the boundary layer as postulated by Brauckmann and Eckhardt [16]. Furthermore, around the same values of Ta , the dependence of Nu_ω on the roll wavelength, and thus on Γ changes. This was seen as a crossing of the $Nu_\omega(Ta)$ curves for different values of Γ around the transition to the ultimate regime [95, 107]. That these phenomena occur all at the same time indicates the complex character of the transition to the ultimate regime.

Finally, we note that for sufficiently large driving ($Ta = 4.95 \times 10^9$), the narrow peak completely dominates and the broad peak can not be detected, as was also postulated by Brauckmann and Eckhardt [16]. At these values of Ta , [107] showed that the torque would no longer depend on roll wavelength, indicating again that the changes in the peak behavior are intimately linked to changes in the $Nu_\omega(\Gamma)$ relationships.

4.4.3 Local flow structure and its relation to the local Nu_ω maxima

In the previous section, we showed that the narrow peak (counter-rotation) will surpass the broad peak (corotation) for a given value of the driving. To further elucidate the mechanisms behind this phenomenon, we investigate the flow locally with PIV measurements. We explore a range of Ta which spans values before, close to and beyond the transition to the ultimate regime. For every driving, we investigate two flow states, namely where both the narrow and broad peaks are located as is shown in figure 4.3b and table 4.2.

We first investigate the strength of the radial flow by looking at u_r in the $(r - z)$ plane. In figure 4.5, we show $u_r(r, z)$ for both peaks, which are located in the corotating and counter-rotating regime, respectively, and as function of Ta . Here, we can clearly identify regions of negative and positive radial velocity along the axial direction which indicates the presence of Taylor rolls. Strikingly, we find that for all Ta explored, $|u_r|$ is much larger for corotation than for counter-rotation. This confirms what was shown numerically by Brauckmann et al. [17]: the broad peak (located for corotation) is accompanied by strong and coherent rolls.

In order to give a more quantitative picture of the strength of the rolls as a function of the driving, we look at the quantity

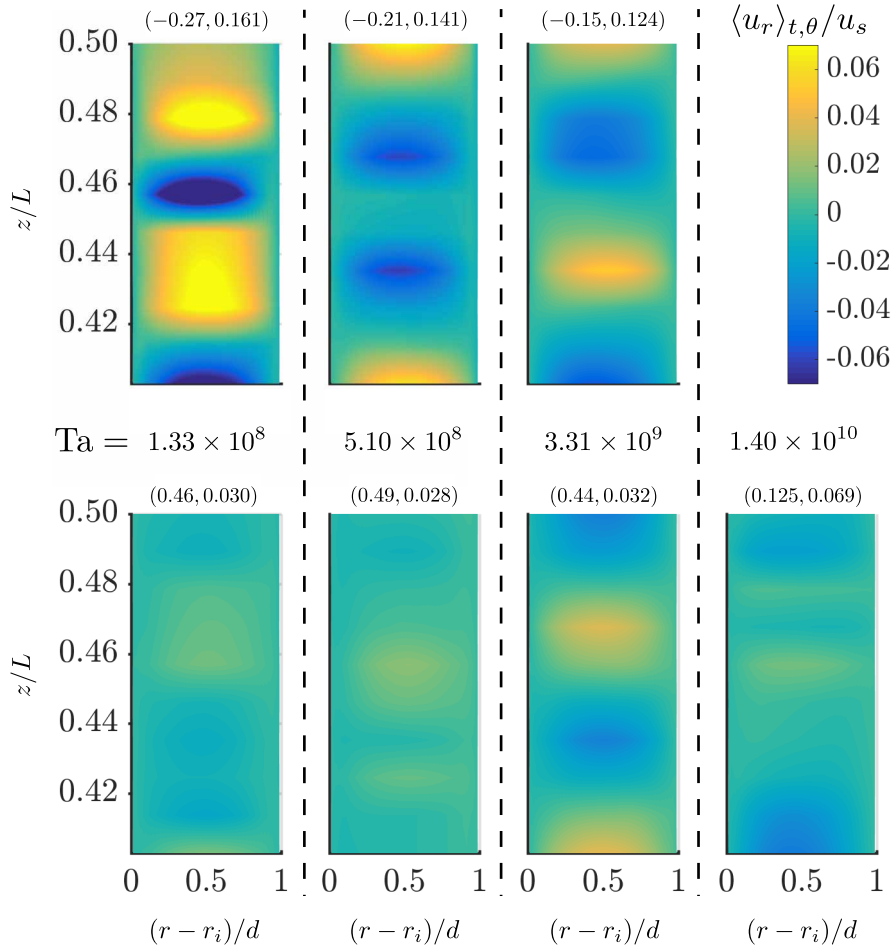


Figure 4.5: Azimuthally and time averaged normalized radial velocity obtained from PIV experiments as described in figure 4.3. The legend on top of each figure represents the value of (a, R_Ω) . The upper row represents measurements of the peak in the corotating regime while the bottom row shows measurements of the peak for counter-rotation. Along a single column, the Ta is fixed for both co- and counter rotating states. The dashed lines are added to emphasize the difference between the Ta values.

$$\text{RMS}(\tilde{u}_r) \equiv \sqrt{\langle (\langle u_r/u_s \rangle_{t,\theta,r_{\text{bulk}}})^2 \rangle_z}, \quad (4.4.2)$$

which is the root mean square (RMS) of the normalized radial velocity profile along the z -direction. Here, r_{bulk} denotes an average over the radial domain that defines the bulk region of the flow, namely $0.3 \leq (r - r_i)/d \leq 0.7$. Due to the presence of the vortical structures in the flow, the axial average has to be carefully carried out. For the cases at $a = -0.27$ and $a = -0.15$, and for their

corresponding counter-rotation counterparts at the same Ta ($a = 0.46, 0.44$), the axial average is performed in the region between the maximum values of u_r , in order to sample a roll couple. In contrast, averages for the cases at $a = -0.21, 0.49$, and 0.125 are done throughout the entire axial domain. The reason is that no coherent structures are detected for $a = 0.49, 0.125$, and for the case at $a = -0.21$, two symmetric rolls are contained within the full axial domain. In figure 4.6a, we show $\text{RMS}(\tilde{u}_r)$ as a function of the driving, where we observe that the $\text{RMS}(\tilde{u}_r)$ of the co-rotating peak decreases with driving while the opposite occurs for the counter-rotating peak. However, for the highest Ta we observe that the RMS of the radial velocity decreases for increasing driving.

In addition to the strength of the rolls, we look now at the so-called “wind” by looking at the radial velocity fluctuations defined by

$$\sigma_{\text{bulk}}(u_r) \equiv \langle \sigma_{t,\theta}(u_r) \rangle_{r_{\text{bulk}},z}, \quad (4.4.3)$$

where $\sigma_{t,\theta}(u_r)$ is the standard deviation of the radial velocity averaged in the azimuthal direction and over time. Here, the averages are performed in the same way as for $\text{RMS}(\tilde{u}_r)$. From this characteristic velocity we construct the wind Reynolds number, i.e. $\text{Re}_w = (d\sigma_{\text{bulk}}(u_r))/\nu$. In the classical regime of turbulence, the unifying theory of Grossmann and Lohse [52] predicts a scaling of the Reynolds wind $\text{Re}_w \propto \text{Ta}^{3/7}$. When the driving is increased, towards the ultimate regime, the logarithmic corrections remarkably cancel out and an effective scaling of $\text{Re}_w \propto \text{Ta}^{1/2}$ is observed [52, 57]. In figure 4.6b, we plot the compensated Reynolds wind with the scaling of the ultimate regime $\text{Re}_w \text{Ta}^{-1/2}$ as a function of Ta. Here we see that, indeed, beyond the transition to the ultimate regime, Re_w slowly asymptotes to a $\text{Ta}^{-1/2}$ scaling for both peaks, which is consistent with the observation of [57] for $\eta = 0.716$ at $a = 0$. We now draw the attention to the case of $\text{Ta} = 5.10 \times 10^8$, which is close to Ta_c , and where both angular momentum peaks have roughly the same magnitude (see figure 4.4b). As shown in figure 4.5, for corotation at $a = -0.21$ (second panel of first row in figure 4.5), a peculiar pattern of the radial velocity can be appreciated along the axial direction. If we compare this panel with the first and the third panel of the same row, we immediately note an anomalous pattern: the presence of a roll pair requires that at the interface their velocities point at the same direction. As a consequence, we expect a succession of positive and negative radial velocities as can be seen in the first and third panels. Rather peculiarly, in the second panel ($a = -0.21$), we encounter two consecutive regions of negative velocity, located in between $0.42 \leq z/L \leq 0.48$. As a consequence, we observe an unexpected pattern of two counterclockwise Taylor rolls coexisting next to each other, although slightly disconnected. This

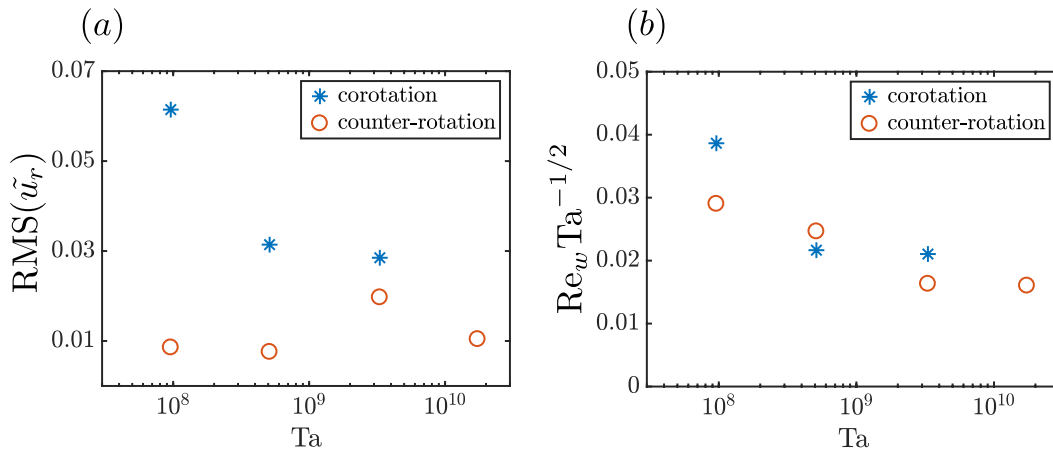


Figure 4.6: (a) RMS along the axial direction of the azimuthally-time-bulk averaged radial velocity, normalized with the shear velocity u_S , as a function of the driving strength Ta . (b) Wind Reynolds number (based on the radial velocity) as a function of Ta . In both figures, the blue stars represent states that correspond to the peak in the corotating regime, while the red open circles represent measurements for the peak for counter-rotation.

rather interesting observation will be revisited in section 4.5.3, as we unveil more data from the numerical simulations.

4.5 Boundary layer transitions and state switching

In the previous sections, we highlighted various observations which cannot be fully explained by the limited information we can retain from the experiments. In this section, we therefore turn to direct numerical simulations instead, such as to provide a more quantitative description of the observations. Namely, the mechanism responsible for the disappearance of the broad peak with sufficient shear (see figure 4.4a), the observation of discrete jumps in the corotating regime ($a < 0$) for $Ta = 2.23 \times 10^9$ and $Ta = 3.31 \times 10^9$ (see figure 4.3a) and the “peculiar” pattern of Taylor rolls which was presented in the previous section (see figure 4.5). We closely examine the velocities, especially in the boundary layers, and inspect the changes in roll states.

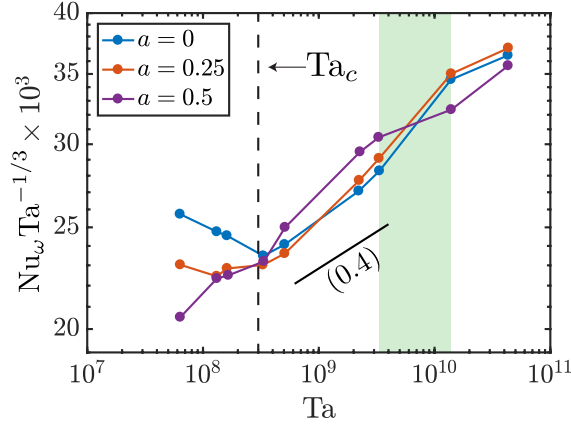


Figure 4.7: Compensated Nusselt number as a function of Ta for three rotation ratios. A reordering of the curves around $Ta \approx 10^{10}$ can be seen. The green shaded area corresponds to the region where a *jump* can be seen due to the disappearance of quiescent wind shearing regions. The black solid line represents the scaling of $Nu_w \propto Ta^{0.4}$.

4.5.1 Disappearance of the broad peak

We first focus on the shift of the counter-rotating peak that leads to the $Nu_w(a)$ measurement for $Ta \approx 10^{10}$ shown in figure 4.3a. In section 4.2.2, we mentioned how, for $a = 0$, jumps in the $Nu_w(Ta)$ relationship appeared at $Ta \approx 10^{10}$ (see figure 4.2). These coincided with the disappearance of the torque on the roll-wavelength, and cannot be associated to the transition to the ultimate regime, as it happened at a much higher value of Ta . In figure 4.7, we show the behaviour of the $Nu_w(Ta)$ curves for three selected values of a . We see how at $Ta \approx 10^{10}$, a reordering of the curves occurs, distinct from the one seen at $Ta = Ta_c$. For $a = 0$ and $a = 0.25$, a discrete jump in the relationship increases the torque, while for $a = 0.5$ the opposite process seems to occur.

By relating this to the transition observed in Ostilla-Mónico et al. [107], where the quiescent regions of the boundary layer disappeared, we can explain why the counter-rotating maximum shifts. In figure 4.8, we show the structure of the near-wall region for several values of R_Ω (and a). As R_Ω is increased (i.e. from counter-rotation towards pure inner cylinder rotation), the flow structure self-organizes: the near-wall turbulent streaks occur in a stratified manner and the turbulent Taylor-roll is stabilized. The appearance of quiescent regions is not inconsistent with the idea that the creation of the narrow peak is due to shear instabilities that arise from the BLs. Both before and after the transition

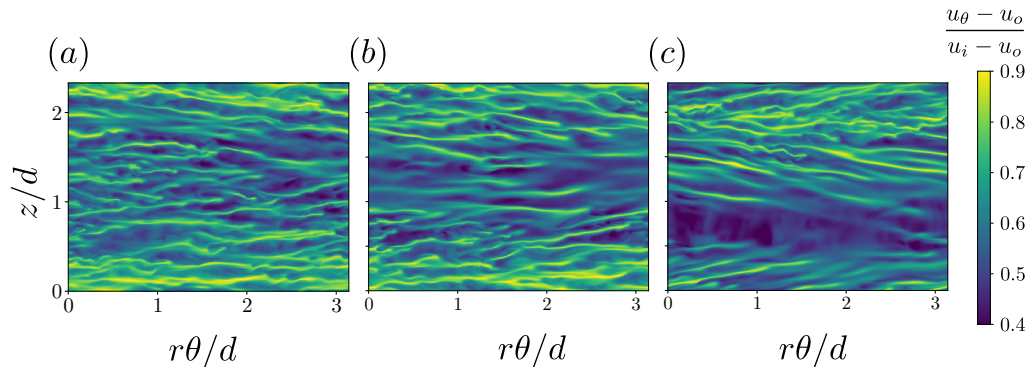


Figure 4.8: Instantaneous normalized azimuthal velocity at $r^+ = 15$ for $Ta = 5 \times 10^8$ for (a) $a = 0.6$ ($R_\Omega = 0.02$), (b) $a = 0.47$ ($R_\Omega = 0.03$), and (c) $a = 0$ ($R_\Omega = 0.09$). The DNS corresponds to the case of $\Gamma = 2.33$.

to the ultimate regime, only parts of the boundary layer are active in producing plumes or streaks. During the transition to the ultimate regime, the plume-emitting part of the laminar boundary layer transitions to turbulence, while the quiescent part remains quiescent. For larger Ta , beyond $Ta = 10^{10}$, the quiescent regions disappear, and the entire boundary layer becomes active and turbulent. As this happens, the $a = 0$ curve surpasses the $a = 0.5$ curve. Because there is no quiescent area to eliminate for $a > 0.5$, these branches of the $Nu_\omega(Ta)$ curve do not jump and remain at a lower value.

4.5.2 Roll state switches

We now focus on the discrete jumps in the $Nu_\omega(a)$ curve at $Ta = 2.23 \times 10^9$ and $Ta = 3.31 \times 10^9$ for $a < 0$ from the experiments (see figure 4.3). We note that in previous simulations, both by [16] and [106], a small Γ domain is used, which essentially fixes the roll size. The fact that no discrete jumps are detected in the numerics with small boxes, indicates that roll state switching might be responsible for this. Thus, in order to explain these jumps, we need to use both a small computational box which accommodates a single roll pair, as well as medium-sized boxes which can sustain changes in roll number. In this way, we can capture how the rolls manifest as the system goes from pure counter-rotation to corotation, and whether state switching takes place or not. We note that the number of rolls does not significantly affect the value of Nu_ω and that the only dependence comes from the roll wavelength [14, 111]. However, by enforcing a periodicity length, both effects

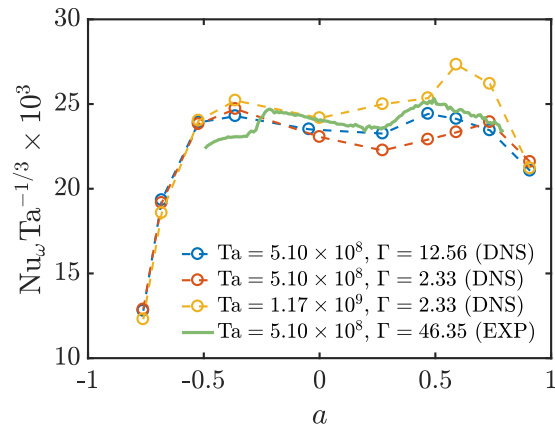


Figure 4.9: Compensated Nusselt number as a function of a obtained from the DNS of the current study. The green solid line is the experimental data performed at $\text{Ta} = 5.10 \times 10^8$.

will manifest simultaneously. The roll number N and the (non-dimensional) roll wavelength λ_z are related by $\lambda_z = \Gamma/N$.

In figure 4.9, we show the compensated Nusselt number for both the small and the medium boxes for two Ta , and the experiments for $\text{Ta} = 5.10 \times 10^8$. The numerical simulations at $\text{Ta} = 5.10 \times 10^8$ reveal that for $a < -0.5$ the value of Nu_ω is at most weakly dependent on Γ . However, for $a \geq -0.5$ the two numerical studies and the experimental measurements result in different values of Nu_ω . To further explore this, in figure 4.10 we show the azimuthally and temporally averaged radial velocity for the medium-sized domain ($\Gamma = 12.56$), as we vary a from the corotating to the counter-rotating regime. In terms of R_Ω this is equivalent to varying the Coriolis force from anti-cyclonic to zero. Here, we can see that the flow self-organizes in Taylor rolls as the Coriolis force starts to become dominant, i.e., when $R_\Omega \neq 0$ [132]. As R_Ω increases, we first observe that the rolls become sharper and more prominent, as evidenced by an increment in $|u_r|$, which is also observed in the experiments (see figure 4.5). As we approach the “broad peak”, the number of roll pairs switch, first from four to five, then from five to six, which sharply reduces the roll wavelength. This reduction in wavelength clearly has an effect on the torque as can be seen in figure 4.9 for $a > -0.5$. The change in the roll wavelength changes the proportion between quiescent and active regions inside the boundary layers [159, 160]. As Ta increases, these sharp changes in the $\text{Nu}_\omega(a)$ curve disappear, because roll state switching does not modify the fraction of boundary layer regions which emit plumes.

The influence of the large structures on the torque can also be appreciated

4.5 Boundary layer transitions and state switching

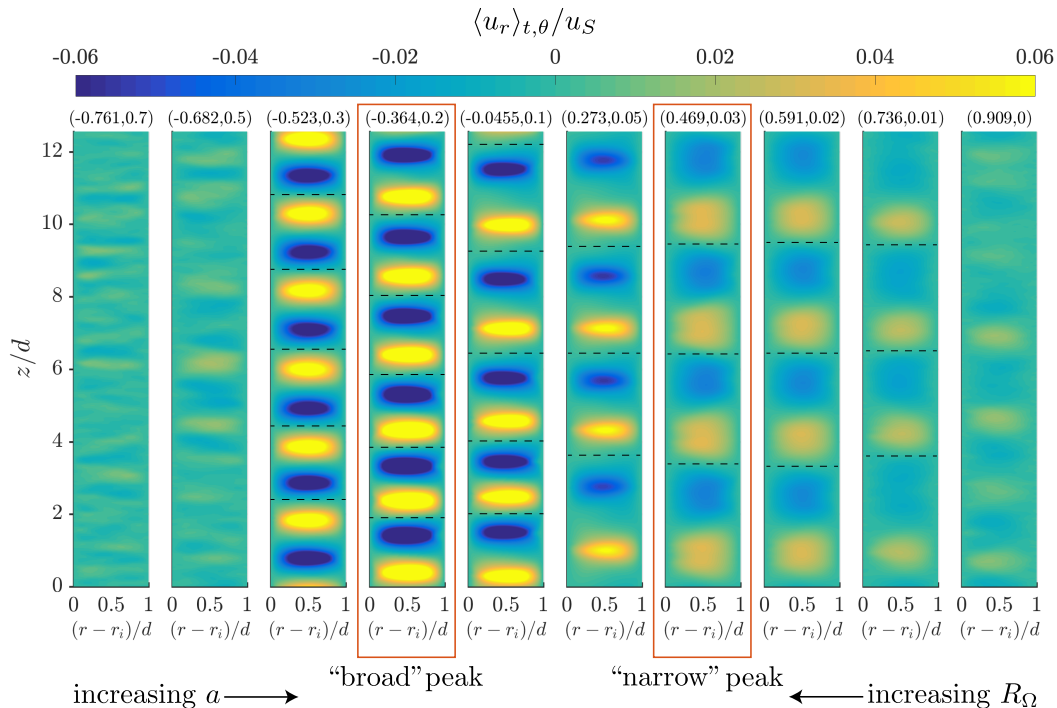


Figure 4.10: Azimuthally-time averaged radial velocity normalized with the shear velocity u_S obtained from DNS for $Ta = 5.10 \times 10^8$ and $\Gamma = 12.56$. Each plot represents a different rotation state, quantified by either a or R_Ω . The legend on top of each figure represents the value of (a, R_Ω) . The flow state that corresponds to either the “broad” or “narrow” peak are highlighted in red. The arrows indicate the direction of the increment of either a or R_Ω .

when we compare the $\Gamma = 12.56$ simulation with the experimental data ($\Gamma = 46.35$) shown in figure 4.9. Here, we see that both the experimental and numerical data coincide within the region $0.3 < a < 1$, where the Coriolis force is small and the rolls only start to become organized. However, in the region between $-0.5 < a < 0.3$ there are significant discrepancies between experiments and numerics. These are probably a consequence of state switching. In the medium size box ($\Gamma = 12.56$), a switch in the number of roll pairs can take place, but the values that the roll wavelength can take are more restricted due to the size domain and thus, leading to large variation in roll wavelength across different states. In the experiment Γ is much larger, so state switches will generally have a very small effect on the roll wavelength, and as a consequence a small effect on the torque. This can explain both the jumps in the $Nu_\omega(a)$ curve, and why they are much smaller than for numerics.

4.5.3 Transient roll dynamics

During the transition to the ultimate regime, the homogeneous distribution of the roll breaks down (see figure 4.10). They acquire different sizes and different shapes: the distance between the maximum absolute value of u_r , and hence, the size of the rolls is not always the same. In order to explain the pattern depicted at the end of section 4.4.3, represented in the second panel of figure 4.5, i.e., the presence of two adjacent counterclockwise Taylor rolls, we must explore the instantaneous velocity fields that DNS provides. Experimental results examine consecutive meridional planes ($r - \theta$) and assume that the flow is azimuthally homogeneous. However, if the structures change only locally, this could be wiped out by an averaging operation.

As R_Ω increases (see figure 4.10), the rolls become sharper, until at a certain point, one of them can start to split up locally, such that transiently, outflow, or inflow regions with the same sign coexist next to each other at certain values of the azimuth. As R_Ω is further increased, the roll splits up completely to form a new roll pair. However, the speed at which this roll “dislocation” exists and propagates to “fracture” the roll is a priori unknown.

In order to closely inspect the change in the morphology of the rolls as a function of the Coriolis force, we perform DNS by slowly changing the value of R_Ω over a certain number of large eddy turnover times $\tau = tU/d$, where U is the characteristic velocity as defined in section 4.3. The simulations are performed for $Ta = 5.10 \times 10^8$ and for the medium-sized box ($\Gamma = 12.56$). The idea is to capture the evolution of the radial velocity and its effect on Nu_ω as we slowly increase R_Ω in discrete steps. We initiate the simulation at $\tau = 0$ with a statistical stationary TC flow and $R_\Omega = 0$. Next, at $\tau = 25$, we increase the value of the Coriolis force to $R_\Omega = 0.02$. When $\tau = 50$ is reached, we set finally R_Ω to 0.03. In figure 4.11a, we show the instantaneous Nu_ω and in figure 4.11b, we show the space-time evolution of the instantaneous radial velocity u_r at mid-gap. We note that, globally, a correlation between transient regions of Nu_ω and the change in R_Ω can be observed. This is caused by the increasing acceleration of the flow, in which the number of rolls changes as well. Locally, we clearly see two instants in which two consecutive rolls begin to approach each other until they merge. Right before the merging, we observe a long-time transient, of $\approx 10\tau$, in which two consecutive outflow regions can coexist next to each other. This indicates—just as it was observed in the experiments shown in figure 4.5—that close to the transition to the ultimate regime, a change in the roll dynamics can occasionally lead to long-time transient effects.

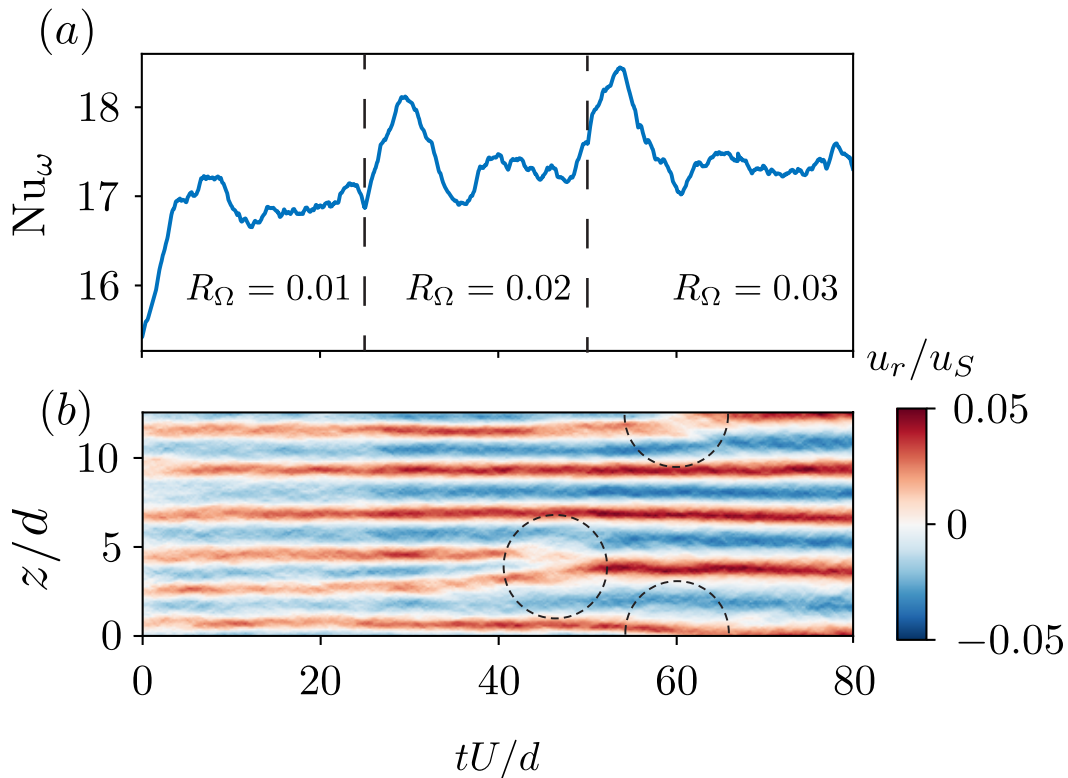


Figure 4.11: DNS results of varying R_Ω for $Ta = 5.10 \times 10^8$ and $\Gamma = 12.56$. (a) Temporal evolution of the dissipation Nu_ω . (b) Time-space diagram of the instantaneous u_r at mid-gap. Here, two regions of merging rolls can clearly be seen, which are generated from two consecutive outflow regions. These mergers are highlighted with the dashed circles. The vertical dashed lines in (a) represent a stage during the simulation for a fixed value of R_Ω .

4.6 Summary and conclusions

We probe the angular momentum transport with both experiments and direct numerical simulations for $\eta = 0.91$ as a function of the driving which we quantify with Ta and the magnitude of the Coriolis force which we quantify with either the rotation ratio a or the rotation number R_Ω . The range of shear driving we explore spans several decades of Ta , namely $\mathcal{O}(10^7) - \mathcal{O}(10^{10})$, which includes the transition to the ultimate regime at $Ta \approx Ta_c = 3 \times 10^8$. In the vicinity of Ta_c , our experiments reveal the presence of two local angular momentum transport maxima for fixed Ta , as it was firstly reported by the numerical works of Brauckmann et al. [17] and Brauckmann and Eckhardt [16]. Thus we have demonstrated that this occurrence is not an artifact of the axial domain used in the numerics. We showed that the broad peak is associated to

the strengthening of the large-scale structures (Taylor-rolls) due to an increment in centrifugal forcing R_Ω , as it is evidenced by both PIV and DNS. In addition, the numerical simulations reveal that the appearance of the narrow peak is a consequence of shear instabilities that arise from the BLs. Moreover, we show that as the driving increases, the broad peak remains roughly at the same R_Ω while decreasing its magnitude. Conversely, the narrow peak increases its magnitude while experiencing a shift in R_Ω . We attribute this to the different way in which the near-wall structures self-organizes at $Ta \approx 10^{10}$. Explicitly, the disappearance of quiescent wind sheared regions at the cylinder walls, which suddenly transition to a state where the whole BLs can emit plumes, as evidenced by a sharp “jump” in the $Nu_\omega(Ta)$ curve. With sufficient driving, both the experiments and numerics confirm that the shear instabilities dominate over centrifugal instabilities and the broad peak disappears at around $Ta = 4.95 \times 10^9$. Beyond this value, only the narrow peak can be detected.

In the experiments, a peculiar state of the Taylor rolls is observed at $a = -0.210$ ($R_\Omega = 0.141$) and $Ta = 5.10 \times 10^8$, which is close to Ta_c , where both the narrow and broad peaks are present and have roughly the same magnitude. Here, we observe two neighboring Taylor rolls which rotate opposite to each other. We explore the possibility that this *unusual* state is produced by roll splitting, which occurs when the axial extent is sufficiently large and for sufficient R_Ω . The numerics at $Ta = 5.10 \times 10^8$ reveal that as the magnitude of the Coriolis force increases via R_Ω , the Taylor rolls undergo a reorganization and a change in both their number and wavelength. This effect translates into a change in the global torque, i.e. Nu_ω , which is evidenced by different $Nu_\omega(a)$ curves for different values of Γ . We explore the reorganization of the rolls in detail by performing a last numerical simulation where we slowly vary R_Ω several times. Here, we observe that for the same driving Ta and curvature η as in the experiments (different Γ), the merging of two adjacent rolls is possible. This suggests that the “peculiar” pattern of roll formation discussed previously can be a consequence of such long-time transient effects. Further work in this direction is encouraged in order to thoroughly explore this new feature of secondary flows in TC flow.

Chapter 5

Dynamic mode decomposition analysis of coherent structures rotating plane Couette flow

Based on: Francesco Sacco, Rodolfo Ostilla-Mónico & Roberto Verzicco, 'Dynamic mode decomposition analysis of coherent structures rotating plane Couette flow', to appear on *Journal of Physics: Conference Series*.

5.1 Introduction

Turbulent flows are generally characterized by chaotic motion and abundant mixing. But within certain canonical systems, experiments and simulations have detected coherent large scale structures [66, 10]. The prime example of a turbulent system where such coherent flows are present is plane Couette (PC) flow, the shear-driven flow between two parallel plates. Direct numerical simulations (DNS) of PC flow have found extremely long structures that are far larger than the inter-plate distance [156, 8, 118, 79]. To accurately capture these structures, we require computational boxes that are large enough to fit them. Large-scale structures have some important practical impact, having the general role of redistributing friction and heat flux along the walls and across the flow [10]. Small computational boxes that fail to capture these large-scale structures can considerably alter the flow behaviour and statistics [156].

In the last decades, improvements in computation have made possible the use of numerical simulations as a tool for observing and exploring phenomena in many different systems. In this context, substantial effort has been made to characterize the origin, pinning and mathematical modelling of the coherent structures in turbulent flows. Methods for isolating these structures are still under development. Commonly used methods to extract structures include moving ensemble averages [8, 85], two-point correlations [138] or Fourier analysis [112]. The main disadvantage of these methods is that they often include the relatively arbitrary choice of a cut-off to isolate the structures, be it in the shape of a cut-off frequency in Fourier space [112], or in the shape of a threshold value for a certain attribute [8, 138]. Furthermore, these methods are usually tuned for one particular setup of the system; but as the control parameters of the flow changes, so do the shape of the coherent structure. Because of this, conventional methods can completely fail to track structures across certain dimensions of parameter space.

Our main aim is the development of a low-order model for the analysis of the evolution of large-scale structures in PC flow across parameter space. But to do this, we must be able to robustly capture the structures everywhere in parameter space, and separate them from the background turbulence. This filter must remove arbitrariness as far as possible. In this manuscript, we will assess the merits of Dynamic Mode Decomposition [135] (DMD) in fulfilling this tasks. The DMD method is fully detailed below, but for now we highlight that this method is a data-driven technique that algorithmically is a regression of data onto locally linear dynamics. This makes it a promising candidate to extract the large-scale structures in wall-bounded turbulent flow, as it is known

that these structures behave in a quasi-inviscid, quasi-linear manner [60].

We will focus on rotating plane Couette (RPC) system, i.e. PC flow with an added solid-body rotation in the spanwise direction. A spanwise rotation coincides with the direction of the underlying streamwise vorticity, and it is known to significantly alter the shape and dynamics of the large-scale structures. Anti-cyclonic rotation induces a strong secondary flow perpendicular to the main flow direction, and pins the structures in the spanwise direction [132]. By comparing how DMD perform for both PC flow with no rotation and RPC flow with anti-cyclonic rotation, we can assess the merits of DMD in capturing our quantities of interest.

This article is organized as follows. In section 5.2 we briefly recall the general idea of the standard DMD method and of the variants we have used for our analysis. In section 5.3 we introduce the numerical details of the simulations. In section 5.4 we report the analysis of the method applied on both PC and RPC, with a particular care on the obtained large scale structures. The final section 5.5 contains a summary of the work done and the conclusions.

5.2 Dynamic mode decomposition

Dynamic mode decomposition (DMD) is a method that provides a spatio-temporal decomposition of data into a set of relevant dynamical modes from a sequence of snapshots of an evolving system. The method was firstly developed by Schmidt [135] to provide a linear approximation of non-linear dynamics, and soon after it was closely linked to Koopman operator analysis [130, 71, 72]. The Koopman operator is an infinite dimensional linear operator that represents the non-linear dynamic of a physical system. Because the underlying system is non-linear, and the Koopman operator does not linearize the system, the operator becomes infinite-dimensional. The DMD method can be interpreted as a way of calculating a finite approximation of the Koopman operator.

5.2.1 Standard DMD

In what follows, we briefly outline the key steps of DMD. The method is applied to spatio-temporal data organized in N -equispaced, M -dimensional realizations of the system:

$$x_i \equiv x(t_i) \in \mathbb{R}^M \quad \text{where} \quad t_i = t_1 + (i-1)\Delta t \quad \text{for} \quad i = 1, \dots, N.$$

The data are arranged in an $M \times N$ matrix:

$$X = [x_1, \dots, x_N].$$

The DMD method relies on the following Koopman assumption:

$$x_{i+1} = Ax_i \quad \text{for} \quad i = 1, \dots, N-1, \quad (5.2.1)$$

which can be written in matrix form as:

$$X_2^N = AX_1^{N-1}, \quad (5.2.2)$$

where the *snapshot matrices* are generally defined as:

$$X_j^k = [x_j, x_{j+1}, \dots, x_k].$$

In practice, when the dimension M is large, the matrix A may be intractable to analyze directly. DMD circumvents the eigendecomposition of A by considering the projection on its proper orthogonal decomposition (POD) modes, resulting in a rank-reduced matrix \tilde{A} .

The DMD algorithm proceeds as follows [157]:

- 1) Compute the truncated singular value decomposition (SVD) of the snapshot matrix X_1^{N-1} :

$$X_1^{N-1} = U\Sigma V^H \quad (5.2.3)$$

where \cdot^H denotes the conjugate transpose of a matrix, $\Sigma \in \mathbb{C}^{K \times K}$ is the diagonal matrix containing the retained SVD singular values sorted in decreasing order, and the (orthonormal) columns of the matrix $U \in \mathbb{C}^{M \times K}$ and the matrix $V \in \mathbb{C}^{N-1 \times K}$ are the spatial and temporal SVD-modes, respectively. We remark also that the left singular vectors of U correspond to POD modes.

- 2) Compute \tilde{A} , the projection of the full matrix A onto U :

$$\tilde{A} = U^H A U = U^H Y V \Sigma^{-1} \quad (5.2.4)$$

- 3) Compute the eigenvalues λ_k and eigenvectors w_k of \tilde{A} , arranged in the matrices Λ and W :

$$\tilde{A}W = W\Lambda \quad (5.2.5)$$

4) Reconstruct the eigendecomposition of A from W and Λ :

$$A\Phi = \Phi\Lambda, \quad \Phi = X_2^N V \Sigma^{-1} W \quad (5.2.6)$$

Note that the eigenvalues for A are equivalent to those of \tilde{A} , and that the eigenvectors of A are given by the columns of Φ , and correspond to the DMD modes.

In this way, with the columns of the A and Φ matrices, we arrive at the DMD representation of the snapshots:

$$x_{DMD}(t) = \sum_{k=1}^K a_k \phi_k e^{(\delta_k + i\omega_k)t} \quad (5.2.7)$$

where, for convenience, we have written the eigenvalues as:

$$\delta_k + i\omega_k = \frac{\log(\lambda_k)}{\Delta t}, \quad (5.2.8)$$

in order to distinguish in (5.2.7) the growth rates δ_k , and frequencies ω_k of the Fourier-like modes. The amplitudes a_k are computed via least squares fitting (as in optimized DMD [26]) of the snapshots in expansion (5.2.7).

Standard DMD has several known limitations. The DMD method is based on an underlying SVD, whose well known weaknesses are the inability to efficiently handle invariances in the data, such as translational and/or rotational invariances of low-rank objects; and as other SVD-based methods, DMD is also unable to handle transient time phenomena (cf. chapter 1.5 in [72], or [153] for examples). To address these problems, several modifications to the basic DMD method have been proposed. For this manuscript we will consider two of these methods.

5.2.2 Multi-resolution DMD (mrDMD)

The first method we will use is multi-resolution DMD (mrDMD). The method mrDMD is derived by the idea of separating slow and fast modes with techniques from foreground/background subtraction in video feeds [51]. It essentially combines features of the DMD decomposition with key concepts from wavelet theory and multi-resolution analysis [71, 73].

As we can see from (5.2.8), the characteristic time of a mode is inversely proportional to $|\log(\lambda_k)|$. It depends on the magnitude of both frequency and growth/decay rate. A mode can be considered “slow” if $|\delta_k + i\omega_k| \approx 0$. This simply means that the mode changes somewhat slowly as the system evolves

in time. To have an immediate representation of this behavior, when we plot a mode in a $Re(|\log(\lambda_k)|)-Im(|\log(\lambda_k)|)$ space, a DMD mode with temporal frequencies near the origin in this space has both small ω_k and δ_k and therefore represents a slow mode. Such modes are interpreted as background (low-rank) portions of the given dynamics, while the terms with temporal frequencies far from the origin are their foreground (sparse) counterparts.

The mrDMD recursively removes low-frequency slowly-varying content from a given collection of snapshots. In this way at each step the slow-modes are removed first and the data is filtered for analysis of its higher frequency content. This recursive sampling structure is demonstrated to be effective in allowing for a reconstruction of a greater number of datasets with respect to classical DMD, since it overcomes the transitional and transient problems described above [51, 72, 154].

The mrDMD method is an iterative algorithm that can be briefly summarized as follow:

- 1) Compute DMD for available data.
- 2) Determine fast and slow modes.
- 3) Find the best DMD approximation to the available data constructed from the slow modes only.
- 4) Subtract off the slow-mode approximation from the available data.
- 5) Split the available data in half.
- 6) Repeat the procedure for the first half of data (including this step).
- 7) Repeat the procedure for the second half of data (including this step).

Mathematically, the mrDMD separates the DMD approximate solution (5.2.7) in the first pass as:

$$x_{mrDMD}(t) = \sum_{k=1}^K a_k \phi_k^{(1)} e^{(\delta_k + i\omega_k)t} = \underbrace{\sum_{k=1}^{m_1} a_k \phi_k^{(1)} e^{(\delta_k + i\omega_k)t}}_{\text{slow modes}} + \underbrace{\sum_{k=m_1+1}^K a_k \phi_k^{(1)} e^{(\delta_k + i\omega_k)t}}_{\text{fast modes}}, \quad (5.2.9)$$

where we have ordered the modes from the slowest to the fastest. Note that the modes computed at this level are indicated with $\phi_k^{(1)}$, and that we are separating the first m_1 background slowest modes from the other ones. Since

we have already removed the slowest modes in the first sum, in the second step we use the second sum to yield the fast scale data matrix:

$$X_{K/2} = \sum_{k=m_1+1}^K a_k \phi_k^{(1)} e^{(\delta_k + i\omega_k)t}. \quad (5.2.10)$$

The matrix $X_{K/2}$ is now separated into two matrices:

$$X_{K/2} = X_{K/2}^{(1)} + X_{K/2}^{(2)}, \quad (5.2.11)$$

where each of the two matrices contain $K/2$ of the total K snapshots. We then recompute DMD separately on both of the two matrices but we retain the slowest m_2 DMD modes, indicated as $\phi_k^{(2)}$, obtained from both the decomposition at this level.

The iterative process works by recursively removing slow frequency components until a desired multi-resolution decomposition has been achieved. The final DMD approximation reads as:

$$x_{mrDMD}(t) = \sum_{k=1}^{m_1} a_k^{(1)} \phi_k^{(1)} e^{(\delta_k^{(1)} + i\omega_k^{(1)})t} + \sum_{k=1}^{m_2} a_k^{(2)} \phi_k^{(2)} e^{(\delta_k^{(2)} + i\omega_k^{(2)})t} + \sum_{k=1}^{m_3} a_k^{(3)} \phi_k^{(3)} e^{(\delta_k^{(3)} + i\omega_k^{(3)})t} + \dots \quad (5.2.12)$$

To be precise, $\phi_k^{(i)}$ are the DMD modes obtained at i -th level of decomposition, and the m_k are the number of slow modes retained at each level. In this way each successive level contains modes that are faster and faster, thereby providing a way to identify long-, medium-, and short-term trends in data. There is not a single set of modes that dominates the SVD and potentially obscures features at other time scales, but instead different DMD modes are used to represent key features at different time scales. We refer the reader to [73] for more detailed information on the method and its applications.

5.2.3 High order DMD

High order DMD (HODMD) is an extension of the classic DMD method which is appropriate to treat general periodic and quasi-periodic dynamics, and transients decaying to periodic and quasi-periodic attractors. This includes cases, not accessible to standard DMD, that show limited spatial complexity but a very large number of involved frequencies.

Instead of using the Koopman assumption (5.2.1), HODMD relies on the *higher order* Koopman assumption:

$$x_{i+d} = A_1 x_i + A_2 x_{i+1} + \dots + A_d x_{i+d-1} \quad \text{for } i = 1, \dots, N - d, \quad (5.2.13)$$

for a tunable $d \geq 1$. Equation (5.2.13) can also be written as:

$$\hat{x}_{k+1} = \hat{A}\hat{x}_k, \quad (5.2.14)$$

where \hat{x}_k and \hat{A} are defined as:

$$\hat{x}_k = \begin{pmatrix} x_k \\ x_{k+1} \\ \dots \\ x_{k+d-1} \end{pmatrix}, \quad \hat{A} = \begin{pmatrix} 0 & I & 0 & \dots & 0 & 0 \\ 0 & 0 & I & \dots & 0 & 0 \\ \dots & \dots & \dots & \dots & \dots & \dots \\ 0 & 0 & 0 & \dots & I & 0 \\ A_1 & A_2 & A_3 & \dots & A_{d-1} & A_d \end{pmatrix}. \quad (5.2.15)$$

After applying a first dimension reduction on the general snapshot matrix X_1^N , the HODMD algorithm proceeds the same way as the standard DMD described in section 5.2.1, and is applied on the reduced snapshots reorganized as in equation (5.2.14) (see [77] for more details).

Note that the main difference between equations (5.2.1) and (5.2.13) is that the latter relates each snapshot with not only the last but also the preceding $d - 1$ snapshots. In fact, HODMD reduces to standard DMD if $d = 1$. For $d > 1$, instead, HODMD can be seen as a result of applying standard DMD to a set of enlarged snapshots (*time-lagged snapshots*) which also contains the delayed snapshots (*sliding window*).

The idea of using delayed snapshots to characterize chaotic dynamics comes from the time-delay embedding theory, and in particular from the *delayed embedding theorem* by Takens [148], who followed and formalized former seminal ideas by Packard *et al.* [114]. This theory states that in some cases, it may be possible to reconstruct the entire attractor of a turbulent flow from a time series of a single point measurement, by enriching a single observable $x(t)$ with time-shifted copies of itself, known as *delay coordinates* or *delay reconstruction*, $\mathbf{x}(t) = \{x(t), x(t - \tau), \dots, x(t - (d - 2)\tau), x(t - (d - 1)\tau)\}$, where τ is the *lag* or *delay time*, and d is the *embedding dimension*. Takens' theory has been related not only to fluid attractors, but in general to nonlinear dynamics and data-driven methods [157, 18], as it can demarcate large coherent regions of phase space where the dynamics are approximately linear from those that are strongly nonlinear.

We note that in HODMD method two tunable tolerances ϵ_1 and ϵ_2 are defined; the first is linked to the first SVD truncation on X_1^N :

$$EE(M) = \frac{\sigma_{K+1}^2 + \dots + \sigma_R^2}{\sigma_1^2 + \dots + \sigma_R^2} \leq \epsilon_1, \quad (5.2.16)$$

with $R = \min\{N, M\}$ the rank of the full snapshot matrix. The second tolerance is selected to get rid of small amplitudes, i.e. a smaller number of L modes is retained such that

$$\frac{a_{L+1}}{a_1} < \epsilon_2. \quad (5.2.17)$$

The possibility of tuning the parameters d , ϵ_1 and ϵ_2 makes the method more robust than standard DMD methods, since in this way it can get rid of noise or discretization/truncation errors and hence avoids capturing unphysical modes [77, 78].

5.3 Numerical setup

The flow data used for the analysis will be taken from direct numerical simulations (DNS) of rotating plane Couette flow (RPCF) in a three dimensional domain bounded by no-slip conditions at the walls in the wall normal (y) direction at $y = 0$ and $y = 2h$, and periodic in the streamwise (x) and spanwise (z) directions with periodicity lengths L_x and L_z , respectively.

We have used an energy-conserving second-order centered finite-difference code for the spatial discretization, while the discretized system is integrated using a fractional-step method and advanced in time by a low-storage third order Runge-Kutta scheme. The simulation code used is based on the highly parallel FORTRAN-based AFiD (www.afid.eu) which has been used mainly for simulations of turbulent Rayleigh-Bénard convection and Taylor-Couette flow [163]. This code has been comprehensively validated. Detailed information regarding the code algorithms can be found in [163, 172].

All the simulations are performed in a reference frame such that the walls have opposite streamwise velocities $\pm U/2$, and the entire system rotates with angular velocity $\boldsymbol{\Omega} = \Omega_{rf} \mathbf{e}_z$ around the spanwise axis. In this frame the two control parameters are a shear Reynolds number $Re_s = Uh/\nu$ and a Coriolis parameter $R_\Omega = 2h\Omega_{rf}/U$.

The incompressible Navier-Stokes equations then become:

$$\nabla \cdot \mathbf{u} = 0, \quad (5.3.1)$$

$$\frac{\partial \mathbf{u}}{\partial t} + \mathbf{u} \cdot \nabla \mathbf{u} + R_\Omega \mathbf{e}_z \times \mathbf{u} = -\nabla p + Re_s^{-1} \nabla^2 \mathbf{u}. \quad (5.3.2)$$

A uniform grid is used in the streamwise and spanwise directions, while a Chebychev-type clustering near the walls is used in the wall-normal direction.

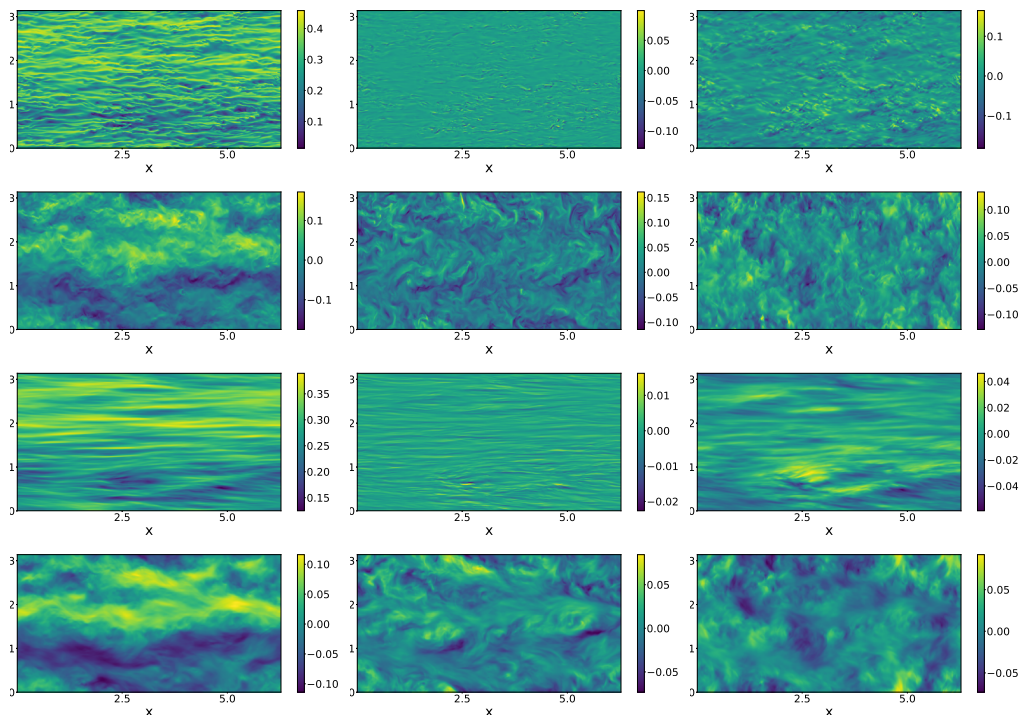


Figure 5.1: From top to bottom: instantaneous flow near the wall at $y^+ \approx 15$, instantaneous flow at the centerline $y = h$, mean flow near the wall at $y^+ \approx 15$, mean flow at the centerline $y = h$. From left to right, the panel represent the v_x (streamwise), v_y (wall-normal) and v_z (spanwise) velocity components, in the rotationless case $R_\Omega = 0$.

For this study we have fixed $Re_s = 3 \times 10^4$ and varied the Coriolis forcing, $R_\Omega = 0$ and 0.1 . The computational box used is of $4\pi h \times 2h \times 2\pi h$ in streamwise, wall-normal and spanwise directions respectively, the same size as in [133]. This has led to a numerical resolution of $n_x \times n_y \times n_z = 512 \times 384 \times 512$ in the wall-normal, streamwise and spanwise directions, respectively. In order to achieve temporal convergence, the simulations are run until the difference between the time-averaged shear at both walls is less than 1%.

To perform the DMD analysis, we have used open source algorithms. For mrDMD we have used the python package described in [36]; while for HODMD we have used the MATLAB solver described in [77], that can be found in [76].

5.4 Results

Before introducing the results obtained with DMD methods, we report here a visualization of the velocity flow fields of $2D$ slices in the $x - z$ plane taken

5.4 Results

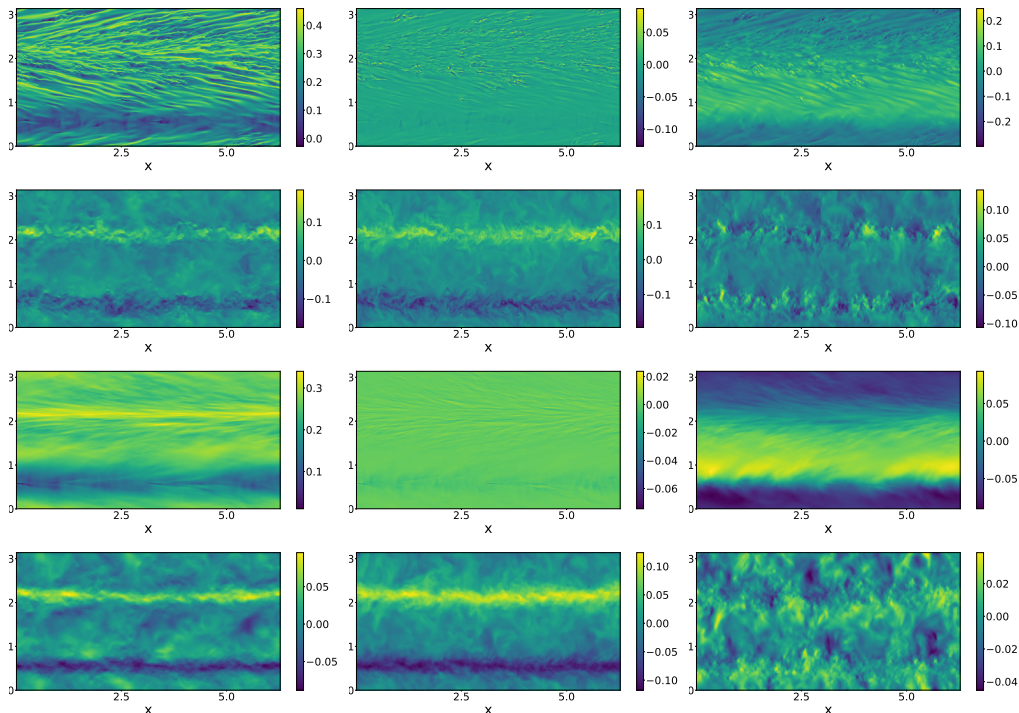


Figure 5.2: From top to bottom: instantaneous flow near the wall at $y^+ \approx 15$, instantaneous flow at the centerline $y = h$, mean flow near the wall at $y^+ \approx 15$, mean flow at the centerline $y = h$. From left to right, the panel represent the v_x (streamwise), v_y (wall-normal) and v_z (spanwise) velocity components, in the case with anti-cyclonic rotation $R_\Omega = 0.1$.

at fixed wall-normal distance: at the centerline $y = h$ and close to the wall at $y^+ \approx 15$. We have reported both the instantaneous and the temporal average of the flow, for both the rotationless case $R_\Omega = 0$ (figure 5.1) and the anti-cyclonic case $R_\Omega = 0.1$ (figure 5.2). We can see the complexity of the flow, composed by fast-evolving small structures, especially close to the wall, and large structures, whose shape is not perfectly defined in the $R_\Omega = 0$ case, and are approximately streamwise invariant, and pinned in the $R_\Omega = 0.1$ case.

5.4.1 mrDMD

We first applied the mrDMD method to a collection of 1000 snapshots of $2D$ slices in the $x - z$ plane taken at fixed wall-normal distance: at the centerline $y = h$ and close to the wall at $y^+ \approx 15$. The temporal spacing between each snapshot was fixed as $\Delta t U/h = 4 \times 10^{-2}$.

In what follows we analyze the components in the DMD decomposition (equa-

tion (5.2.12)), and the effect of the Coriolis force term R_Ω on this decomposition. We will particularly focus on the slowest modes, which should capture the dynamics of the large, coherent structures. As an additional test, we perform the analysis on a snapshot matrix built by considering the three velocity components simultaneously or separately, in order to capture the dominant modes of either the entire flow or of a single component.

No rotation

We first analyze the results obtained in the case with no rotation, $R_\Omega = 0$. We begin by reporting in figure 5.3 the stability of the modes. This is done through the eigenvalues as written in equation (5.2.8), in order to check both growth/decay rate and frequency of the modes. In particular we have highlighted the first level of the decomposition. As we have explained in subsection 5.2.2, mrDMD method recursively separates slow modes from fast modes; thus the first level of this decomposition is the first step in the recursive procedure, and corresponds to modes with both the lowest frequency and growth/decay rate. Moreover this level corresponds to the first summation addend of the decomposition written as in equation (5.2.12). If we look then at the first level of the decomposition performed on the single velocity components in figure 5.3 we can see that non-oscillatory modes –with zero imaginary component, are only present when analyzing the streamwise velocity. We also note that at the centerline the non-oscillatory mode is slightly decaying, while close to the wall, this mode is perfectly stable.

When we perform the analysis on the velocity fields simultaneously, we observe that the first level of the decomposition at the centerline has an imaginary component, probably meaning that the non-oscillatory, streamwise velocity is not strong enough to dominate the whole flow. We will return to this later.

To better understand the flow decomposition, we look at the mode amplitudes α_i , reported in figure 5.4. Here we can clearly see that for the streamwise velocity, the first (slowest) mode has a large influence in the dynamics of the flow both close to the wall and in the centerline, as its amplitude is significantly larger than that of other modes. This does not happen for the other two velocity components, where fast and slow modes contribute with similar weight to the dynamics. When we perform the method on the velocity fields simultaneously, we can again see that the first (slowest) mode has a large influence in the dynamics of the flow both close to the wall and in the centerline.

Both these results hint at the fact that mrDMD is only capturing a large-scale

5.4 Results

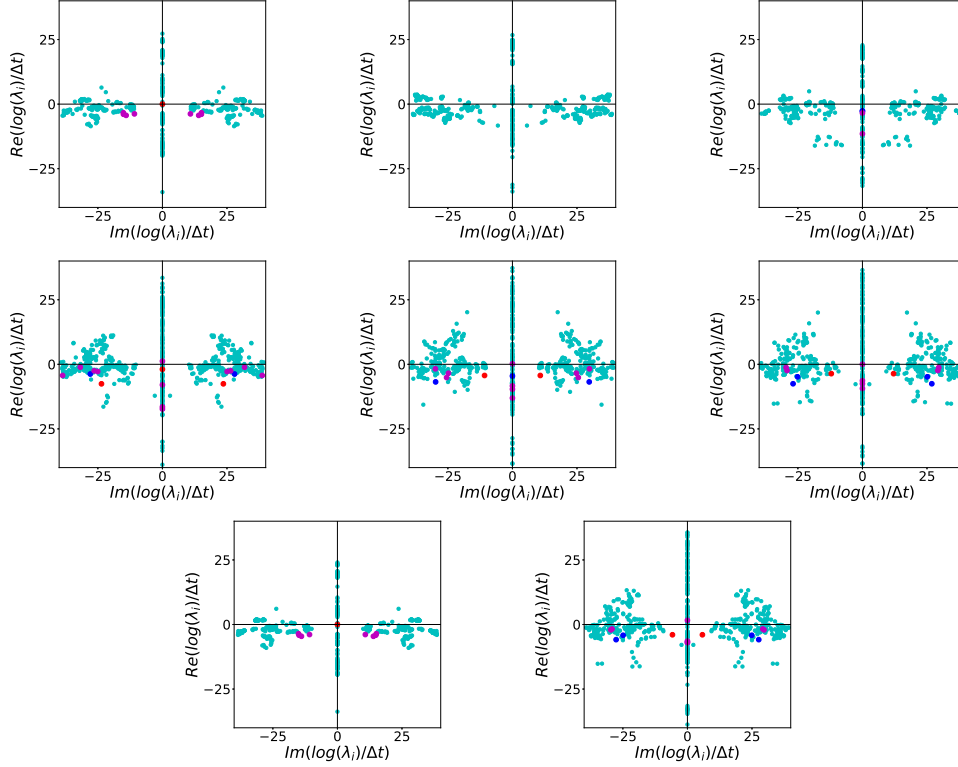


Figure 5.3: Growth/decay and frequency of the modes $\delta_k + i\omega_k = \frac{|\log(\lambda_k)|}{\Delta t}$ in the rotationless case $R_\Omega = 0$, near the wall at $y^+ \approx 15$ (top row) and at the centerline $y = h$ (central row). The panels correspond to the modes derived, from left to right, from the v_x (streamwise), v_y (wall-normal) and v_z (spanwise) velocity component singularly. The last row corresponds to the the modes derived from all the velocities simultaneously, close to the wall (left) and at the centerline (right). In the panels the first three levels of iteration of equation (5.2.12) are highlighted with red (level 1), blue (level 2) and magenta (level 3) markers.

mode in the streamwise velocity. Indeed, these behaviours are reflected when visualizing the modes themselves. In figure 5.5, we show the first (slowest) mode obtained with the mrDMD method applied to the three velocity components simultaneously. We observe the clear presence of a large-scale structure only for the streamwise velocity. In particular we have an evident large scale motion at the centerline, and close to the wall there is a structure pattern that is clearly related to the mid-gap one. Meanwhile, for the other velocity components, large-scale structures are completely absent.

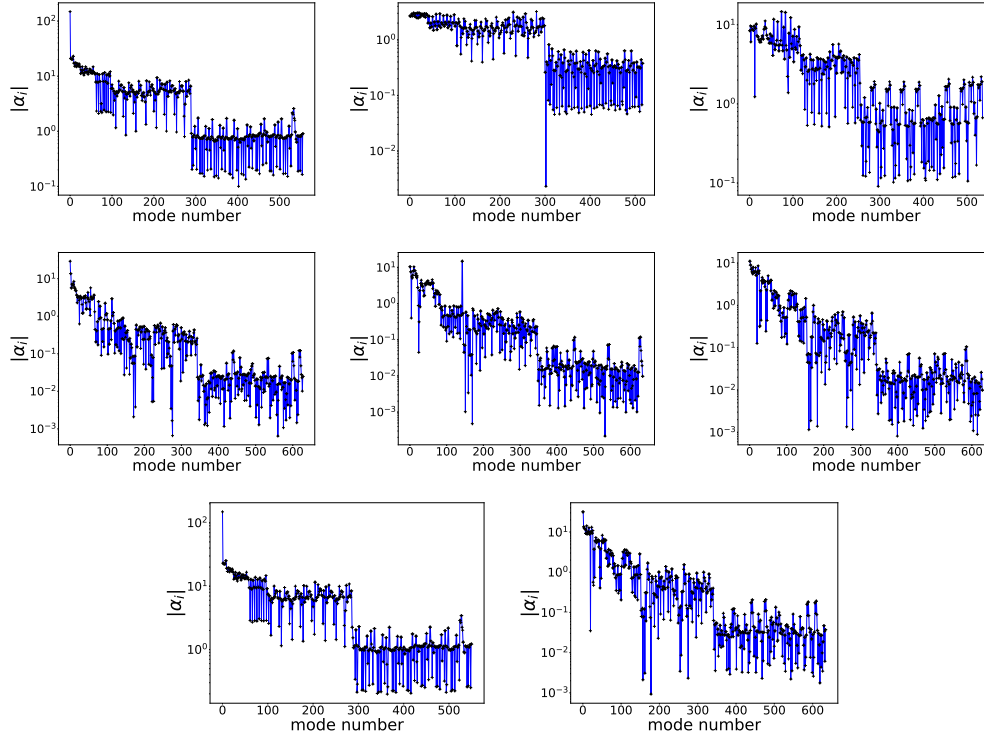


Figure 5.4: Amplitude α_i of the modes in the rotationless case $R_\Omega = 0$, near the wall at $y^+ \approx 15$ (top) and at the centerline $y = h$ (center). The panels correspond to the mode derived, from left to right, from the v_x (streamwise), v_y (wall-normal) and v_z (spanwise) velocity components singularly. The last row corresponds to the the modes derived from all the velocities simultaneously, close to the wall (left) and at the centerline (right).

Anti-cyclonic rotation

The situation is different when we inspect the results obtained in the case where anti-cyclonic rotation, $R_\Omega = 0.1$, is imposed to the flow. Again we start by analyzing the stability of the slowest modes in figure 5.3, written as in equation (5.2.8). We have then analyzed the first level of the decomposition, that is, as we have stated in the previous subsection, the first summation addends of the decomposition written as in (5.2.12), which correspond to the the slowest modes of the flow. When we analyse the modes on the single components, we find that the first level of the decomposition of every component is composed by a single mode, whose frequency is exactly zero. This happens both at $y^+ \approx 15$ and at the centerline for all the velocity fields, except for the wall-normal velocity close to the wall, whose first level of decomposition has no modes. Moreover all the non oscillating modes have eigenvalues close to

5.4 Results

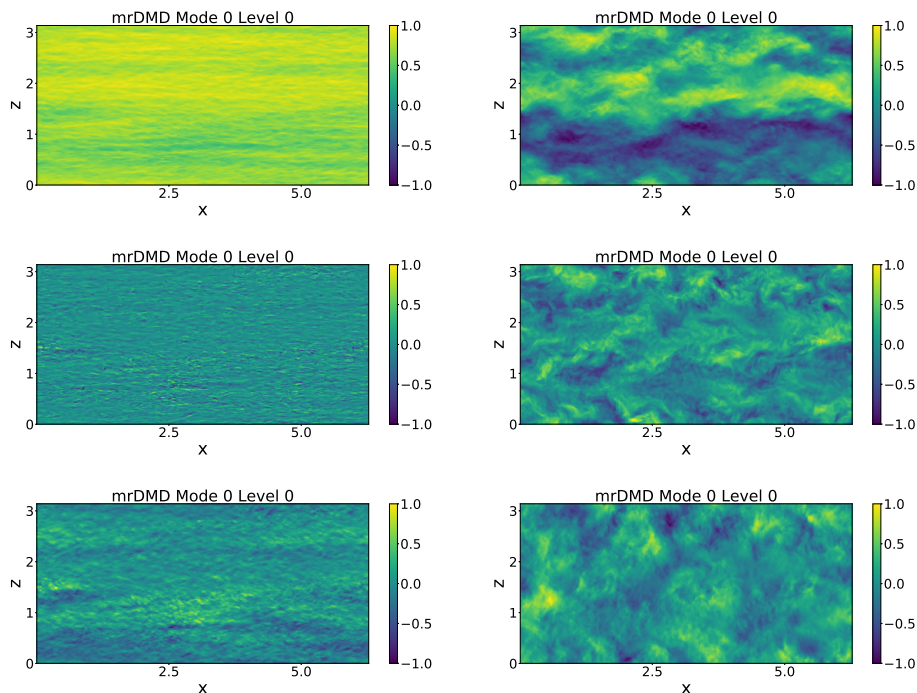


Figure 5.5: Real part of the slowest structure in the rotationless case $R_\Omega = 0$, near the wall at $y^+ \approx 15$ (left) and at the centerline $y = h$ (right). The panels correspond to the mode derived, from top to bottom, from the v_x (streamwise), v_y (wall-normal) and v_z (spanwise) velocity components.

the origin of the axis, which means that they are all either slightly decaying or perfectly stable modes.

If we now perform the method on the velocity fields simultaneously, we observe that, in contrast to the $R_\Omega = 0$ case, the first level of the decomposition both close to the wall and at the centerline has no imaginary component.

This more complex scenario is confirmed if we look at the amplitudes in figure 5.7. Again we have that for the streamwise velocity, the first mode is the one that has the largest influence in determining the evolution of the flow. However, this mode is now marked at the centerline for the wall-normal velocity and at the near-wall in the spanwise component. This configuration is confirmed when we perform the method on the velocity fields simultaneously, since both close to the wall and in the centerline the first mode is dominating the dynamics of the flow. These properties are also reflected when visualizing the slowest mode obtained with the analysis applied to the three velocity fields simultaneously in figure 5.8. In this case there is clear presence of the large structures in both streamwise and wall normal components at the centerline, and streamwise and spanwise direction close to the wall.

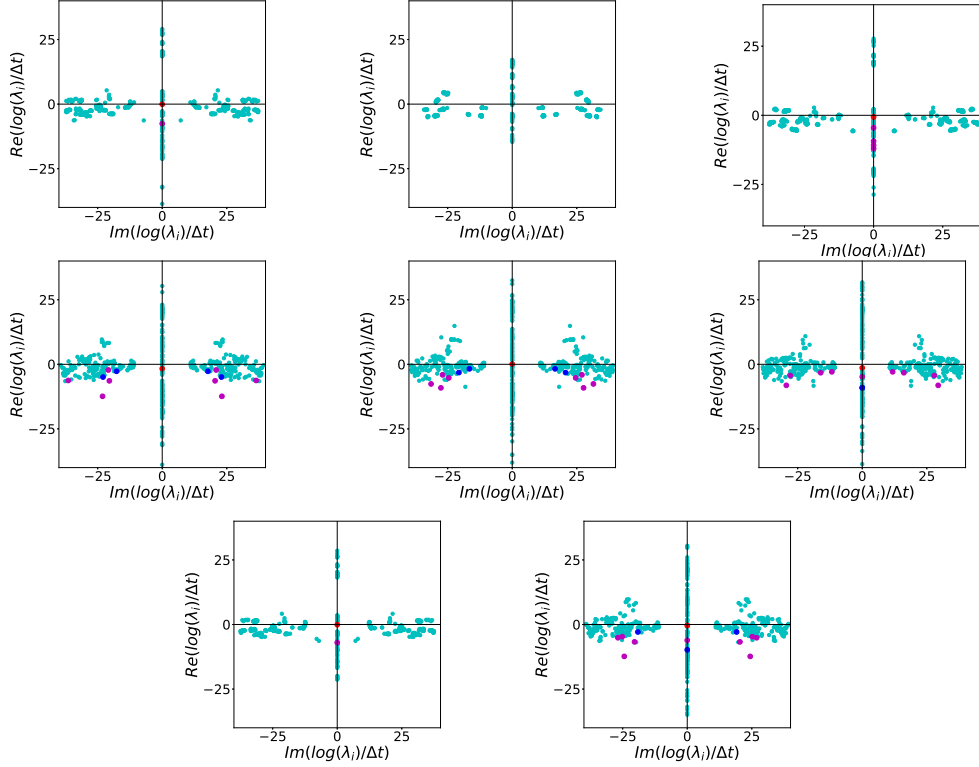


Figure 5.6: Growth/decay and frequency of the modes $\delta_k + i\omega_k = \frac{|\log(\lambda_k)|}{\Delta t}$ in the case with anti-cyclonic rotation $R_\Omega = 0.1$, near the wall at $y^+ \approx 15$ (top row) and at the centerline $y = h$ (central row). The panels correspond to the mode derived, from left to right, from the v_x (streamwise), v_y (wall-normal) and v_z (spanwise) velocity components singularly. The last row corresponds to the the modes derived from all the velocities simultaneously, close to the wall (left) and at the centerline (right). In the panels the first three levels of iteration of equation (5.2.12) are highlighted with colors as in figure 5.3.

With mrDMD we have confirmed nothing more than a clear detection of the organized, pinned structures of RPC flow as described in [155, 132]: at the centerline there is a strong correlation between the v_x and v_y velocity component due to the Coriolis force. On the other hand, close to the wall the v_y velocity component has to be very close to zero, and owing to the existence of the roll large structure, there has to be a strong v_z component. With this analysis we can say that without rotation, i.e., with $R_\Omega = 0$, we do not see a clear coupling coupling between the structures across velocity directions, while for the anti-cyclonic case, $R_\Omega = 0.1$, the three components of velocity are strongly coupled.

This could be a first step to explain why the rolls are fixed when we add rotation, and they are not if this is missing: for $R_\Omega = 0$ these large structures

5.4 Results

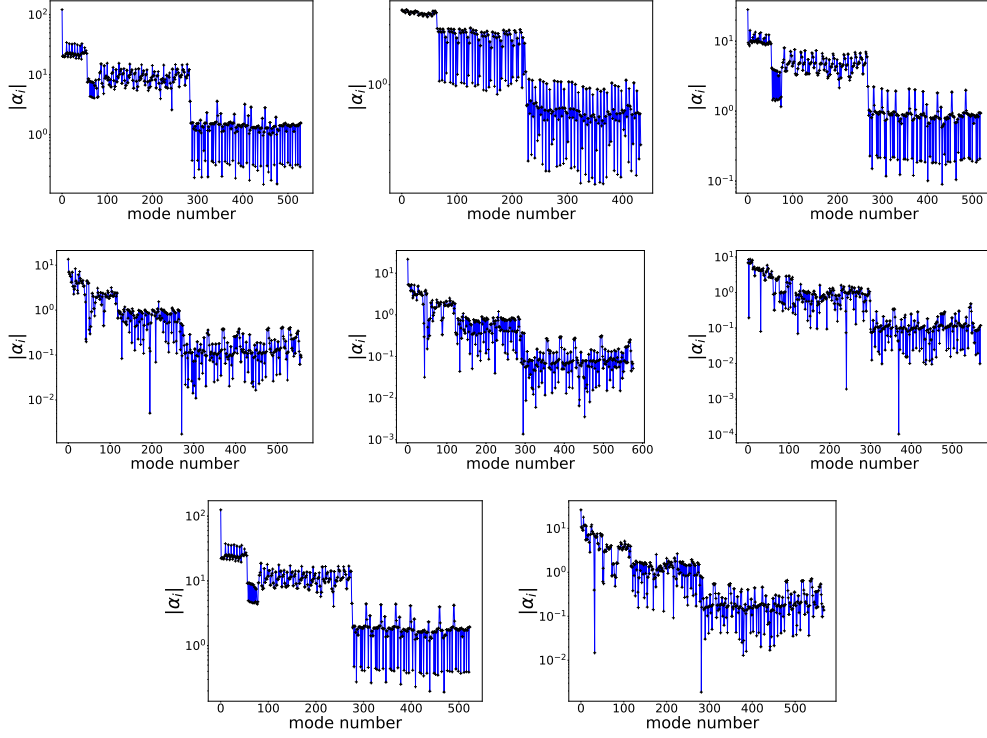


Figure 5.7: Amplitude α_i of the modes in the case with anti-cyclonic rotation $R_\Omega = 0.1$, near the wall at $y^+ \approx 15$ (top) and at the centerline $y = h$ (center). The panels correspond to the mode derived, from left to right, from the v_x (streamwise), v_y (wall-normal) and v_z (spanwise) velocity components singularly. The last row correspond to the the modes derived from all the velocities simultaneously, close to the wall (left) and at the centerline (right).

are just “eigenmodes” of the streamwise velocity, while for $R_\Omega = 0.1$ the Coriolis term is modifying the eigenmodes by forcing the coupling between the velocity components, in particular of v_x and v_y in the centerline.

5.4.2 HODMD

In this section we want to test the reliability of the results obtained in the previous section by applying HODMD: a different variant of standard DMD which is appropriate to study periodic and quasi-periodic dynamics, as we have already pointed out in section 5.2, or in general to that dynamics that show limited spatial complexity but a very large number of involved frequencies. Moreover HODMD has the possibility of fine-tuning the order parameters d , and the tolerances ϵ_1 and ϵ_2 . In this way we gain both the ability of getting

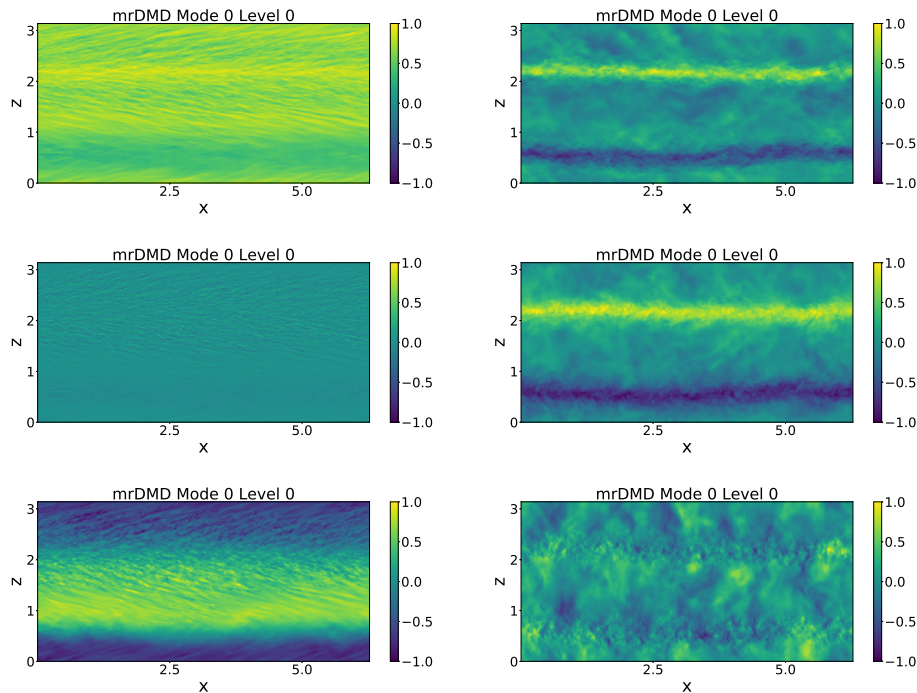


Figure 5.8: Real part of the slowest structure in the case with anti-cyclonic rotation $R_\Omega = 0.1$, near the wall at $y^+ \approx 15$ (left) and at the centerline $y = h$ (right). The panels correspond to the mode derived, from top to bottom, from the v_x (streamwise), v_y (wall-normal) and v_z (spanwise) velocity components.

rid of noise or discretization/truncation errors and thus avoid capturing unphysical modes, and also the possibility get rid of irrelevant or spurious modes by eliminating small amplitude modes.

Due to these reasons, we applied HODMD on a collection of 100 2D snapshots on the three velocity fields simultaneously, but however focusing on the streamwise velocity at the centerline. For this method, we use a larger temporal step between snapshots of $\Delta t U/h = 4 \times 10^{-1}$, in order to focus more on slower evolving structures, and compare the output obtained when varying $\epsilon_1 = \epsilon_2 = 10^{-2}, 10^{-4}, 10^{-6}$, and changing $d = 2, 5, 10, 50$ for $R_\Omega = 0$ and $d = 2, 10, 20, 50$ for $R_\Omega = 0.1$.

As we can see from figure 5.9, fixing the order and reducing the tolerance value increases the number of retained modes. On one side these modes are located at higher values of frequencies, indicating that they are related with high frequency, small scale structures; on the other side there is an increasing number of spurious modes, which are high frequency modes with high amplitudes. This happens for all the values of order d considered, and for both the rotation and the rotationless cases. Because of this, in figure 5.10 we fix the

tolerances to $\epsilon_1 = \epsilon_2 = 10^{-2}$ and vary the order of the method d in both rotation and rotationless cases. As we can see, we have that the order that better captures the complexity of the flow in its large scales without introducing spurious effects is $d = 10$ for both $R_\Omega = 0$ and $R_\Omega = 0.1$, both highlighted with the black markers. Moreover these two figures emphasize the greater number of eigenvalues/eigenmodes when anti-cyclonic rotation is present with respect to the rotationless case, and the less clear pattern in the influence of them in the evolution of the flow.

It is worth noting that, in contrast with mrDMD, the dominant mode captured by HODMD has zero frequency, while with mrDMD the rotationless case was exhibiting an oscillating behaviour. This could be a consequence to the fact that HODMD is more appropriate to detect periodic or quasi-periodic dynamics, thus it is isolating the streamwise, quasi-steady large scale mode; on the other side seems that mrDMD is keeping also the dynamics of the other two velocity fields, which are faster and oscillatory.

There is another interesting behavior that can be studied if we look now at the frequencies ω_k of the eigenvalues. If we look at figure 5.11, we can see a spectral decay of frequencies of the modes, indicating a period cascade in the periodicity lengthscale of the eigenmodes. In a better way, we can say that the largest scales of the streamwise velocity can be decomposed in a mean flow (zero frequency) and a single periodic wave that repeats itself in the higher modes doubling its frequency in space with the mode number.

This behavior is clearly visible if we plot the slowest in frequency modes, as we have done in figure 5.12. In both, rotation and rotationless, cases we capture the largest, zero-frequency structures that are almost identical to the ones found with mrDMD in figure 5.5 and 5.8. We also capture oscillating structures, whose frequency is faster with the increasing mode order. This behavior recalls a result found for Rayleigh-Bénard flow during the transition to turbulence in [170]. During the transition it was found a fundamental harmonic with all the subharmonics of that fundamental oscillation frequency that during the transition was also indicating a route to chaos following a period-doubling scenario, until the transition to turbulence is complete, and the frequency spectrum appears as a continuous curve. It is possible than that a similar behavior could be present also for PC and RPFC flow, and that even at a completely turbulent flow, the largest scales still preserve the fundamental frequency with all the subharmonics, as a footprints of the transition.

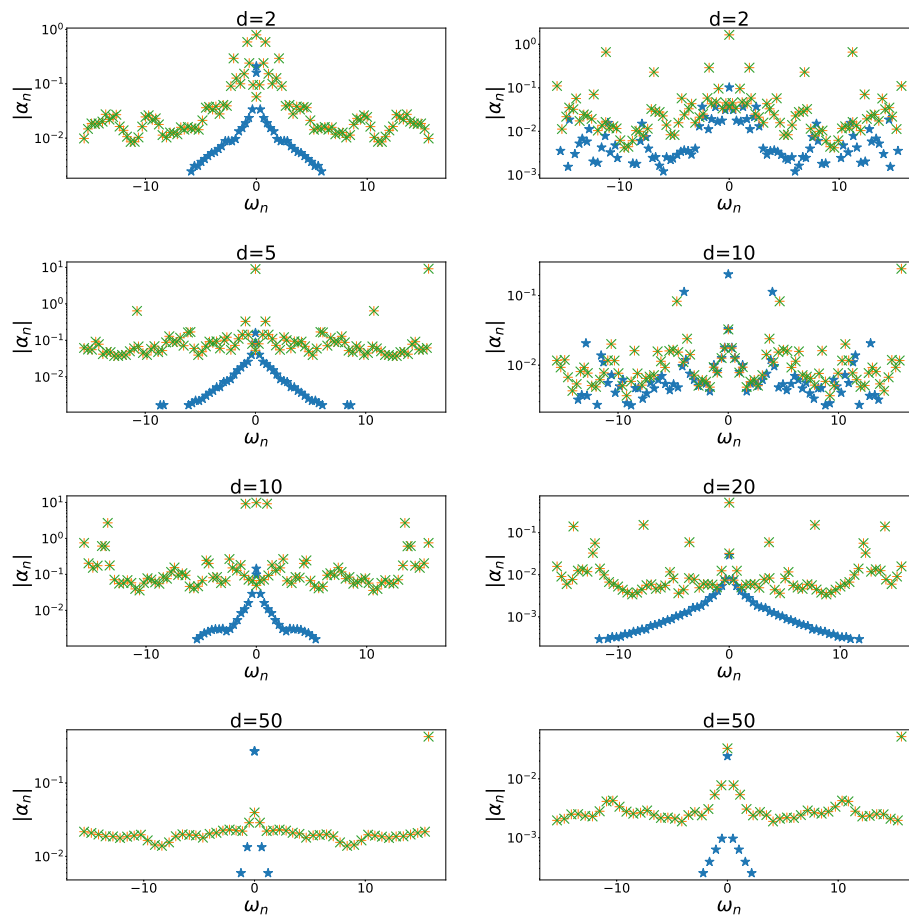


Figure 5.9: Amplitude on frequency plot of the eigenvalues of the streamwise component of the velocity for a fixed order d of HODMD and varying the tolerances between values $\epsilon_1 = \epsilon_2 = 10^{-2}$ (stars), 10^{-4} (pluses) and 10^{-6} (crosses). Left: $R_\Omega = 0$ case; right: $R_\Omega = 0.1$

5.5 Summary and conclusion

In this manuscript, we applied two variants of standard DMD on PC flow and RPC flow. The aim of the work was to find a filter for large-scale structures that was robust across the parameter space and that was able to correctly detect the coherent structures arising in the turbulent flow.

We first used mrDMD on a large amount of 2D snapshots, and this method was able to capture the different behaviors of the structures in the flow. In particular, we showed that when there is no added rotation, the large structures develop predominantly in the streamwise component, and are decoupled from the other velocity components, that show no evident structures; this means that the wavyness in the streamwise structures has no effect on both wall-

5.5 Summary and conclusion

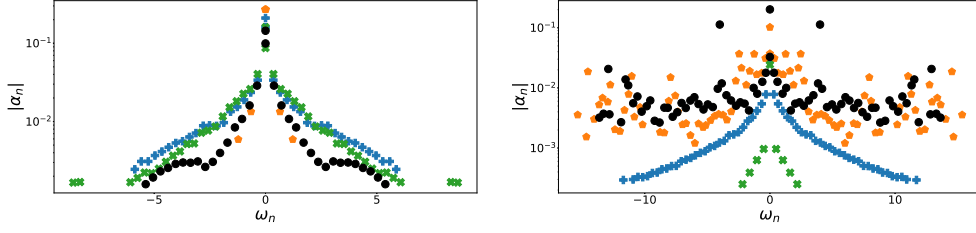


Figure 5.10: Amplitude on frequency plot of the eigenvalues of the streamwise component of the velocity for a fixed tolerance $\epsilon_1 = \epsilon_2 = 10^{-2}$ and varying the order of the method d between values $d = 2$ (pluses), $d = 5$ (crosses), $d = 10$ (circles) and $d = 50$ (pentagons) for the $R_\Omega = 0$ case (left panel), $d = 2$ (pentagons), $d = 10$ (circles), $d = 20$ (pluses) and $d = 50$ (crosses) for the $R_\Omega = 0.1$ case (right panel).

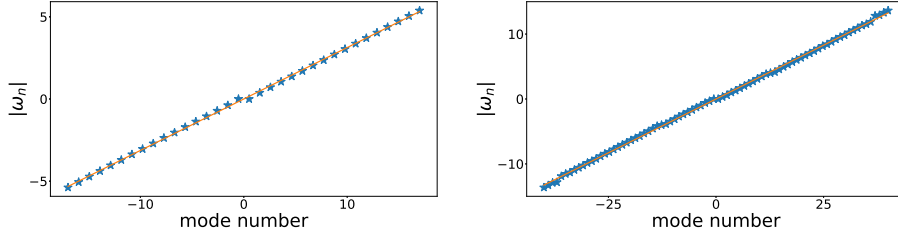


Figure 5.11: Frequency of the eigenvalues (stars) and linear fit (solid line), for $R_\Omega = 0$ (left) and $R_\Omega = 0.1$ (right).

normal and spanwise directions. On the other side, when rotation is added on the system, large structures are detected both in streamwise and wall-normal components; this means that the Coriolis force is forcing the coupling among the different components of the flow.

We also applied HODMD on a smaller selection of snapshots with a greater spacing in time, as in this way the method is able to eliminate small scale components and spurious elements that arise elsewhere. This serves as a check on mrDMD's accuracy. We found the same coherent structures for the two methods. Moreover, we detected an extra feature: large scales of both both PC and RPC systems can be decomposed in mean flow (the zero frequency stable elongated structures) and a single periodic wave, or harmonic, that repeat itself in the smaller structures with a doubling period cascade. This feature can be linked to the period cascade in the route to turbulence in Rayleigh-Bénard flow.

With this work, we have demonstrated that DMD methods can be a robust and reliable way to capture the large scale motion and try to understand their origin and their pinning. However there are known issues due to the large

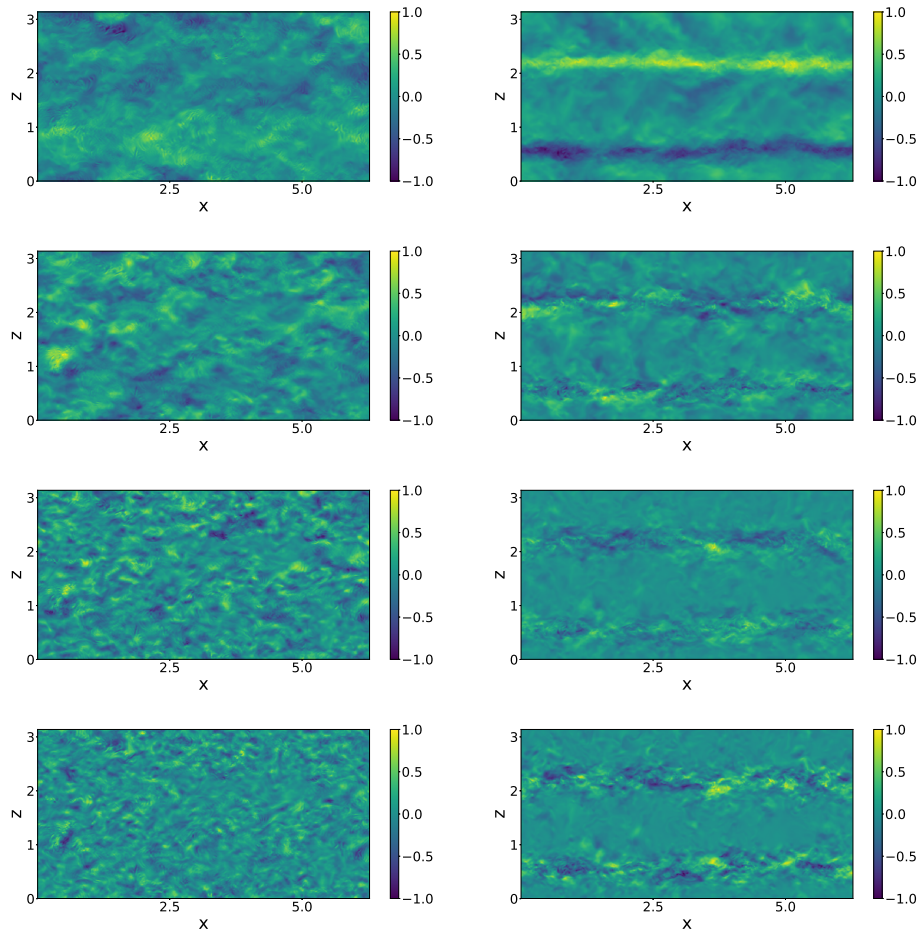


Figure 5.12: Real part of the largest structure in the rotationless case $R_\Omega = 0$ (left panels) and anti-cyclonic rotation $R_\Omega = 0.1$ (right panels) at the center-line $y = h$, for the v_x (streamwise) velocity components. The panels represent, from top to bottom, the zero-frequency mode, the first, second and third harmonics.

amount of snapshots that DMD methods need to properly capture the motion. For this reason this analysis was limited to a small size domain and to 2D collection of snapshots instead of full 3D fields. Thus to develop a full three-dimensional model for the structures we need to reduce the computational load of the methods used in this manuscript, using for example a further reduction of the dimension of the snapshot matrix, or a parallel distributed version of the codes on multiple CPUs or GPUs.

Chapter 6

Linear correction of the turbulent velocity profile for a small gap Taylor–Couette flow

Based on: Francesco Sacco, Paolo Luchini & Roberto Verzicco, ‘Linear correction of the turbulent velocity profile for a small gap Taylor–Couette flow’, in preparation.

6.1 Introduction and background

Most of the turbulent flows are bounded, at least in part, by one or more solid surfaces. The classical theory of these flows states that the distribution of the streamwise velocity in the wall–normal direction of a turbulent fluid flow near a boundary with a no–slip condition has a common behavior. This theory comes after the works of von Kármán [174] and Prandtl [123]: starting from the experiments and from the mixing–length argument of Prandtl [122], they recognize a layer in the wall–normal direction, called “overlap” region, where the viscous contribution due to the wall is small but also where the turbulent shear stress has a constant intensity. From this assumptions they derived the logarithmic law of the wall – or simply the *log law*:

$$u^+ \simeq A_0 \log(y^+) + B, \quad (6.1.1)$$

where the reciprocal of the A_0 coefficient is known as von Kármán constant $k = \frac{1}{A_0}$. Here $u^+ = \frac{u}{u_\tau}$, $y^+ = \frac{yu_\tau}{\nu}$, $u_\tau = \sqrt{\frac{\tau_w}{\rho}}$, where τ_w is the wall shear stress, ν the kinematic viscosity and ρ the fluid density. Quantities with the superscript + are also commonly denoted as measured in “wall units”.

The theory in its present form is based on dimensional analysis by Millikan [98], and it is based on an asymptotic expansion in the limit of $Re_\tau \rightarrow \infty$, where the shear–based friction Reynolds number $Re_\tau = \frac{hu_\tau}{\nu}$ is a typical parameter that identifies how turbulent is the flow. Since this law was formulated for a flow between parallel walls and in absence of pressure gradient, a basic ansatz of this theory is the uniformity of the shear stress in the wall layer. Moreover an other assumption comes from the link between the externally imposed pressure gradient p_x and the wall mean shear stress τ_w , derived from force balance: if A is the area of the duct cross section and LP its lateral area, product of length L and perimeter P , static equilibrium requires that:

$$-Ap_xL = LP\tau_w, \quad (6.1.2)$$

or

$$p_x = -\frac{4\tau_w}{D_h}, \quad (6.1.3)$$

where the quantity $D_h = 4A/P$ goes by the name of hydraulic diameter, because in a circular pipe it coincides with its diameter, and in other cases, it has the role of diameter of an equivalent pipe with the same volume to area ratio.

From the uniformity of the shear stress and equation (6.1.2) (or (6.1.3)) one can conclude that, for a given geometry, only one of τ_w or p_x must be specified;

however, one has not to forget that these relations have been developed for specific systems with particular hypotheses, and so these two quantities could be differently related in different geometries.

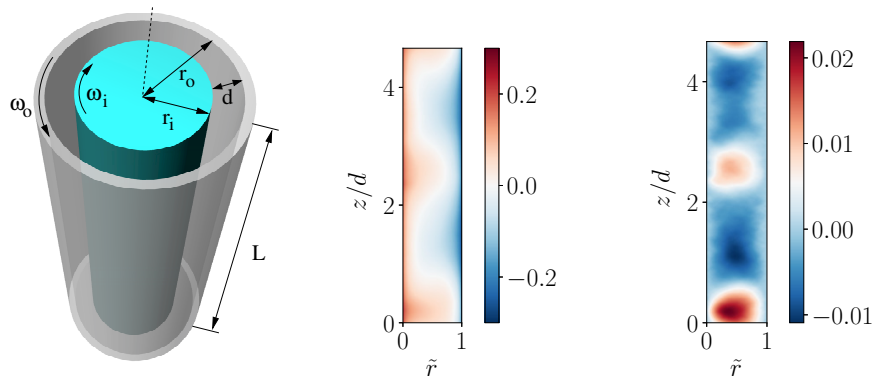


Figure 6.1: Left panel: classical setup of a TC system; the fluid fills the gap $d = r_o - r_i$ between coaxial cylinders with radii r_i and r_o , which rotate independently with the angular velocities ω_i and ω_o , respectively. Central panel: temporally- and azimuthally averaged azimuthal velocity \bar{u}_θ . Right panel: temporally- and azimuthally averaged radial velocity \bar{u}_r .

Taylor–Couette (TC) flow, the flow between two coaxial, independently–rotating cylinders (see figure 6.1), has successfully been used as a model system to study turbulence, and the influence of curvature and rotation on the flow [150, 53]. This system has a complex phase diagram, due to the effects of linear instabilities [6], and in the unstable regime one can observe Taylor rolls, modulated waves, spirals, and many other rich spatial and temporal flow features.

Since the classical asymptotic theory developed by Prandtl and von Kármán requires that $Re_\tau \rightarrow \infty$, we are interested in the TC flow with highly turbulent state, i.e. with extremely high Reynolds number, in which the bulk flow as well as the boundary layers are turbulent [58, 111, 53]). For this case the profile was believed to be described by the law of the wall in equation (6.1.1). Evidences for such a universal behaviour were provided by both experiments and numerics [58, 111], obtaining a von Kármán constant $k \approx 0.4$, similar to the one found for other wall–bounded turbulent flows [141, 140, 9].

This agreement is quite surprising, since, unlike pipe or channel flows, the effects of the streamwise curvature and the shear forces due to rotation give rise to additional instabilities, which manifest themselves as Taylor rolls [150]. It has been seen that these coherent structure develop along the whole gap, and their interaction with the main flow alters the overall large–scale features and transfer properties. Moreover, under certain condition they can survive

up to extremely high Reynolds numbers [111, 59, 132].

A less surprising agreement comes from the comparison between TC flow and plane Couette (PC) flow, the shear-driven flow between two parallel plates, or rotating plane Couette flow (RPCF), i.e. PC flow with an added solid-body rotation in the spanwise direction. Indeed it has been found in [17] that in the limit of low curvature there is a collapse between various radius ratios TC flows and RPCF, even varying the angular velocity (and so the rotation intensity) of the walls of the two systems, indicating a turbulent behaviour common to both systems. This agreement has been observed in the torque, mean momentum transport, mean profiles, and turbulent fluctuations.

Moreover, both systems are characterized by an absence of pressure gradient effects, both flows are driven only by wall shear effects and also PC flow and RPCF are characterized by the presence of large coherent structures consisting of rollers and/or streaks that occupy the whole channel [118, 8].

Also for this kind of system a logarithmic law has been numerically detected in [118], suggesting a best-fitting data parameters of $k = 0.41$ and $B = 5$, while in [88] the two parameters have been found as $k = 0.392$ and $B = 4.48$. However, one of the big differences between results obtained for TC flow and the ones of PC flow is that most of studies in TC flow have been carried out for the pure inner cylinder rotation only, while in PC flow both walls were kept with same velocity magnitude, and opposite directions. It has been shown [17] that different rotation ratios cause different responses of the systems; in particular even when the flow is driven at constant driving strength, a maximum in angular momentum transport can be found for a certain values on rotation ratio [115, 167, 53].

Therefore, in order to avoid all of these effects on TC flow, in this chapter we have setup the system so to have counter-rotating cylinders with angular velocity equal in magnitude. In this way we intend to provide a better match with existent studies on PC flow and, at the same time, to focus only on the effects on the log law due to curvature, and not to the ones caused by the differential rotation of the two walls.

The chapter is organized as follows: in section 6.2 we briefly recall the pressure gradient correction found in [87, 88] for straight geometries and then we derive the analogous equation for TC flow, based on the relation between the wall shear stress and the conserved transverse current of azimuthal motion found by Eckhardt et al. [43]. In section 6.3 we describe the numerical method used and the parameter setup used in the simulations. The log law parameter estimation and the comparison between the corrected mean velocity field and the log law are reported in section 6.4. In section 6.5 we summarize all the

findings and give some remarks and an outlook for future works.

6.2 The linear correction

6.2.1 Pressure–gradient correction to the overlap layer

In [87, 88], an asymptotic expansion of the mean streamwise velocity u^+ has been proposed, after the observation that in the overlap layer, the dimensionless quantity $\frac{y \frac{\partial u}{\partial y}}{u_\tau}$ is almost independent of h and ν , but is acted upon by p_x as by a small perturbation.

The analysis starts from the link between the externally imposed pressure gradient p_x and the wall mean shear stress τ_w stated in equations (6.1.2) and (6.1.3).

The effect of the pressure gradient is now no more interpreted as producing a variation of the value of von Kármán’s constant, rather is included in Millikan’s ansatz; this means that $\frac{y \frac{\partial u}{\partial y}}{u_\tau}$ is no longer a constant k^{-1} , but depends linearly on p_x (since we are imposing it as a small perturbation).

Simply from dimensional analysis, this extends the *log law* of von Kármán as:

$$\frac{\frac{\partial u}{\partial y}}{u_\tau} = \frac{1}{ky} - A_1 \frac{p_x}{\tau_w},$$

that integrates to:

$$u^+ = k^{-1} \log(y^+) + A_1 g Re_\tau^{-1} y^+ + B, \quad (6.2.1)$$

where A_1 is a new universal constant and the geometric factor $g = -hp_x/\tau_w = 4h/D_h$ appears due to nondimensionalization.

After applying the method that we are going to describe in section 6.4, it was found a best approximation of the log law holding for three geometries, a channel flow, a pipe flow and PC flow, with the parameters values of:

$$k = 0.392 \text{ or } A_0 = \frac{1}{k} = 2.55, \quad B = 4.48;$$

moreover a common value of $A_1 = 1$ was found for the three geometries, and simply from the definition, the geometric factor is $g = 1$ for channel flow, $g = 2$ for pipe flow, $g = 0$ for PC flow, bringing to the different values for the linear correction parameter $A_1 g$.

6.2.2 Correction to the overlap layer in Taylor–Couette flow

We now want to apply the idea of section 6.2.1 to TC flow. Hereafter we denote with r the wall–normal direction, and u_θ is our streamwise velocity. Using inner cylinder wall coordinate, the mean azimuthal profile is defined as $u_\theta^+ = \frac{u_{\theta i} - \langle u_\theta \rangle_{t,\theta,z}}{u_{\tau i}}$, while the distance to the inner cylinder is $r^+ = \frac{(r-r_i)u_{\tau i}}{\nu}$; using outer cylinder wall coordinate, the mean azimuthal profile is defined as $u_\theta^+ = \frac{\langle u_\theta \rangle_{t,\theta,z} - u_{\theta o}}{u_{\tau o}}$, while the distance to the outer cylinder is $r^+ = \frac{(r_o-r)u_{\tau o}}{\nu}$. As in PC flow, pressure gradient in TC is absent, $p_x = 0$, and the flow is driven only by the wall shear. However for TC flow we have that if the angular velocities of the cylinders are different, $\omega_i \neq \omega_o$, with $\omega = \frac{u_\theta}{r}$, there is an r -dependent profile of the azimuthal velocity u_θ . The consequence is a viscous as well as a convective transport of azimuthal momentum.

Following [43], we have that this u_θ -current is quantified by the constant value:

$$J^w = r^3 [\langle u_r \omega \rangle_{A,t} - \nu \partial_r \langle \omega \rangle_{A,t}], \quad (6.2.2)$$

where we average the u_θ -equation in time and over a cylindrical surface of axial height L_z and area $A(r) = 2\pi r L_z$, chosen to be co–axial to the rotating TC cylinders and lying between them, $r_i \leq r \leq r_o$.

The quantity J^w , indeed, corresponds to the conserved transverse current of azimuthal motion (possibly up to a constant factor), transporting the angular velocity $\omega(\mathbf{x}, t)$ in the radial direction.

It is important to note two things:

- $\frac{J^w}{r_{i,o}^2}$ is the r, θ component of the wall stress tensor:

$$r_{i,o}^{-2} J^w = -\nu r_{i,o} \left(\frac{\partial \omega}{\partial r} \right)_{r_{i,o}} = -\nu \left(\frac{\partial u_\theta}{\partial r} - \frac{u_\theta}{r} \right)_{r_{i,o}} = \tau_{w_{i,o}}. \quad (6.2.3)$$

- There is an explicit link between the azimuthal current and the torque T :

$$T = 2\pi L_z J^w. \quad (6.2.4)$$

If we look closer at equation (6.2.3), we see that there is an analogy between the role of the pressure gradient p_x in straight geometries and the conserved transverse current of azimuthal motion J^w : indeed equation (6.2.3) can be derived in a similar way to equation (6.1.3), coming again from force balance. To highlight more the analogy, we can note from equation (6.1.3) that the ratio between the pressure gradient and the wall shear stress has the dimension of the inverse of a length, and it is proportional to the hydraulic diameter:

$$\frac{p_x}{\tau_w} = \frac{4}{D_h}.$$

6.3 Numerical framework

In TC we have that the role of the hydraulic diameter is covered by the wall radius r_w : $\frac{J^w}{r_w^3 \tau_w} = \frac{1}{r_w}$.

For this reason the quantity $\frac{J^w}{r_w^3 \tau_w}$ can act as a small perturbation parameter in the asymptotic expansion of the mean streamwise velocity, that take in account the effects of the curvature on the flow, as the quantity $\frac{p_x}{\tau_w}$, used as a perturbation parameter in section 6.2.1, takes into account for the pressure effects on the flow.

Thus we have that:

$$\frac{\partial u_\theta}{\partial r} = \frac{1}{kr} - A_1 \frac{J^w}{r_w^3 \tau_w};$$

due to integration we get the first order correction, equivalent to equation (6.2.1):

$$\begin{aligned} u_\theta^+ &= \frac{1}{k} \log(r^+) - \frac{\nu}{u_\tau} r^+ A_1 \frac{J^w}{r_w^3 \tau_w} + B = \\ &= \frac{1}{k} \log(r^+) - A_1 g Re_\tau^{-1} r^+ + B. \end{aligned} \quad (6.2.5)$$

As in the previous case, we have a constant parameter A_1 and the geometric factor is now $g = \frac{h}{r_w^3} \frac{J^w}{\tau_w} = \frac{d}{2r_w^3} \frac{J^w}{\tau_w}$, with $d = 2h = r_o - r_i$ the gap between the cylinders.

6.3 Numerical framework

All the simulations are performed in a convective reference frame [41] such that the cylinders have opposite tangential velocities $\pm U/2$, and the entire system then rotates with angular velocity $\boldsymbol{\Omega} = \Omega_r f \mathbf{e}_z$ around the spanwise axis. In this way any combination of differential rotations of the cylinders is reflected as a Coriolis force. In this frame the two control parameters chosen are a shear Reynolds number $Re_s = Ud/\nu$ and a non-dimensional Coriolis parameter $R_\Omega = 2d\Omega_r f/U$.

The incompressible Navier–Stokes equations then become:

$$\nabla \cdot \mathbf{u} = 0, \quad (6.3.1)$$

$$\frac{\partial \mathbf{u}}{\partial t} + \mathbf{u} \cdot \nabla \mathbf{u} + R_\Omega \mathbf{e}_z \times \mathbf{u} = -\nabla p + Re_s^{-1} \nabla^2 \mathbf{u}. \quad (6.3.2)$$

This reference frame has been chosen since in the limit of a vanishing curvature, i.e. when $\eta = \frac{r_i}{r_o} \rightarrow 1$, TC flow reduces to PC flow (or RPCF) case [17]. Moreover we have decided to eliminate the effects of Coriolis forces, setting

the rotation parameter $R_\Omega = 0$. In this way, as we have said also in the introduction, we have been able to compare our results with what has already been done for channel flow, cylindrical pipe and, in particular, with PC flow in [87], [88].

Axially periodic boundary conditions are taken with a periodicity length L_z , expressed non-dimensionally as an aspect ratio $\Gamma = L_z/d$. In the azimuthal direction, TC is naturally periodic. However, a rotational symmetry of order N can be imposed on the system with a twofold purpose: to reduce computational costs and to explore the effects of the the streamwise periodic length on turbulent structures. In this study we have started setting for almost all values of Re_s and η the values of $\Gamma = 2.33$, which is enough to fit a single roll pair, so that their wavelength λ_z will be $\lambda_z = \Gamma = 2.33$, and an imposed symmetry of $N = 20$, which leads to a small computational box with streamwise periodicity length of around 2π half-gaps, the usual value considered for turbulent channel flow. Moreover this computational box is similar to the one used in [14, 109], where it was found that this domain does not affect asymptotic torque and mean statistics of the flow.

However even if the mean statistic does not change significantly, it was pointed out in [132] that computational domain can influence the behaviour of Taylor rolls around the transition to the ultimate regime for $R_\Omega = 0.1$, i.e. for pure inner cylinder rotation. In particular it was shown that rolls wander in the domain depending on the box-size: the larger the domain the smaller the spatial variations.

In our case, where $R_\Omega = 0$, such structures have a reduced order of magnitude with respect to the $R_\Omega = 0.1$ case; however, in order to avoid their effects on the log law, due to their motion in the domain, we are going to show the results obtained for the various η with an axial ratio of $\Gamma = 4.66$, that corresponds to two couple of roll pairs, and a large streamwise periodicity length of 8π half-gaps, that corresponds to an imposed symmetry of $N = 5$ for $\eta = 0.91$, $N = 10$ for $\eta = 0.95$ and $N = 25$ for $\eta = 0.98$. See appendix A for a brief discussion on the results obtained in the small domain.

A uniform grid is used in the azimuthal and axial directions, while a Chebychev-type clustering near the cylinders is used in the radial direction. For all the η cases $Re_s = 3.61 \times 10^4$ and $Re_s = 8.96 \times 10^4$ is set, leading to friction Reynolds numbers $Re_\tau \approx 500$ and $Re_\tau \approx 1000$ respectively; in order to get spatially resolved simulations, we take the criteria $\Delta z^+ \approx 5$, $\Delta x^+ = r\Delta\theta^+ \approx 9$ and $\Delta r^+ \in (0.5, 5)$, resulting in resolutions of $n_\theta \times n_r \times n_z = 1536 \times 512 \times 1024$ in the azimuthal, radial and axial directions respectively for $Re_\tau = 500$ and of $n_\theta \times n_r \times n_z = 3072 \times 800 \times 2048$ for $Re_\tau = 1000$. In order to achieve temporal convergence, the simulations are run until the difference between

the time-averaged torque of the inner and the outer cylinders is less than 1%. The torque is then taken as the average between these two values. The simulations are then run for at least 40 large eddy turnover times tU/d . In this way the error due to finite time statistics can be estimated to be around 1%. A complete discussion of temporal time-scales is available in [111].

6.4 Results

In order to check the validity of equation (6.2.5), we have extracted the mean azimuthal velocity profiles from various TC cases.

The first thing to do is to obtain a reliable value for the von Kármán parameter k , or better, of its inverse $A_0 = \frac{1}{k}$.

We want to remark that all the following analysis has been performed on the inner cylinder wall velocity profiles, in order to compare with existing literature. However, since TC flow is not axisymmetric, the same method has been applied also to the outer cylinder wall profiles, and the results are shown at the end of this section.

We first note that equation (6.2.5) is consistent with a pair of matched asymptotic expansions *à la van Dyke* [166] of the wall and defect layers, in which an asymptotic expansion in powers of $(h^+)^{-1} = Re_\tau^{-1}$ of the former is matched to a Taylor series in powers of $\tilde{r} = \frac{r-r_i}{h}$ of the latter. If we assume that the layered structure of the turbulent velocity profile can also be recast as a uniformly valid approximation, we can write the velocity profile as:

$$u^+ = f_0(r^+) + Re_\tau^{-1}f_1(r^+) + Re_\tau^{-2}f_2(r^+) + \dots \\ + G_0(\tilde{r}) + Re_\tau^{-1}G_1(\tilde{r}) + Re_\tau^{-2}G_2(\tilde{r}) + \dots, \quad (6.4.1)$$

where the function $G(\tilde{r})$ represents the deviation of velocity in the defect layer from the logarithmic law, and it is also known as “*the law of the wake*”, from the work of Coles [29]. In this way, if we look at the first order approximation, that in our case is nothing but equation (6.2.5), we have associated its logarithmic and constant terms to f_0 and its linear term to G_0 .

In order to get a good evaluation of the parameter A_0 , we want to eliminate the effects of the wake function on the logarithmic law. We rewrite equation (6.2.5) in terms of outer coordinate \tilde{r} :

$$u_\theta^+ = A_0 \log(\tilde{r}) - A_1 g \tilde{r} + A_0 \log(Re_\tau) + B. \quad (6.4.2)$$

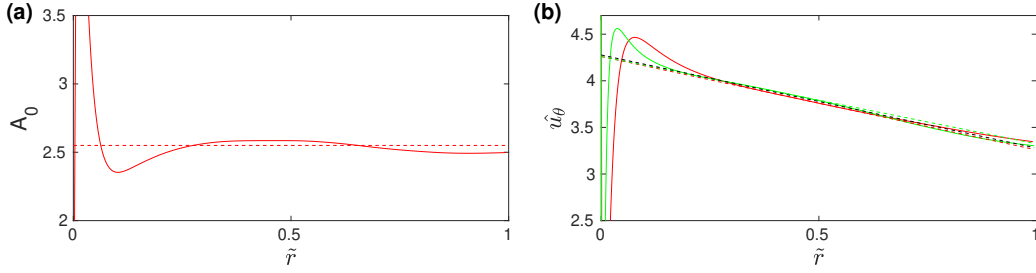


Figure 6.2: (a) Wake elimination procedure. The solid line is the difference of two curves at $Re_\tau = 1000$ and $Re_\tau = 500$ at $\eta = 0.91$. The dashed line is expected value of $A_0 = 2.55$. (b) A_1g coefficient evaluation from $\hat{u}_\theta = u_\theta^+ - A_0 \log(\tilde{r})$ curves (solid lines) at $Re_\tau = 1000$ (green) and $Re_\tau = 500$ (red). The dashed lines correspond to the best linear fit with coefficient $A_1g = -1.00$, $B = 4.26$ for $Re_\tau = 500$ (dashed red), $A_1g = -0.94$, $B = 4.26$ for $Re_\tau = 1000$ (dashed green) and a collective fitting of $A_1 = -1.00$, $B = 4.28$ (dashed black).

If we subtract two different velocity profiles u_1^+ and u_2^+ at two different Reynolds numbers Re_{τ_1} and Re_{τ_2} , at the same values of \tilde{r} , the result would be (at least in the overlap layer) to eliminate the wake function, and since the logarithmic law is assumed to be valid for both the profiles, the result of the subtraction would be a constant value

$$\begin{aligned} u_{\theta_2}^+(\tilde{r}) - u_{\theta_1}^+(\tilde{r}) &= \Delta f_{21}(\tilde{r}) = \\ &= A_0 \log \left(\frac{Re_{\tau_2}}{Re_{\tau_1}} \right). \end{aligned}$$

If we then divide this value by $\log \left(\frac{Re_{\tau_2}}{Re_{\tau_1}} \right)$, the result is expected to be a horizontal line of value value of A_0 , as it is confirmed in figure 6.2: in panel (a) we have plotted the profile taken from the difference between two Reynolds number, $Re_\tau = 500$ and $Re_\tau = 1000$, in case of a small gap $\eta = 0.91$, an aspect ratio $\Gamma = 4.66$ and azimuthal symmetry of $N = 5$. In appendix A we have reported also the results obtained with this procedure to many more Re_s at $\Gamma = 2.33$ and $N = 20$.

What we can see from this picture is very similar to what has been found in figure 9 in [88]: once inside the defect layer, the curve tends to align along a horizontal line of value $A_0 = 2.55$.

Once we have evaluated A_0 , to get A_1g and B it is enough to consider the quantity $\hat{u}_\theta = u_\theta^+ - A_0 \log(r^+)$ and look at the linear part of each function. This is done in the left panel of figure 6.2: we can see that both profiles have

a common rectilinear path between $r^+ \sim 200$ and $h/2$, whose slope is very close to -1 , and that have their origin at 4.28.

As practical purpose, since the values obtained for the two Reynolds number were slightly different, in order to get uniquely valid values for both the profiles, we have performed a linear fit between all points of the two curves in the region where the log law would hold, approximately $200\nu/u_\tau \leq r \leq d$, and consider the coefficients obtained as the best value for the parameters in equation (6.2.5).

In this way, at the end of the procedure, we have as von Kármán constants the values of

$$k = 0.392, \quad B = 4.28,$$

and the linear correction parameter

$$-A_1 g = -1.$$

We note that the coefficient B is slightly different from the value $B = 4.48$ found in [87], probably due to some η dependence, as we will show later.

In panels (a), (b) of figure 6.3 we show the velocity profiles u_θ^+ compared with the profile $u_\theta^+ + A_1 g Re_\tau^{-1} r^+ = u_\theta^+ - Re_\tau^{-1} r^+$ in order to check the validity of the log law in its original form of equation (6.1.1). As a further test, on panels (c), (d) we have checked also the logarithmic derivatives $r^+ \frac{\partial u_\theta^+}{\partial r^+}$ of both the profiles. All the plots are done, as we have already said, for a small gap value of $\eta = 0.91$, that means a gap $d = 0.1$ and radii $r_i = 1$ and $r_o = 1.1$. In this way we have that the geometric parameter becomes $g \sim 0.05$ and so $A_1 = 20$. What we can clearly see is a substantial improvement in the matching of the profile to the log law, both for velocity profile and its logarithmic derivative. In order to better show this, we have highlighted with vertical lines the zone where the log law holds, that is $200\nu/u_\tau \leq r \leq d$; in this zone we can immediately observe that when the correction is applied, not only the velocity profile behaves linearly as (6.1.1), but also the logarithmic derivative becomes almost horizontal.

We want to remark here that for a fixed geometry, i.e. for a fixed curvature η , the parameters obtained with this procedure are independent on the particular Re_τ used, as reported in figure 6.3 and as we will see in a moment for different η . Indeed the prediction given on the logarithmic profile of the corrected velocity has to be independent of the particular Re_τ , as it is expected from equation (6.2.5), and the difference between the raw velocity profile and the corrected one becomes smaller for increasing Re_τ , since the classical asymptotic theory of the turbulent velocity profile is valid in the limit of $Re_\tau \rightarrow \infty$.

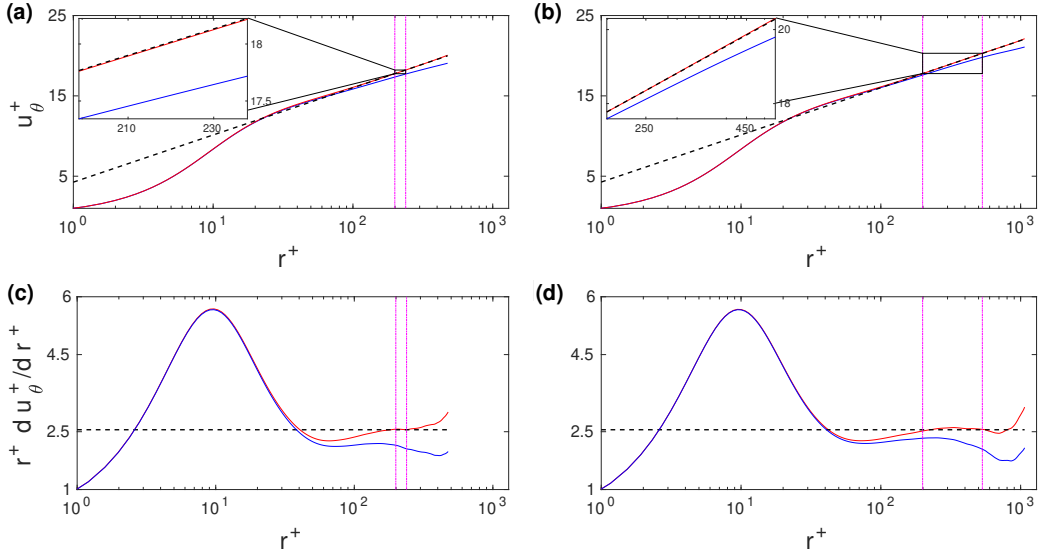


Figure 6.3: (a,b) Semi-logarithmic plot of temporally-azimuthally and axially averaged azimuthal velocity in wall coordinate u_θ^+ (blue), of the law of the wall $u^+ = 2.55 \log(r^+) + 4.28$ (dashed back), and of the wall velocity profile from which we have taken off the linear correction of equation (6.2.5) (red), for opposite rotation cylinders ($R_\Omega = 0$) at Reynolds number $Re_\tau = 500$ (a) and $Re_\tau = 1000$ (b) for radius ratio $\eta = 0.91$, at $\Gamma = 4.66$. (c,d) Logarithmic derivatives $r^+ \frac{\partial u_\theta^+}{\partial r^+}$ of the quantities in the top panels at Reynolds number $Re_\tau = 500$ (c) and $Re_\tau = 1000$ (d). The vertical magenta dot-dashed lines delineate the validity zone of the log law, approximately between $200\nu/u_\tau \leq r \leq d$.

In order to get better comparison with PC flow, we have repeated the same analysis for smaller curvatures $\eta = 0.95$ and 0.98 , as reported in figure 6.4. This has brought to values of $B = 4.36$, $-A_1 g = -0.59$ for $\eta = 0.95$ and $B = 4.44$, $-A_1 g = -0.26$ for $\eta = 0.98$, that are in agreement with the fact that we are reaching the values of $B = 4.48$ and $A_1 g = 0$ found in [88] for PC flow.

In figures 6.5 and 6.6 we show the velocity profiles $u_\theta^+ + A_1 g Re_\tau^{-1} r^+$ and their logarithmic derivatives $r^+ \frac{\partial u_\theta^+}{\partial r^+}$ as we have done for $\eta = 0.91$ in figure 6.3.

Again we can see an improvement in the matching of the profiles to the log law, both for velocity profile and its logarithmic derivative, highlighting with vertical lines the zone $200\nu/u_\tau \leq r \leq d$, where the log law holds.

Now that we have computed the parameters for different geometries, we can quantify the dependency of both the parameters $A_1 g$ and B on the different geometries. In figure 6.7 we have reported these parameters as a function of

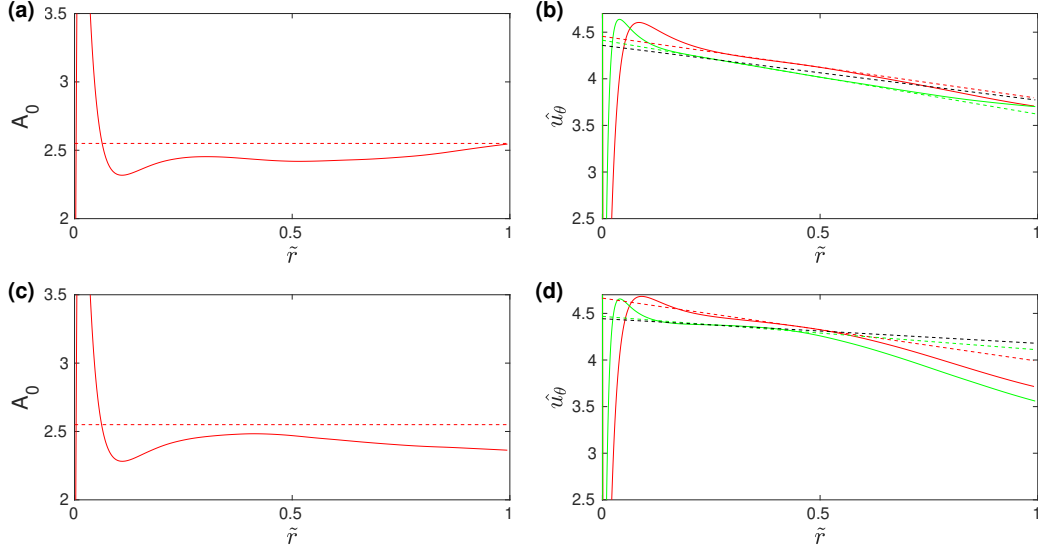


Figure 6.4: (a, c) Wake elimination procedure from the difference of two curves at $Re_\tau = 1000$ and $Re_\tau = 500$ (solid lines) for $\eta = 0.95$ (a) and $\eta = 0.98$ (b). The dashed line is expected value of $A_0 = 2.55$. (b, d) A_1g and B coefficient evaluation; for $\eta = 0.95$ (c) the best linear fit brings to the coefficients $A_1g = -0.66$, $B = 4.46$ for $Re_\tau = 500$ (dashed red), $A_1g = -0.79$, $B = 4.41$ for $Re_\tau = 1000$ (dashed green) and a collective fitting of $A_1 = -0.59$, $B = 4.36$ (dashed black); for $\eta = 0.98$ (d) the best linear fit brings to the coefficients $A_1g = -0.68$, $B = 4.66$ for $Re_\tau = 500$ (dashed red), $A_1g = -0.36$, $B = 4.47$ for $Re_\tau = 1000$ (dashed green) and a collective fitting of $A_1 = -0.26$, $B = 4.44$ (dashed black).

η adding also the values of $B = 4.48$ and $A_1g = 0$ found in [88] for PC flow. As we have already observed, our parameters approach the values of PC flow as $\eta \rightarrow 1$ and they do it linearly with η .

We want to remark here that this collapse of our parameters to PC flow case is not only numerical, but comes theoretically from the method: indeed, in the limit of vanishing curvature, i.e. when $d \rightarrow 0$ or $\eta \rightarrow 1$, the linear correction for TC system naturally reduces to the PC flow correction, where, as shown in [88], $g = 0$.

To do so, we write explicitly the geometric parameter:

$$g = \frac{d}{2r_w^3} \frac{J^w}{\tau_w} = \frac{r_o - r_i}{2r_w^3} \frac{J^w}{\tau_w}.$$

If we write it for the inner wall (but we can do the same for the outer wall), and we rewrite everything in terms of η :

$$g = \frac{r_o - r_i}{2r_i^3} \frac{J^{w_i}}{\tau_{w_i}} = \left(\frac{1}{2\eta r_i^2} - \frac{1}{2r_i^2} \right) \frac{J^{w_i}}{\tau_{w_i}}.$$

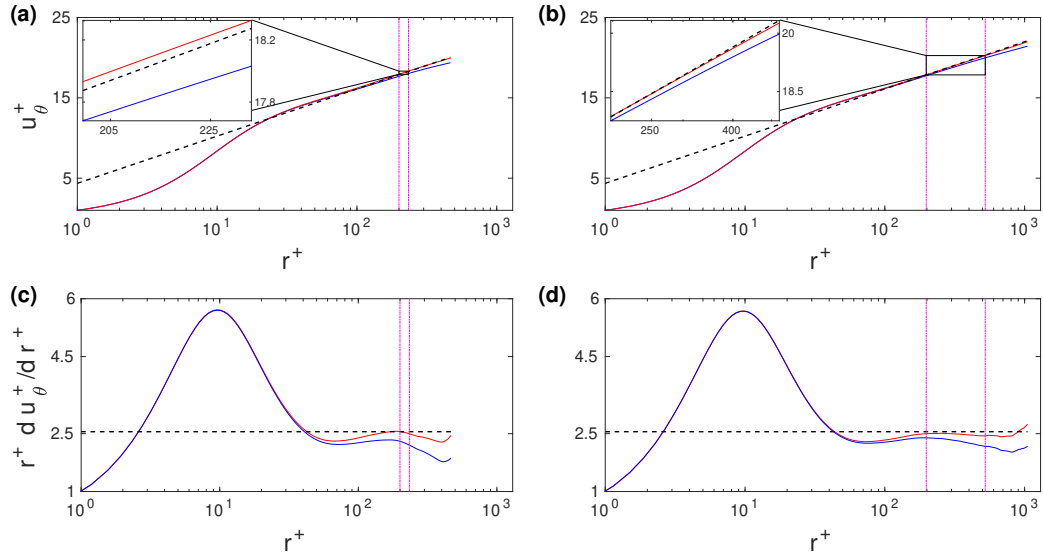


Figure 6.5: Semi-logarithmic plot of velocity profiles (a, b) and logarithmic derivatives (c, d) as in figure 6.3 for $\eta = 0.95$.

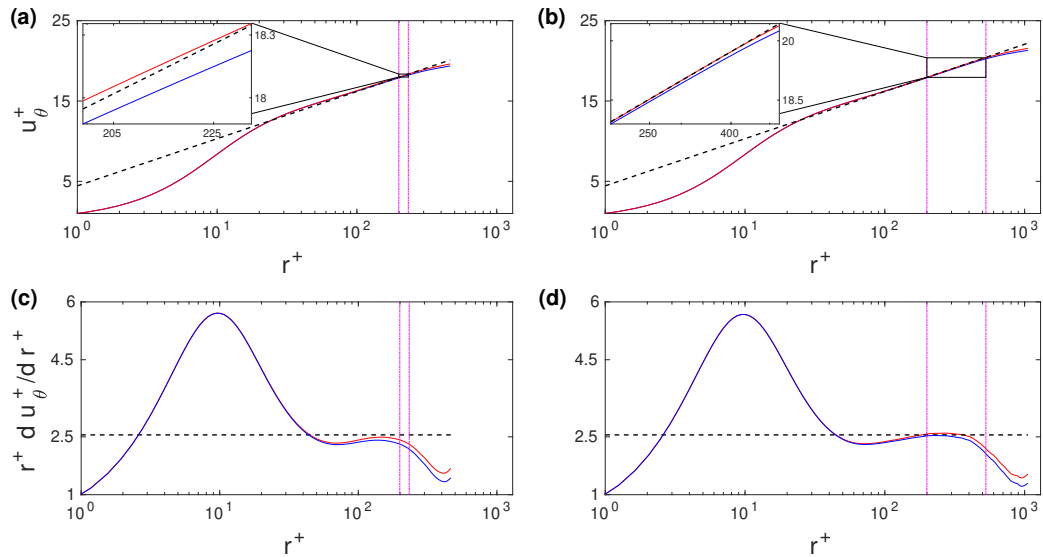


Figure 6.6: Semi-logarithmic plot of velocity profiles (a, b) and logarithmic derivatives (c, d) as in figure 6.3 for $\eta = 0.98$.

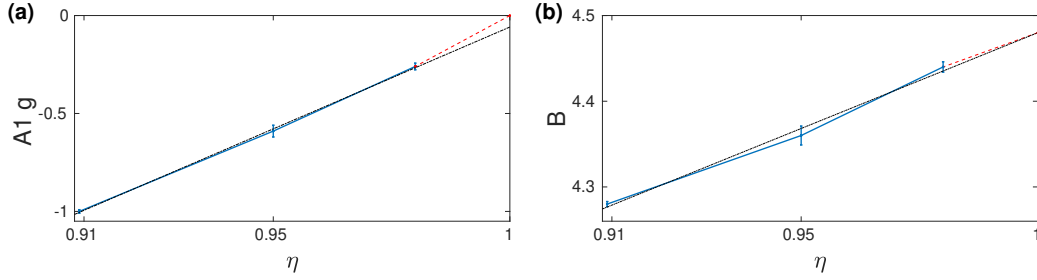


Figure 6.7: $A_1 g$ parameters (a) and B parameters (b) founded with the wake elimination procedure as a function of η (solid blue lines). The red dashed lines indicate the expected behaviour in the limit to PC flow ($\eta = 1$), while the black dot-dashed lines is the best linear fit to the data.

We then recall equation (6.2.3) and we get:

$$g = \frac{1}{2} \left(\frac{1}{\eta} - 1 \right) \frac{r_i^{-2} J^{w_i}}{\tau_{w_i}} =$$

$$\frac{1}{2} \left(\frac{1}{\eta} - 1 \right) \longrightarrow 0,$$

as $\eta \rightarrow 1$.

In order to complete our analysis, as we have introduced at the beginning of this section, we have applied the method also on the outer cylinder wall velocity profiles. We report in figures 6.8 and 6.9 the wake elimination procedure and the profiles obtained for $\eta = 0.91$. We have immediately to note that, due to the stabilizing effects of the concave surface and to the bigger extent of the outer cylinder surface, the frictional Reynolds number obtained at the outer wall is slightly lower than its internal counterpart, and the minimal value obtained is $Re_\tau \approx 430$; for this Reynolds number the logarithmic layer has just begun to develop. We have to ascribe to this feature the greater difference in the linear part of the two profiles in panel (b) of figure 6.8.

However there is again a good agreement with the value $k = 0.392$ of the von Kármán constant. With the obtained parameters of $B = 4.71$, $-A_1 g = 1.29$, we get again an improvement in the matching of the profiles to the log law, both for velocity profile and its logarithmic derivative, in the zone $200\nu/u_\tau \leq r \leq d$, where the log law holds.

As a final remark we just report here, without showing, that we expect this method to produce good results also for larger curvatures, since we have data up to $\eta = 0.714$. However for those smaller η we have performed simulations only for the small box case with $\Gamma = 2.33$ and a streamwise periodicity length of 2π half-gaps, and for this reason we prefer to postpone the complete analysis

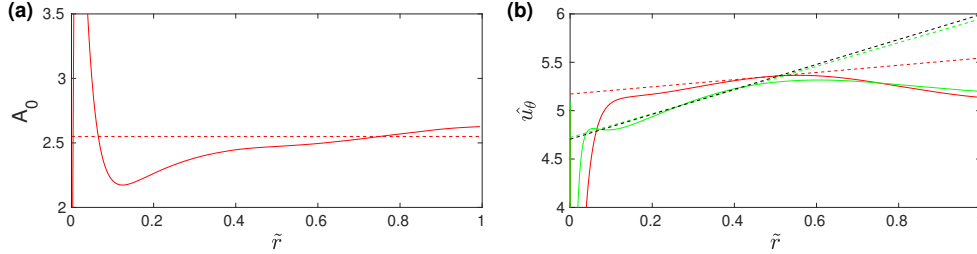


Figure 6.8: (a) Wake elimination procedure obtained from outer cylinder profiles at $\eta = 0.91$ obtained from the difference of two curves at $Re_\tau = 970$ and $Re_\tau = 430$ (solid line). The dashed line is expected value of $A_0 = 2.55$. (b) A_1g and B coefficient evaluation at $Re_\tau = 970$ (solid green) and $Re_\tau = 430$ (solid red). The dashed lines correspond to the best linear fit with coefficient $A_1g = 0.37$, $B = 5.17$ for $Re_\tau = 430$ (dashed red), $A_1g = 1.23$, $B = 4.73$ for $Re_\tau = 970$ (dashed green) and a collective fitting of $A_1g = 1.29$, $B = 4.71$ (dashed black).

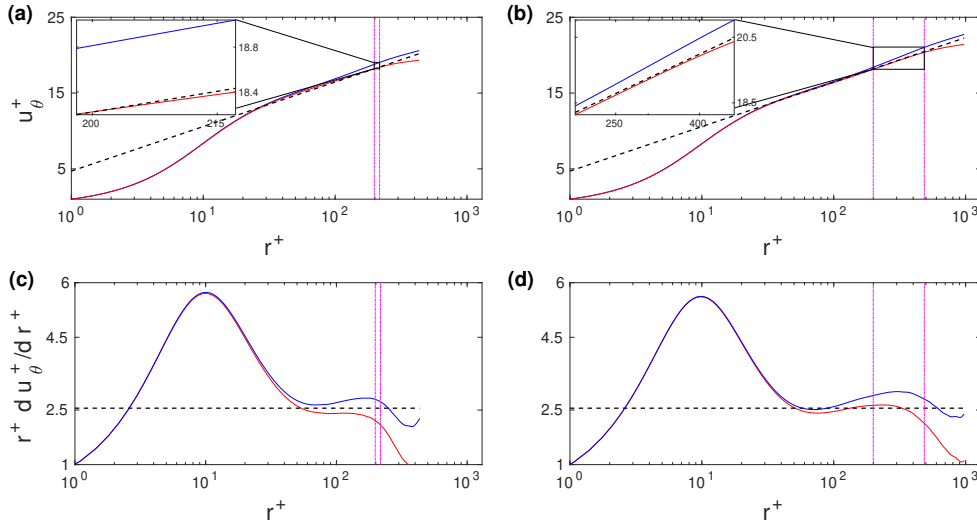


Figure 6.9: Semi–logarithmic plot of velocity profiles (a, b) and logarithmic derivatives (c, d) as in figure 6.3 for the outer cylinder profiles at $\eta = 0.91$.

of those cases until we have the data sets also of the bigger domains.

6.5 Summary and conclusion

In the spirit of an asymptotic expansion of the mean velocity profile, whose first order effects can be ascribed to pressure gradient for many classical flow ([87, 88]), we have derived a first order correction for TC flow based on the link between the wall mean shear stress τ_w and the transverse current of azimuthal motion J^w ([14]). Several direct numerical simulations have been performed in order to test the validity of the correction on small gap geometries $\eta = 0.91, 0.95, 0.98$ and with $R_\Omega = 0$, that means, in absence of Coriolis forces.

We have first eliminated the effect of the wake on the wall function in order to get the best parameters of the log law $u_\theta^+ = \frac{1}{k} \log(r^+) - A_1 g Re_\tau^{-1} r^+ + B$. We have found a common value $k = 0.392$ of the von Kármán constant for the three geometries. This value is the same found in [88] for channel flow, pipe flow and PC flow, and it is also close to the value found experimentally by [58] and numerically by [111].

For the other two constants we have found a geometry dependence. The $A_1 g$ parameter reaches the zero value as $\eta \rightarrow 0$, consistent to the fact that PC flow does not exhibit neither pressure gradient nor curvature effects. Similarly also the B collapse to the value $B = 4.48$ found for PC flow. We have also found that this collapse is almost linear, and we believe that this effect is due to some high order curvature effects.

For all the three geometries and for both inner and outer cylinder walls we have then found for different Reynolds numbers Re_τ a good agreement with the log law of both the corrected mean velocity profile and its logarithmic derivative. Moreover this concordance is improved with respect to the uncorrected profile, whose behavior is much less logarithmic, especially when looking at the derivative slope, far from being horizontal.

Even if this is a first attempt to recollect the universality of the logarithmic law in the presence of curvature, however, much work has to be done. The first issue to be solved, as suggested also in [88], is the numerical influence on the statistics of the flow; indeed in TC flow the artificial symmetry and the small dimension imposed on the domain have non negligible effects on the flow in the bulk (Taylor rolls), and this affects our estimations. Once numerical issues will be solved, we will be able to see if there are some yet undiscovered physical features.

And of course a more deep study on the effects of geometry is needed, both on

curvature, i.e. η dependency, and on shear influence, i.e. due to R_Ω , since it is known that they affect both boundary layers and bulk velocity profiles, but the picture is not complete yet, especially for high values of Reynolds number.

Chapter 7

Conclusions and outlook

Turbulence is the last big question mark in classical field, and even a simple set up as Taylor-Couette, the flow in between two coaxial and independently rotating cylinders, is far from being totally understood. However, the improvements of the last decades in computation have made possible the use of numerical simulations as a tool for better understanding phenomena in many different systems, and in this thesis we took advantage of all the improvements in this field to conduct direct numerical simulations and analyze the effects of high turbulence on Taylor-Couette flow.

In particular, with this work we tried to understand the role of both curvature and rotation on turbulence, with a particular care for their impact on secondary flows, since large scale structures have been observed in many wall bounded systems, and it is well known that their appearance can considerably alter the flow.

The thesis starts with the description of the numerical code used for the simulations. In chapter 2 the high Reynolds number code for simulations of wall-bounded turbulence developed by van der Poel et al. [163] is detailed. The second-order finite-difference scheme by Verzicco and Orlandi [172] was modified by integrating explicitly the viscous terms in the wall-parallel directions. A pencil-type decomposition, with the pencils aligned in the wall-normal direction, was developed. This synergy between algorithm and data parallelization allowed for the total amount of communication to be minimal, and this made the code scale up to sixty-four thousand processors, allowing the largest simulations in the thesis to be performed.

In chapter 3 we performed DNS to investigate on the origin and the pinning of Taylor rolls at high Reynolds number. By using the convective reference frame of Dubrulle et al. [41] we linked this vortices to the large scale structures found for high turbulent PC flow, and we also discovered that large-scale streaky structures arise in the azimuthal (streamwise) direction. Thus the roll/streak pairs can be understood in the context of shear forces and not of centrifugal ones, as previously thought. In particular, this process can be seen as a spatially localized instance of a process reminiscent of the self-sustained process of shear flows described by Waleffe [176]: streaks are generated by the redistribution of shear stress by the rolls, and their instability sustains the evolution of the same rolls. However, rotation is also needed: for a narrow gap system, the self-sustained process is pinned under the presence of moderate anti-cyclonic rotation, described by the R_Ω parameter, and this pinning persists in the plane Couette limit value $\eta \rightarrow 1$, i.e. for no curvature.

In chapter 4 we explored TC flow with both experiments and direct numerical simulations to probe the flow globally and locally in the phase space of $(Ta - a)$ at high Reynolds number parameter space and with the radius ra-

tio fixed at $\eta = 0.91$. We showed that two maxima for angular momentum transport can be detected at two different rotation ratios of the cylinder and for the same Ta . As it was found in Brauckmann et al. [17], a broad peak is detected for corotating cylinders, while narrow peak is found when the cylinders are counter-rotating. We showed firstly that the narrow peak only appears with sufficient driving, leading to the detection of both peaks within the range of $Ta \in [1.33 \times 10^8, 3.31 \times 10^9]$. In addition, we showed that the broad peak disappears when $Ta > 4.95 \times 10^9$, leaving only the narrow peak in the counter-rotating regime. We showed that the original prediction of Brauckmann et al. [17] is correct: the broad peak is created due to centrifugal instabilities, and that the narrow peak is created due to shear instabilities that are originated from transitions of the boundary layers. The reason why the broad peak disappears is that with sufficient driving, these shear instabilities become more dominant as compared to the centrifugal ones. We also showed that the narrow peak moves non-monotonically with respect to the rotation ratio as the driving increases. We attributed this to a second transition in the scaling around $Ta \approx 10^{10}$, in which a sharp jump in the $Nu_\omega - Ta$ curve is observed. The reason behind this transition is that wind-sheared regions in the boundary walls disappear, allowing for the ejecting of plumes throughout the whole boundary layers. Furthermore, at $Ta = 5.10 \times 10^8$ the velocimetry revealed two neighboring rolls which rotate opposite to each other. By describing the magnitude of the Coriolis force with the rotation number R_Ω , we found firstly that the rolls increase their strength with increasing R_Ω ; and secondly, that the existence of the unusual state of the rolls mentioned previously could be due to roll-splitting, which seems to occur when the value of R_Ω is large enough so as to dislocate a roll and divide it in two new ones. In chapter 5 we moved our attention on rotating PC flow, in order to prove that Dynamic Mode Decomposition is a reliable filter for large-scale structures that is robust across parameter space and that is able to correctly detect the coherent structures that arise when the flow is turbulent. In particular, we showed that the method is able to detect the role of rotation on the different behaviour of large structures. When there is no added rotation on the flow, the large structures develop predominantly in the streamwise component, and no evident connection structures between velocity components are found. On the other hand, the different components of the flow are coupled through the Coriolis force when rotation is added on the system, and large structures are detected both in streamwise and wall-normal components. Moreover, we discovered that PC flow both with and without rotation can be decomposed in mean flow and a single harmonic, that repeats itself in smaller structures whose frequency double in space with increasing wavenumber. A similar pat-

tern was found for RB flow in its route to turbulence.

Finally, in the last chapter of this thesis we derived a first order correction for TC flow based on the link between the wall mean shear stress τ_w and the transverse current of azimuthal motion J^w [14]. We tested the validity of the model on small gap geometries $\eta = 0.91, 0.95, 0.98$ and with $R_\Omega = 0$, that means, in absence of Coriolis forces. Then we found a logarithmic law of the form $u_\theta^+ = \frac{1}{k} \log(r^+) - A_1 g Re_\tau^{-1} r^+ + B$, with a common value $k = 0.392$ of the von Kármán constant for the three values of η , and for the other two parameters we have found values that depend linearly on the geometry, but however collapse onto the values already found for PC flow. For all the three geometries and for both inner and outer cylinder walls we found a good agreement with the log law of both the corrected mean velocity profile and its logarithmic derivative for different Reynolds numbers Re_τ .

Along this thesis we tried to clarify the underlying mechanisms that rise at high turbulence in TC flow, for different curvatures η and rotations R_Ω , with a particular care on large scale structures. However, several open questions are raised and still remain unanswered. Even if it is clear that turbulent Taylor rolls are caused and pinned by the combined action of shear and Coriolis forces, still it is not clear how these forces are combined together, and how they impose to the different velocity components to interact with each other. This is a crucial step if we want to analyze the formation and dynamics of large scale structures formed by shear and rotation, not only in TC flow, but also in other wall-bounded flows. Thus it is still impossible to give the mathematical prediction of the evolution of these structures, as instead was already proposed for square ducts in [119]. The following step would be the complete decoupling of curvature, shear and rotation, and their separate effects on other quantities of the flow, in the spirit of what we have started in chapter 4. Also, all simulations in this thesis have been performed with axially periodic boundary conditions. For this reason, we need to answer to another essential question: what are the effects of the computational box size on the statistics of the Taylor-Couette flow? We have already shown in chapter 3 that the azimuthal extent influence the meandering of the rolls in the axial direction, and in chapter 5 that different dynamics in the BLs and in the number of the rolls can occur when the axial extent varies. Thus it would be important to characterize the box-size dependency on the dynamics of the flow, on large coherent structures (Taylor rolls) and on the velocity profiles in the near wall region.

Once we have found the answer to all of these question, we could try understand how (or even, if) overlap layers form in TC flow, and so to put an

other piece in the puzzle of universality for Prandtl logarithmic law of the mean velocity profile. This is a fundamental piece of the puzzle, since most of the practical applications involve high Reynolds number flows that cannot be tackled by direct numerical simulations, even with all the technological improvements of the last decades. Thus they require the use of wall functions to alleviate the computational load. These wall functions, however, are derived from the classical flat plate, zero-pressure gradient boundary layer flow and they do not describe properly the realistic geometries with curvature. The correction accounting for both mean rotation and wall curvature would be a step forward the derivation of a more general law of the wall for high Reynolds number turbulent modeling. Any upgrade in the fundamental theory of wall turbulence would improve the understanding of many phenomena that are crucial either for theoretical purposes but also for many engineering applications. If we could develop Prandtl theory, we would have the possibility of extracting features to improve closure models of turbulence such as LES. It is clear that physical insight and accurate prediction of flows via universal theory is a matter of high interest in the engineering practice. There are many different opinions on the topic and it would be necessary to collect them all back in a unique theory.

Appendix A

Domain dependency

In section 6.3 we have mentioned that a small computational domain could affect the estimation of the log law due to the wandering of the remnants of Taylor rolls. We can have a first sight on this effect looking at figure A.1, that shows the estimation of the three parameters A_0 , A_1g and B . When we apply the wake elimination procedure to estimate the von Kármán constant, we can see that the obtained lines are not exactly horizontal, probably because the Reynolds number range is not wide enough to properly eliminate the wake function, or to an averaging time not long enough. This effect was also seen in [88], and indeed our picture is very similar to his figure 9. However seems that once inside the defect layer, all curves tend to align along straight lines that radiate from a common point located at $A_0 = 2.55$.

The effect is even more evident in the estimation of the two others parameters, since both the values varies with Re_τ and only a collective fitting of all the curves in the respective logarithmic layer seems to properly catch the property. Another consequence of the wandering of the rolls is the effect on the velocity profiles in the bulk, as reported in figure A.2. We have compared two profiles at the same $Re_\tau = 780$ but with different averaging times: one statistic taken after 20 large eddies turnover times, one after 40. The obtained profiles are the same until they get in the bulk region; the difference is even more evident from the logarithmic derivatives.

So even if it is capable to give good results on torque and mean statistic, the small box with $\Gamma = 2.33$ and $N = 20$ has defects in reproducing velocities in the bulk, and the question “*how big is big enough*” arise again.

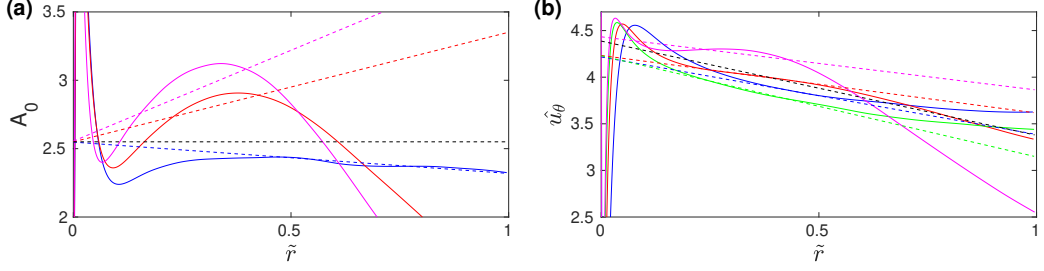


Figure A.1: (a) Wake elimination procedure for $\eta = 0.91$ with $\Gamma = 2.33$ and $N = 20$ from the difference of two curves at $Re_\tau = 1000$ and $Re_\tau = 500$ (solid blue), $Re_\tau = 1200$ and $Re_\tau = 500$ (solid red), $Re_\tau = 1200$ and $Re_\tau = 780$ (solid magenta); the black dashed line is the expected value of $A_0 = 2.55$. (b) A_1g and B coefficient evaluation; the best linear fit brings to the coefficients $A_1g = -0.83$, $B = 4.22$ for $Re_\tau = 500$ (dashed blue), $A_1g = -0.61$, $B = 4.23$ for $Re_\tau = 7800$ (dashed red), $A_1g = -1.08$, $B = 4.23$ for $Re_\tau = 1000$ (dashed green), $A_1g = -0.57$, $B = 4.43$ for $Re_\tau = 1200$ (dashed magenta) and a collective fitting of $A_1 = -1.01$, $B = 4.38$ (dashed black).

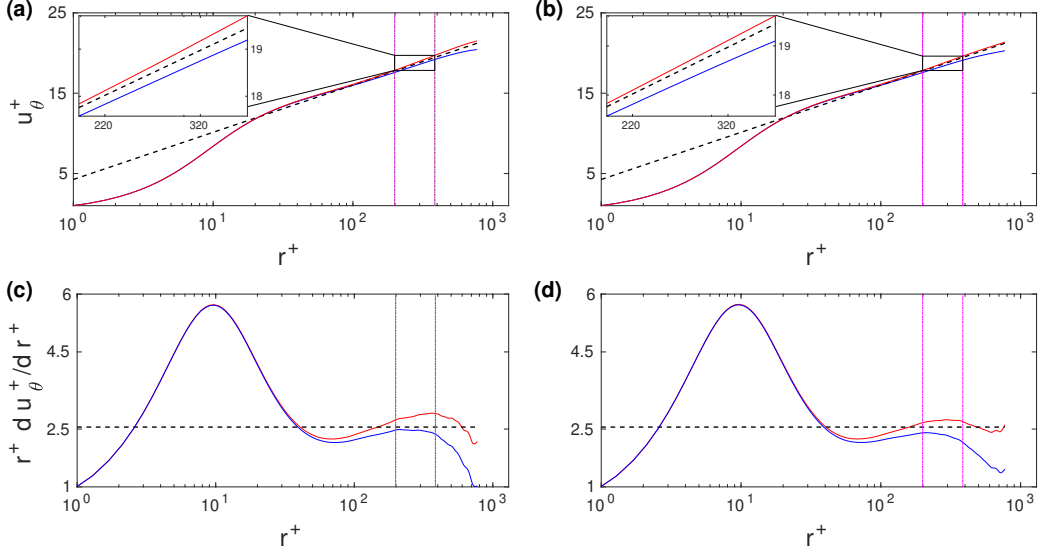


Figure A.2: Semi-logarithmic plot of velocity profiles for two different averaging times (a, b) and their logarithmic derivatives (c, d), for $\eta = 0.91$ and $Re_\tau = 780$ with $\Gamma = 2.33$ and $N = 20$. Colours as in figure 6.3.

Bibliography

- [1] *2DECOMP&FFT – A Highly Scalable 2D Decomposition Library and FFT Interface*, 2010. Cray User Group 2010 conference.
- [2] Guenter Ahlers. Low-temperature studies of the rayleigh–bénard instability and turbulence. *Physical Review Letters*, 33(20):1185, 1974.
- [3] Guenter Ahlers, Eberhard Bodenschatz, Denis Funfschilling, and James Hogg. Turbulent rayleigh–bénard convection for a prandtl number of 0.67. *Journal of Fluid Mechanics*, 641:157–167, 2009.
- [4] Guenter Ahlers, Siegfried Grossmann, and Detlef Lohse. Heat transfer and large scale dynamics in turbulent rayleigh–bénard convection. *Reviews of modern physics*, 81(2):503, 2009.
- [5] Guenter Ahlers, Xiaozhou He, Denis Funfschilling, and Eberhard Bodenschatz. Heat transport by turbulent Rayleigh–Bénard convection for $\text{Pr} \simeq 0.8$ and $3 \times 10^{12} \leq \text{Ra} \leq 10^{15}$: aspect ratio $\Gamma = 0.50$. *New Journal of Physics*, 14(10):103012, 2012.
- [6] C. D. Andereck, S. S. Liu, and H. L. Swinney. Flow regimes in a circular Couette system with independently rotating cylinders. *J. Fluid Mech.*, 164:155–183, 1986.
- [7] M. Avila. Stability and angular-momentum transport of fluid flows between corotating cylinders. *Physical Review Letters*, 108(12), 2012.
- [8] V. Avsarkisov, S. Hoyas, M. Oberlack, and J. P. García-Galache. Turbulent plane Couette flow at moderately high Reynolds number. *J. Fluid Mech.*, 751:R1–8, 2014.
- [9] S.C.C. Bailey, M. Vallikivi, M. Hultmark, and A.J. Smits. Estimating the value of von kármán constant in turbulent pipe flow. *J. Fluid Mech.*, 749:79 – 98, 2014.
- [10] BJ Balakumar and RJ Adrian. Large-and very-large-scale motions in channel and boundary-layer flows. *Philosophical Transactions of the*

-
- Royal Society A: Mathematical, Physical and Engineering Sciences*, 365 (1852):665–681, 2007.
- [11] RP Behringer. Rayleigh-bénard convection and turbulence in liquid helium. *Reviews of modern physics*, 57(3):657, 1985.
- [12] M. Bernardini, S. Pirozzoli, and P. Orlandi. Velocity statistics in turbulent channel flow up to $Re_\tau = 4000$. *Journal of Fluid Mechanics*, 742: 171–191, 2014.
- [13] Eberhard Bodenschatz, Werner Pesch, and Guenter Ahlers. Recent developments in rayleigh-bénard convection. *Annual review of fluid mechanics*, 32(1):709–778, 2000.
- [14] H. J. Brauckmann and B. Eckhardt. Direct numerical simulations of local and global torque in Taylor-Couette flow up to $Re=30.000$. *J. Fluid Mech*, 718:398–427, 2013.
- [15] H. J. Brauckmann and B. Eckhardt. Intermittent boundary layers and torque maxima in Taylor-Couette flow. *Phys. Rev. E*, 87:033004, 2013.
- [16] H. J. Brauckmann and B. Eckhardt. Marginally stable and turbulent boundary layers in low-curvature Taylor-Couette flow. *J. Fluid Mech.*, 815:149–168, 2017.
- [17] H. J. Brauckmann, M. Salewski, and B. Eckhardt. Momentum transport in Taylor-Couette flow with vanishing curvature. *J. Fluid Mech.*, 790: 419–452, 2016.
- [18] S. L. Brunton, B. W. Brunton, J. L. Proctor, E. Kaiser, and Kutz J. N. Chaos as an intermittently forced linear system. *Nature Communications*, 8, 2017.
- [19] P Büchel, M Lücke, D Roth, and R Schmitz. Pattern selection in the absolutely unstable regime as a nonlinear eigenvalue problem: Taylor vortices in axial flow. *Physical Review E*, 53(5):4764, 1996.
- [20] F. H. Busse. The stability of finite amplitude cellular convection and its relation to an extremum principle. *Journal of Fluid Mechanics*, 30(4): 625–649, 1967.
- [21] F. H. Busse. Viewpoint: The twins of turbulence research. *Physics*, 5 (4), 2012.

- [22] E. Calzavarini, F. Toschi, and R. Tripicciono. Evidences of bolgiano-obhukhov scaling in three-dimensional rayleigh-bénard convection. *Physical Review E - Statistical Physics, Plasmas, Fluids, and Related Interdisciplinary Topics*, 66(1), 2002.
- [23] E. Calzavarini, C. R. Doering, J. D. Gibbon, D. Lohse, A. Tanabe, and F. Toschi. Exponentially growing solutions in homogeneous rayleigh-bénard convection. *Physical Review E - Statistical, Nonlinear, and Soft Matter Physics*, 73(3), 2006.
- [24] Johan Carlier and Michel Stanislas. Experimental study of eddy structures in a turbulent boundary layer using particle image velocimetry. *Journal of Fluid Mechanics*, 535:143–188, 2005.
- [25] S. Chandrasekhar. *Hydrodynamic and Hydromagnetic Stability*. Dover, 1981.
- [26] K. K. Chen, J. H. Tu, and C. W. Rowley. Variants of dynamic mode decomposition: boundary condition, koopman, and fourier analyses. *J. Nonlinear Sci.*, 22(6):887–915, 2012.
- [27] N.-S. Cheng. Formula for the viscosity of a glycerol-water mixture. *Ind. Eng. Chem. Res.*, 47:3285–3288, 2008.
- [28] Pascal Chossat and Gérard Iooss. *The Couette-Taylor Problem*, volume 102. Springer Science & Business Media, 2012.
- [29] D. Coles. The law of the wake in the turbulent boundary layer. *J. Fluid Mech.*, 1:191–226, 1956.
- [30] D Coles. Transition in circular couette flow. *Journal of Fluid Mechanics*, 21:385–425, 1965.
- [31] Maurice Couette. *Etudes sur le frottement des liquides*. PhD thesis, 1890.
- [32] K Coughlin and PS Marcus. Turbulent bursts in couette-taylor flow. *Physical review letters*, 77(11):2214, 1996.
- [33] R. Courant, K. Friedrichs, and H. Lewy. Über die partiellen differenzengleichungen der mathematischen physik. *Mathematische Annalen*, 100(1):32–74, 1928.
- [34] Mark C Cross and Pierre C Hohenberg. Pattern formation outside of equilibrium. *Reviews of modern physics*, 65(3):851, 1993.

-
- [35] Michael Cross and Henry Greenside. *Pattern formation and dynamics in nonequilibrium systems*. Cambridge University Press, 2009.
- [36] Nicola Demo, Marco Tezzele, and Gianluigi Rozza. PyDMD: Python Dynamic Mode Decomposition. *The Journal of Open Source Software*, 3(22):530, 2018. doi: 10.21105/joss.00530.
- [37] T. Dessup, L. S. Tuckerman, J. E. Wesfreid, D. Barkley, and A. P. Willis. The Self-Sustaining Process in Taylor-Couette flow. *arXiv*, 1808 (07253), 2018.
- [38] RC DiPrima, HL Swinney, and JP Gollub. Hydrodynamic instabilities and the transition to turbulence. *Springer, Berlin*, 38:134, 1981.
- [39] R. Donnelly. Taylor-Couette flow: the early days. *Physics Today*, pages 32–39, November 1991.
- [40] PG Drazin and WH Reid. *Hydrodynamic stability*, 1998.
- [41] B. Dubrulle, O. Dauchot, F. Daviaud, P. Y. Longaretti, D. Richard, and J. P. Zahn. Stability and turbulent transport in Taylor–Couette flow from analysis of experimental data. *Phys. Fluids*, 17:095103, 2005.
- [42] M. Duponcheel, P. Orlandi, and G. Winckelmans. Time-reversibility of the euler equations as a benchmark for energy conserving schemes. *Journal of Computational Physics*, 227(19):8736–8752, 2008.
- [43] B. Eckhardt, S. Grossmann, and D. Lohse. Torque scaling in turbulent taylor–couette flow between independently rotating cylinders. *J. Fluid Mech.*, 581:221–250, 2007.
- [44] Alexander Esser and Siegfried Grossmann. Analytic expression for taylor–couette stability boundary. *Physics of Fluids*, 8(7):1814–1819, 1996.
- [45] E. A. Fadlun, R. Verzicco, P. Orlandi, and J. Mohd-Yusof. Combined immersed-boundary finite-difference methods for three-dimensional complex flow simulations. *Journal of Computational Physics*, 161(1): 35–60, 2000.
- [46] H. Faisst and B. Eckhardt. Transition from the Couette-Taylor system to the plane Couette system. *Phys. Rev. E*, 61(6):7227, 2000.
- [47] M. A. Fardin, C. Perge, and N. Taberlet. The hydrogen atom of fluid dynamics — introduction to the taylor–couette flow for soft matter scientists. *Soft Matter*, 10:3523–3535, 2014. doi: 10.1039/C3SM52828F.

- [48] B. Gayen, G. O. Hughes, and R. W. Griffiths. Completing the mechanical energy pathways in turbulent rayleigh- b enard convection. *Physical Review Letters*, 111(12), 2013.
- [49] Thomas Gebhardt and Siegfried Grossmann. The taylor-couette eigenvalue problem with independently rotating cylinders. *Zeitschrift f ur Physik B Condensed Matter*, 90(4):475–490, 1993.
- [50] S. Ghosal. An analysis of numerical errors in large-eddy simulations of turbulence. *Journal of Computational Physics*, 125(1):187–206, 1996.
- [51] J. Grosek and J. N. Kutz. Dynamic mode decomposition for real-time back-ground/foreground separation in video. *arXiv*, 1404.7592, 2014.
- [52] S. Grossmann and D. Lohse. Multiple scaling in the ultimate regime of thermal convection. *Phys. Fluids*, 23:045108, 2011.
- [53] S. Grossmann, D. Lohse, and C. Sun. High-Reynolds number Taylor-Couette turbulence. *Ann. Rev. Fluid Mech.*, 48:53–80, 2016.
- [54] J. M. Hamilton, J. Kim, and F. Waleffe. Regeneration mechanisms of near-wall turbulence structures. *J. Fluid Mech.*, 287:317–348, 1995.
- [55] x. He, D. Funfschilling, H. Nobach, E. Bodenschatz, and G. Ahlers. Transition to the ultimate state of turbulent Rayleigh–B enard convection. *Phys. Rev. Lett.*, 108(2):024502, 2012.
- [56] Hristina Hristova, S ebastien Roch, Peter J Schmid, and Laurette S Tuckerman. Transient growth in taylor–couette flow. *Physics of Fluids*, 14(10):3475–3484, 2002.
- [57] S. G. Huisman, D. P. M. van Gils, S. Grossmann, C. Sun, and D. Lohse. Ultimate turbulent Taylor-Couette flow. *Phys. Rev. Lett.*, 108:024501, 2012.
- [58] S. G. Huisman, S. Scharnowski, C. Cierpka, C. K ahler, D. Lohse, and C. Sun. Logarithmic boundary layers in strong Taylor-Couette turbulence. *Phys. Rev. Lett.*, 110:264501, 2013.
- [59] S. G. Huisman, R. C. A. van der Veen, C. Sun, and D. Lohse. Multiple states in highly turbulent Taylor-Couette flow. *Nature Comm.*, 5, 2014.
- [60] J. Jimenez. Cascades in wall-bounded turbulence. *Ann. Rev. Fluid Mech.*, 44:27–45, 2012.

- [61] J. Jiménez and P. Moin. The minimal flow unit in near-wall turbulence. *J. Fluid Mech.*, 225:213–240, 1991.
- [62] C. A. Jones. The transition to wavy Taylor vortices. *J. Fluid Mech.*, 157:135–162, 1985.
- [63] Leo P Kadanoff. Turbulent heat flow: structures and scaling. *Physics today*, 54(8):34–39, 2001.
- [64] Y. Kaneda, T. Ishihara, M. Yokokawa, K. Itakura, and A. Uno. Energy dissipation rate and energy spectrum in high resolution direct numerical simulations of turbulence in a periodic box. *Physics of Fluids*, 15(2): L21–L24, 2003.
- [65] J. Kim, P. Moin, and R. Moser. Turbulence statistics in fully developed channel flow at low reynolds number. *Journal of Fluid Mechanics*, 177: 133–166, 1987.
- [66] KC Kim and RJ Adrian. Very large-scale motion in the outer layer. *Phys. Flu.*, 11(2):417–422, 1999.
- [67] Andrej Nikolaevič Kolmogorov. On degeneration (decay) of isotropic turbulence in an incompressible viscous liquid. In *Dokl. Akad. Nauk SSSR*, volume 31, pages 538–540, 1941.
- [68] Ernst L Koschmieder. *Bénard cells and Taylor vortices*. Cambridge University Press, 1993.
- [69] A. G. Kravchenko and P. Moin. On the effect of numerical errors in large eddy simulations of turbulent flows. *Journal of Computational Physics*, 131(2):310–322, 1997.
- [70] R. P. J. Kunnen, H. J. H. Clercx, B. J. Geurts, L. J. A. Van Bokhoven, R. A. D. Akkermans, and R. Verzicco. Numerical and experimental investigation of structure-function scaling in turbulent rayleigh-bénard convection. *Physical Review E - Statistical, Nonlinear, and Soft Matter Physics*, 77(1), 2008.
- [71] J. N. Kutz. *Data-driven modeling & scientific computation: methods for complex systems & big data*. Oxford University Press, Oxford, 2013.
- [72] J. Nathan Kutz, Steven L. Brunton, Bingni W. Brunton, and Joshua L. Proctor. *Dynamic Mode Decomposition: Data-Driven Modeling of Complex Systems*. SIAM, 2016.

- [73] J. Nathan Kutz, X. Fu, and Steven L. Brunton. Multi-resolution dynamic mode decomposition. *SIAM J. Appl. Dyn. Sys.*, 15.2:713–735, 2016.
- [74] D. P. Lathrop, J. Fineberg, and H. L. Swinney. Transition to shear-driven turbulence in Couette-Taylor flow. *Phys. Rev. A*, 46:6390–6405, 1992.
- [75] Daniel P Lathrop, Jay Fineberg, and Harry L Swinney. Turbulent flow between concentric rotating cylinders at large reynolds number. *Physical review letters*, 68(10):1515, 1992.
- [76] S. Le Clainche and J. M. Vega. HODMD. <https://github.com/LeClaincheVega/HODMD>, 2017. [Online; accessed 1-July-2019].
- [77] S. Le Clainche and J. M. Vega. Higher order dynamic mode decomposition. *SIAM J. Appl. Dyn. Syst.*, 16(2):882–925, 2017.
- [78] S. Le Clainche and J. M. Vega. Analyzing nonlinear dynamics via data-driven dynamic mode decomposition-like methods. *Complexity*, page 6920783, 2018.
- [79] M. Lee and R. D. Moser. Extreme-scale motions in turbulent plane Couette flows. *J. Fluid Mech*, 842:128–145, 2018.
- [80] M. J. Lee, B. D. Oh, and Y. B. Kim. Canonical fractional-step methods and consistent boundary conditions for the incompressible navier-stokes equations. *Journal of Computational Physics*, 168(1):73–100, 2001.
- [81] G. S. Lewis and H. L. Swinney. Velocity structure functions, scaling, and transitions in high-reynolds-number couette-taylor flow. *Phys. Rev. E*, 59:5457–5467, May 1999. doi: 10.1103/PhysRevE.59.5457.
- [82] D. Lohse and F. Toschi. Ultimate state of thermal convection. *Physical Review Letters*, 90(3):034502/1–034501/3, 2003.
- [83] Detlef Lohse and Ke-Qing Xia. Small-scale properties of turbulent rayleigh-bénard convection. *Annual Review of Fluid Mechanics*, 42, 2010.
- [84] Edward N Lorenz. Deterministic nonperiodic flow. *Journal of the atmospheric sciences*, 20(2):130–141, 1963.
- [85] A. Lozano-Durán and J. Jiménez. Time-resolved evolution of coherent structures in turbulent channels: characterization of eddies and cascades. *J. Fluid Mech.*, 759:432–471, 2014.

-
- [86] A. Lozano-Durán and J. Jiménez. Effect of the computational domain on direct simulations of turbulent channels up to $re_\tau = 4200$. *Physics of Fluids*, 26(1), 2014.
- [87] P. Luchini. Universality of the turbulent velocity profile. *Physical review letters*, 118:224501, 2017.
- [88] P. Luchini. Structure and interpolation of the turbulent velocity profile in parallel flow. *European Journal of Mechanics B Fluids*, 71, 2018.
- [89] M. V. R. Malkus. The heat transport and spectrum of thermal turbulence. *Proc. R. Soc. London A*, 225:196–212, 1954.
- [90] A Mallock. Determination of the viscosity of water. *Proceedings of the Royal Society of London*, 45(273-279):126–132, 1889.
- [91] A Mallock. Experiments on fluid viscosity. *Proceedings of the Royal Society of London Series I*, 59:38–39, 1895.
- [92] Simon Maretzke, Björn Hof, and Marc Avila. Transient growth in linearly stable Taylor–Couette flows. *Journal of Fluid Mechanics*, 742:254–290, 2014.
- [93] Max Margules. *Ueber die Bestimmung des Reibungs- und Gleitungscoefficienten aus ebenen Bewegungen einer Fluessigkeit*. Aus der k. k. Hof- und Staatsdruckerei in Wien, 1881.
- [94] F Marques and JM Lopez. Taylor–Couette flow with axial oscillations of the inner cylinder: Floquet analysis of the basic flow. *Journal of Fluid Mechanics*, 348:153–175, 1997.
- [95] B. Martinez-Arias, J. Peixinho, O. Crumeyrolle, and I. Mutabazi. Effect of the number of vortices on the torque scaling in Taylor–Couette flow. *J. Fluid Mech.*, 748:756–767, 2014.
- [96] S. Merbold, H. Brauckmann, and C. Egbers. Torque measurements and numerical determination in differentially rotating wide gap Taylor–Couette flow. *Phys. Rev. E.*, 87(023014), 2013.
- [97] Álvaro Meseguer. Energy transient growth in the Taylor–Couette problem. *Physics of Fluids*, 14(5):1655–1660, 2002.
- [98] C. B. Millikan. A critical discussion of turbulent flows in channels and circular tubes. In *Proceedings of the Fifth International Congress for Applied Mechanics*, pages 386 – 392, Harvard Univ. and MIT, 1939. Wiley, New York.

- [99] M. Mohan Rai and P. Moin. Direct simulations of turbulent flow using finite-difference schemes. *Journal of Computational Physics*, 96(1):15–53, 1991.
- [100] Parviz Moin and John Kim. Numerical investigation of turbulent channel flow. *Journal of fluid mechanics*, 118:341–377, 1982.
- [101] R. D. Moser and P. Moin. The effect of curvature in wall-bounded turbulent flows. *J. Fluid Mech.*, 175:479–510, 1987.
- [102] T Mullin, KA Cliffe, and G Pfister. Unusual time-dependent phenomena in taylor-couette flow at moderately low reynolds numbers. *Physical review letters*, 58(21):2212, 1987.
- [103] M. Nagata. Three-dimensional finite-amplitude solutions in plane Couette flow: bifurcation from infinity. *J. Fluid Mech.*, 217:519–527, 1990.
- [104] Isaac Newton. *Philosophiae Naturalis Principia Mathematica* (“*Mathematical Principles of Natural Philosophy*”). London, 1687.
- [105] S. A. Orszag and G. S. Patterson. Numerical simulation of three-dimensional homogeneous isotropic turbulence. *Physical Review Letters*, 28(2):76–79, 1972.
- [106] R. Ostilla-Mónico, R. J. A. Stevens, S. Grossmann, R. Verzicco, and D. Lohse. Optimal Taylor–Couette flow: direct numerical simulations. *J. Fluid Mech.*, 719:14–46, 2013.
- [107] R. Ostilla-Mónico, E. P. van der Poel, R. Verzicco, S. Grossmann, and D. Lohse. Exploring the phase diagram of fully turbulent Taylor-Couette flow. *J. Fluid Mech.*, 761:1–26, 2014.
- [108] R. Ostilla-Mónico, E. P. van der Poel, R. Verzicco, S. Grossmann, and D. Lohse. Boundary layer dynamics at the transition between the classical and the ultimate regime of Taylor-Couette flow. *Phys. Fluids*, 26:015114, 2014.
- [109] R. Ostilla-Mónico, R. Verzicco, and D. Lohse. Effects of the computational domain size on DNS of Taylor-Couette turbulence with stationary outer cylinder. *Phys. Fluids*, 27:025110, 2015.
- [110] R. Ostilla-Monico, Yantao Yang, E.P. van der Poel, D. Lohse, and R. Verzicco. A multiple-resolution strategy for direct numerical simulation of scalar turbulence. *Journal of Computational Physics*, 301:308–321, 2015.

- [111] R. Ostilla-Mónico, D. Lohse, and R. Verzicco. Effect of roll number on the statistics of turbulent Taylor-Couette flow. *Phys. Rev. Flu.*, 1 (054402), 2016.
- [112] R. Ostilla-Mónico, R. Verzicco, S. Grossmann, and D. Lohse. The near-wall region of highly turbulent Taylor-Couette flow. *J. Fluid Mech.*, 768: 95–117, 2016.
- [113] Rodolfo Ostilla-Mónico, Xiaojue Zhu, Vamsi Spandan, Roberto Verzicco, and Detlef Lohse. Life stages of wall-bounded decay of Taylor-Couette turbulence. *Phys. Rev. Flu.*, 2(11):114601, 2017.
- [114] N.H. Packard, J.P. Crutchfield, J.D. Farmer, and R.S. Shaw. Geometry from a time series. *Phys. Rev. Lett.*, 45:712–716, 1980.
- [115] M. S. Paoletti and D. P. Lathrop. Angular momentum transport in turbulent flow between independently rotating cylinders. *Phys. Rev. Lett.*, 106:024501, 2011.
- [116] A. Parodi, J. Von Hardenberg, G. Passoni, A. Provenzale, and E. A. Spiegel. Clustering of plumes in turbulent convection. *Physical Review Letters*, 92(19):194503–1–194503–4, 2004.
- [117] G Pfister and I Rehberg. Space-dependent order parameter in circular couette flow transitions. *Physics Letters A*, 83(1):19–22, 1981.
- [118] S. Pirozzoli, M. Bernardini, and P. Orlandi. Turbulence statistics in Couette flow at high Reynolds number. *J. Fluid Mech.*, 758:327–343, 2014.
- [119] S. Pirozzoli, D. Modesti, P. Orlandi, and F. Grasso. Turbulence and secondary motions in square duct flow. *J. Fluid Mech.*, 840:631–655, 2018.
- [120] S. B. Pope. *Turbulent Flows*. Cambridge University Press, 2000.
- [121] L. Prandtl. In Verhandlungen des dritten internationalen mathematiker-kongresses in heidelberg vom 8. bis 13. august 1904. A. Krazer, ed., BG Teubner, Leipzig, Germany, 1905.
- [122] L. Prandtl. Bericht über untersuchungen zur ausgebildeten turbulenz. *Z. Angew. Math. Mech.*, 5:136, 1925.
- [123] L. Prandtl. The mechanics of viscous fluids. In *Aerodynamic Theory*, pages 34–208. Springer Berlin Heidelberg, 1935.

- [124] Ludwig Prandtl. Neuere ergebnisse der turbulenzforschung. *VDI-Ztschr*, 77(5):105, 1933.
- [125] Lord Rayleigh. On the dynamics of revolving fluids. *Proceedings of the Royal Society of London. Series A, Containing Papers of a Mathematical and Physical Character*, 93(648):148–154, 1917.
- [126] Osborne Reynolds. An experimental investigation of the circumstances which determine whether the motion of water shall be direct or sinuous, and of the law of resistance in parallel channels. *Philosophical Transactions of the Royal society of London*, (174):935–982, 1883.
- [127] William C Reynolds. The potential and limitations of direct and large eddy simulations. In *Whither turbulence? Turbulence at the crossroads*, pages 313–343. Springer, 1990.
- [128] Lewis Fry Richardson. The supply of energy from and to atmospheric eddies. *Proceedings of the Royal Society of London. Series A, Containing Papers of a Mathematical and Physical Character*, 97(686):354–373, 1920.
- [129] P. . Roche, F. Gauthier, R. Kaiser, and J. Salort. On the triggering of the ultimate regime of convection. *New Journal of Physics*, 12, 2010.
- [130] C.W. Rowley, I. Mezić, S. Bagheri, P. Schlatter, and D.S. Henningson. Spectral analysis of nonlinear flows. *J. Fluid Mech.*, 641:115–127, 2009.
- [131] Karl Rupp, M Horovitz, F Labonte, O Shacham, K Olukotun, L Hammond, and C Batten. 40 Years of microprocessor trend data. Data available on webpage <http://www.karlrupp.net/wp-content/uploads/2015>, Figures available on webpage <https://www.karlrupp.net/2015/06/40-years-of-microprocessor-trend-data>, 2015. [Online; accessed 7-November-2019].
- [132] F. Sacco, R. Verzicco, and R. Ostilla-Mónico. Dynamics and evolution of turbulent Taylor rolls. *J. Fluid Mech.*, 870:970–987, 2019.
- [133] M. Salewski and B. Eckhardt. Turbulent states in plane couette flow with rotation. *Phys. Fluids*, 27:045109, 2015.
- [134] J. D. Scheel, E. Kim, and K. R. White. Thermal and viscous boundary layers in turbulent rayleigh-bénard convection. *Journal of Fluid Mechanics*, 711:281–305, 2012.

-
- [135] P. J. Schmid. Dynamic mode decomposition of numerical and experimental data. *J. Fluid Mech.*, 656:5–28, 2010.
- [136] J. Schumacher. Lagrangian dispersion and heat transport in convective turbulence. *Physical Review Letters*, 100(13), 2008.
- [137] E. D. Siggia. High rayleigh number convection. *Annual Review of Fluid Mechanics*, 26(1):137–168, 1994.
- [138] J. A. Sillero, J. Jiménez, and R. D. Moser. Two-point statistics for turbulent boundary layers and channels at reynolds numbers up to $\delta^+ \approx 2000$. *Phys. Flu.*, 26(10):105109, 2014.
- [139] GP Smith and AA Townsend. Turbulent couette flow between concentric cylinders at large taylor numbers. *Journal of Fluid Mechanics*, 123:187–217, 1982.
- [140] A.J. Smits and I. Marusic. Wall-bounded turbulence. *Phys. Today*, 66: 25 – 30, 2013.
- [141] A.J. Smits, B.J. McKeon, and I. Marusic. High-reynolds number wall turbulence. *Annu. Rev. Fluid Mech.*, 43:353 – 375, 2010.
- [142] Vamsi Spandan, Rodolfo Ostilla-Mónico, Detlef Lohse, and Roberto Verzicco. Identifying coherent structures and vortex clusters in taylor-couette turbulence. *Journal of Physics: Conference Series*, 708:012006, 2016.
- [143] R. J. A. M. Stevens, D. Lohse, and R. Verzicco. Prandtl and rayleigh number dependence of heat transport in high rayleigh number thermal convection. *Journal of Fluid Mechanics*, 688:31–43, 2011.
- [144] R. J. A. M. Stevens, D. Lohse, and R. Verzicco. Sidewall effects in rayleigh-bénard convection. *Journal of Fluid Mechanics*, 741:1–27, 2014.
- [145] George Gabriel Stokes. On the theories of the internal friction of fluids in motion, and of the equilibrium and motion of elastic solids. *Transactions of the Cambridge Philosophical Society*, 8, 1880.
- [146] G. Stringo and R. Verzicco. Mean flow structure in thermal convection in a cylindrical cell of aspect ratio one half. *Journal of Fluid Mechanics*, 548:1–16, 2006.
- [147] Steven H Strogatz. Nonlinear dynamics and chaos: with applications to physics. *Biology, Chemistry, and Engineering (Studies in Nonlinearity)*, Perseus, Cambridge, UK, 1994.

- [148] F. Takens. Detecting strange attractors in turbulence. In D.A. Rand and L.-S. Young, editors, *Lecture Notes in Math. 898*, page 366–381. Springer, Berlin, New York, 1981.
- [149] G. I. Taylor. Stability of a viscous liquid contained between two rotating cylinders. *Phil. Trans. R. Soc. A*, 223:289–343, 1923.
- [150] G. I. Taylor. Experiments on the motion of solid bodies in rotating fluids. *Proc. R. Soc. Lond. A*, 104:213–218, 1923.
- [151] Geoffrey Ingram Taylor. Stability of a viscous liquid contained between two rotating cylinders. *Philosophical Transactions of the Royal Society of London. Series A, Containing Papers of a Mathematical or Physical Character*, 223(605-615):289–343, 1923.
- [152] Geoffrey Ingram Taylor. Fluid friction between rotating cylinders i—torque measurements. *Proceedings of the Royal Society of London. Series A-Mathematical and Physical Sciences*, 157(892):546–564, 1936.
- [153] Robert Taylor. Dynamic Mode Decomposition in Python. <http://www.pyrunner.com/weblog/2016/07/25/dmd-python/>, 2016. [Online; accessed 3-June-2019].
- [154] Robert Taylor. Multi-resolution DMD. <http://www.pyrunner.com/weblog/2016/08/05/mrdmd-python/>, 2016. [Online; accessed 12-June-2019].
- [155] S. M. Tobias and J. B. Marston. Three-dimensional rotating Couette flow via the generalised quasilinear approximation. *J. Fluid Mech*, 810: 412–428, 2017.
- [156] T. Tsukahara, H. Kawamura, and K. Shingai. DNS of turbulent Couette flow with emphasis on the large-scale structure in the core region. *J. Turb.*, 7(19), 2006.
- [157] J. Tu, C.W. Rowley, D. Luchtenberg, S. Brunton, and J. N. Kutz. On dynamic mode decomposition: Theory and applications. *J. Comp. Dyn.*, 1:391–421, 2014.
- [158] Laurette S Tuckerman. Taylor vortices versus taylor columns. *Journal of Fluid Mechanics*, 750:1–4, 2014.
- [159] E. P. van der Poel, R. Stevens, and D. Lohse. Connecting flow structures and heat flux in turbulent Rayleigh-Bénard convection. *Phys. Rev. E*, 045303(R), 2011.

-
- [160] E. P. van der Poel, R. Stevens, K. Sugiyama, and D. Lohse. Flow states in two-dimensional Rayleigh-Bénard convection as a function of aspect-ratio and rayleigh number. *Phys. Fluids*, 085104, 2012.
- [161] E. P. Van Der Poel, R. J. A. M. Stevens, and D. Lohse. Comparison between two-and three-dimensional rayleigh-bénard convection. *Journal of Fluid Mechanics*, 736:177–194, 2013.
- [162] E. P. Van Der Poel, R. Ostilla-Mónico, R. Verzicco, and D. Lohse. Effect of velocity boundary conditions on the heat transfer and flow topology in two-dimensional rayleigh-bénard convection. *Physical Review E - Statistical, Nonlinear, and Soft Matter Physics*, 90(1), 2014.
- [163] E. P. van der Poel, R. Ostilla-Mónico, J. Donners, and R. Verzicco. A pencil distributed finite difference code for strongly turbulent wall-bounded flows. *Comp. Fluids*, 116:10–16, 2015.
- [164] Erwin P. van der Poel, Roberto Verzicco, Siegfried Grossmann, and Detlef Lohse. Plume emission statistics in turbulent rayleigh-bénard convection. *Journal of Fluid Mechanics*, 772:5–15, 2015.
- [165] R. C. A. van der Veen, S. G. Huisman, S. Merbold, U. Harlander, C. Egbers, D. Lohse, and C. Sun. Taylor-Couette turbulence at radius ratio $\eta = 0.5$: scaling, flow structures and plumes. *J. Fluid Mech.*, 799:334–351, 2016.
- [166] M. van Dyke. *Perturbation Methods in Fluid Mechanics*. Academic Press, 1964.
- [167] D. P. M. van Gils, S. G. Huisman, S. Grossmann, C. Sun, and D. Lohse. Optimal Taylor-Couette turbulence. *J. Fluid Mech.*, 706:118–149, 2012.
- [168] Dennis PM van Gils, Gert-Wim Bruggert, Daniel P Lathrop, Chao Sun, and Detlef Lohse. The twente turbulent taylor-couette (t3c) facility: strongly turbulent (multiphase) flow between two independently rotating cylinders. *Review of scientific instruments*, 82(2):025105, 2011.
- [169] Various. Turbulence - online encyclopedia treccani (treccani.it). <http://www.treccani.it/vocabolario/turbolenza>. [Online; accessed October-2019].
- [170] R. Verzicco and R. Camussi. Transitional regimes of low-prandtl thermal convection in a cylindrical cell. *Phys. Fluids*, 9:1287, 1997.

- [171] R. Verzicco and R. Camussi. Numerical experiments on strongly turbulent thermal convection in a slender cylindrical cell. *Journal of Fluid Mechanics*, (477):19–49, 2003.
- [172] R. Verzicco and P. Orlandi. A finite-difference scheme for three-dimensional incompressible flow in cylindrical coordinates. *J. Comput. Phys.*, 123:402–413, 1996.
- [173] R. Verzicco and K. R. Sreenivasan. A comparison of turbulent thermal convection between conditions of constant temperature and constant heat flux. *Journal of Fluid Mechanics*, 595:203–219, 2008.
- [174] T. von Kármán. Mechanische Ähnlichkeit und turbulenz. In *Proceedings of the Third International Congress for Applied Mechanics*, pages 85 – 105, Stockholm, 1930.
- [175] A. W. Vreman and J. G. M. Kuerten. Comparison of direct numerical simulation databases of turbulent channel flow at $re_\tau = 180$. *Physics of Fluids*, 26(1), 2014.
- [176] F. Waleffe. On a self-sustaining process in shear flows. *Phys. Fluids*, 9: 883–900, 1997.
- [177] Y. Yang, E. P. van der Poel, R. Ostilla-Mónico, C. Sun, R. Verzicco, and S. Grossmann. Salinity transfer in bounded double diffusive convection. *J Fluid Mech*, 768:476–491, 2015.
- [178] Mark V Zagarola and Alexander J Smits. Mean-flow scaling of turbulent pipe flow. *Journal of Fluid Mechanics*, 373:33–79, 1998.
- [179] Xiaojue Zhu, Rodolfo Ostilla-Mónico, Roberto Verzicco, and Detlef Lohse. Direct numerical simulation of taylor–couette flow with grooved walls: torque scaling and flow structure. *Journal of Fluid Mechanics*, 794:746–774, 2016.